Pulsed Power Discharges in Water

Thesis by

Axel Wolf Hendrik Kratel

In Partial Fulfillment of the Requirements

for the Degree of

Doctor of Philosophy

Advisor: Professor Michael Hoffmann

California Institute of Technology

Pasadena, California

1996

(Submitted May 31, 1996)

Acknowledgments

Many individuals have made this work possible. First and foremost, I would like to thank my advisor, Dr. Michael Hoffmann, who has made this work possible in the first place. He has taken a great risk in introducing a new technology to the environmental remediation community, but such risks are what puts Caltech at the cutting edge of science and technology. The faculty, staff and students in the Environmental Engineering Science department at Caltech have made my stay in the Hoffmann Group a pleasant and rewarding experience. Thanks also to various faculty members of the Environmental Engineering Department at Caltech, such as Dr. John List, Dr. Norman Brooks and Dr. Glen Cass, for invaluable discussions and insight. I would like to acknowledge my committee members, Dr. Roger Blandford, Dr. Nai-Chang Yeh, Dr. Frederick Zachariasen, and Dr. Christopher Brennen for serving on my examination committees. Dr. Paul Bellan in the Department of Applied Physics was kind enough to lend us his optical multi-channel analyzer, and has provided insightful comments and suggestions. I would like to acknowledge Dr. Julie Kornfield for exposing me to Polymer Science, and Dr. Harvey Newman and David Hitlin for giving me an opportunity to glimpse into the world of High Energy physics.

Many individuals deserve special thanks for making significant contributions to the Pulsed Power project. In particular, Dean Willberg's tenacity saw us through the initial hurdles related to the less than ideal initial reactor design. Thanks to him, the Caltech Pulsed Power Facility now has a fully functional reactor which so far has not failed. Patrick Lang and Ralf Hoechemer did much of the analytical chemistry work and provided valuable companionships. Peter Green was always there to make sure that all

of the analytical instruments fulfill their functions. Thnaks to John McGill for helping with the early phases of the project. Joe Fontana provided his valuable machinist skills, and Hay Vu installed the security interlock system. Rich Eastvedt helped with various projects, including the construction of the "outhouse." Thanks also to Dr. Martin Gundersen of the University of Southern California, who during his sabbatical at Caltech provided useful advice on pulsed power electronics, and invited me to attend the first conference on Commercialization of Pulsed Power Technology.

Linda Scott, Fran Matzen, and Carmen Lopez have been of invaluable help in solving many administrative problems, and have made my stay at Caltech very enjoyable through their wonderful companionship. They have done a lot to foster a sense of community in the department. Thanks also to my fellow students in Environmental Engineering Science, who have provided good companionship. They include Jim, Anne, Veronica, Dennis, Linda, Greg, Sam, Wonyong, Ron, Simo, Bruce, Janet, Jeff, Susan, Talal, Jerry, Amy, Nicola and many others. Special thanks in particular to Tom Lloyd, who was kind enough to proofread parts of this thesis, and provide invaluable discussions and insight. The librarians, Rayma Harrison and Suzan Leising, and the staff at Millikan library helped find many obscure references.

I am grateful for financial support from the Defense Advanced Research Agency and from the Electric Power Research Institute. I also received financial support in the form of a Grace Fellowship.

I would like to acknowledge several individuals at UC Irvine who have made it possible for me to reach this far in the first place. Thanks to Dr. Henry Sobel and Dr. Frederick Reines for allowing me to work in the Neutrino Physics Laboratory prior to

my admittance to the undergraduate Physics program at UC Irvine. Thanks to all the faculty there who truly inspired me, including Dr. Mildred Moe, Dr. Jonas Schultz, Dr. Riley Newman, and Dr. William Parker.

Finally, last and certainly not least, I would like to acknowledge my family, who have provided much needed support and encouragement. I owe the biggest thanks to my wife Kris, who always provided invaluable love and moral support, which was especially needed in those dark times when nothing seemed to work. This thesis is dedicated to her.

Abstract

An Electrohydraulic Discharge Process (*EHD*) for the treatment of hazardous chemical wastes in water has been developed. Liquid waste in a 4 *L EHD* reactor is directly exposed to high-energy pulsed electrical discharges between two submerged electrodes. The high-temperature (>14,000 *K*) plasma channel created by an *EHD* discharge emits ultraviolet radiation, and produces an intense shock wave as it expands against the surrounding water. A simulation of the *EHD* process is presented along with experimental results. The simulation assumes a uniform plasma channel with a plasma that obeys the ideal gas law and the Spitzer conductivity law. The results agree with previously published data. The simulation is used to predict the total energy efficiency, energy partitioning, maximum plasma channel temperature and pressure for the Caltech Pulsed Power Facility (*CPPF*). The simulation shows that capacitance, initial voltage and gap length can be used to control the efficiency of the discharge.

The oxidative degradation of 4-chlorophenol (*4-CP*), 3,4-dichloroaniline (*3,4-DCA*), and 2,4,6 trinitrotoluene (*TNT*) in an *EHD* reactor was explored. The initial rates of degradation for the three substrates are described by a first-order rate equation, where k_0 is the zero-order rate constant that accounts for direct photolysis; and k_1 is the first-order term that accounts for oxidation in the plasma channel region. For *4-CP* in the 4.0 *L* reactor, the values of these two rate constants are $k_0 = 0.73 \pm 0.08$ μM, and $k_1=(9.4 \pm 1.4) \times 10^{-4}$. For a 200 μM *4-CP* solution this corresponds to

an overall intrinsic zero-order rate constant of 0.022 $M\ s^{-1}$, and a *G*-value of 4.45×10^{-3}.

Ozone increases the rate and extent of degradation of the substrates in the *EHD* reactor. Combined *EHD*/ozone treatment of a 160 μ*M TNT* solution resulted in the complete degradation of *TNT*, and a 34 % reduction of the total organic carbon (*TOC*). The intrinsic initial rate constant of *TNT* degradation was 0.024 $M\ s^{-1}$. The results of these experiments demonstrate the potential application of the *EHD* process for the treatment of hazardous wastes.

Contents

List of Figures

List of tables

1 Introduction

1.1 Motivation

The elimination of toxic and hazardous chemical substances such as halogenated hydrocarbons from waste effluents and previously contaminated sites has become a major national and international concern. Each year, as many as 14,000 installations in the United States generate more than 540 million metric tons of hazardous solid and liquid waste. Some of the hazardous wastes that are stored in holding ponds or discharged within landfills eventually contaminate ground and surface waters. Groundwater contamination is likely to be the primary source of human contact with toxic chemicals. Some specific chemical compounds of interest are: 4-chlorophenol, pentachlorophenol, trichloroethylene (*TCE*), perchloroethylene (*PCE*), carbon tetrachloride, *PCB*'s, dioxins, dibenzofurans, chloroform, methylene chloride, ethylenedibromide, vinyl chloride, ethylene dichloride, methyl chloroform, p-chlorobenzene, and hexachlorocyclopentadiene. The occurrence of chlorinated hydrocarbons and chlorofluorocarbons and other grease-cutting agents in soils and groundwaters is widespread.

These environmental problems have sparked a renewed interest in novel technologies for toxic waste remediation known as advanced oxidation technologies (*AOT*s). Some modern approaches beyond conventional physiochemical treatment and high temperature incineration that have been applied at a commercial level include chemical oxidation with UV light, membrane separation, activated carbon adsorption, substrate-specific biodegration and anaerobic digestion, amended

activated sludge digestion, and fixed-bed high-temperature catalytic reactors. Some newer technologies that exist at an experimental stage include electron beam bombardment, super-critical fluid extraction and oxidation, steam gasification, ultrasonic degradation, and semiconductor photocatalysis.

Several *AOT*s involve the introduction of energy into aqueous solution via non-thermal processes. TiO_2 photocatalysis [1], electron-beam irradiation [2,3], sonochemistry [4-7], and $UV/O_3/H_2O_2$ photolysis [8] are examples of this strategy. One novel technique which has just started to be explored in this regard is the use of pulsed-plasma discharges in aqueous solutions. The electrohydraulic discharge process (*EHD*) is a non-thermal treatment technology that injects energy into an aqueous solution through a plasma channel formed by a high-current/high-voltage electrical discharge between two submersed electrodes [9-15]. The EHD process induces a variety of physical effects that may be exploited for the breakdown of chemical compounds dissolved or suspended in water. They include a high-temperature, high-pressure plasma, an exploding gas-plasma bubble, shock waves, and electromagnetic radiation, including UV and VUV rays.

We have initiated an investigation of the EHD process in the context of hazardous waste remediation. The goal of this program is to measure the chemical effects of pulsed-plasma discharges on selected compounds and to determine the physical origin of induced chemical changes. In this thesis, we use a mathematical simulation to explore the physical nature of extreme conditions that occur during pulsed plasma discharge. We also examine the chemical mechanisms associated with these conditions using the Caltech Pulsed Power Facility (*CPPF*) This facility consists of a large reactor and electronics capable of generating the pulses necessary to induce

electrohydraulic discharges. The goal is to evaluate the EHD process as a method for the treatment of hazardous wastes.

We are motivated by the potential application of the EHD process technology for the rapid degradation of a wide range of halogenated hydrocarbons in water. Present techniques are not totally effective, they are very often cost-intensive and inconvenient to apply to mixed solid-liquid waste, and they are not readily adapted to a wide variety of conditions. EHD process techniques have the potential to be more efficient and adaptable, and appear to be ideally suited for solid-liquid solutions. In addition, EHD technology may be readily coupled with existing technologies to maximize overall treatment efficiency [32].

1.2 General Background

The EHD process [18-26] is a technology that has the potential for the cost-effective treatment of hazardous waste. This process is an adaptation of an existing technology which has been used in a variety of other applications such as in the manufacture of beer cans and automobile springs [16] and in the destruction of kidney stones via focused high-pressure shock waves [18,27,28]. Pulsed-plasma discharge systems have also been used to knock barnacles off marine structures, to form high strength metal alloys, to simulate underwater explosions [15], and to pressure-test cannon bores.

Pulsed-power discharge into water or water-solid slurries is an electrohydraulic phenomenon characterized by a periodic rapid release of accumulated electrical energy across a submerged electrode gap. A typical pulsed-power system is illustrated schematically in Figure 1.1 where the discharge circuit is represented by an

RLC circuit. The power source is a bank of charged capacitors capable of delivering a high voltage, high amperage electrical current to the submerged electrodes. Each electrical discharge produces a short burst of energy at a high power density within the electrode gap, generating a channel containing a highly ionized and pressurized plasma that has the ability to transfer energy to wastewater via dissociation, excitation, and ionization (e. g. H_2O^+, e_{aq}, $\cdot OH$, $H^\cdot$, etc.) with a corresponding increase in temperature. The plasma produces electromagnetic radiation (typically UV to VUV depending on the amount of energy released) and a high pressure shock wave as it expands and does work against the surrounding fluid. A second shock wave also emanates from the collapse and re-expansion of the gas bubble that appears after the discharge ceases and the plasma cools off [15]. If the propagating shock waves are reflected back from either a free surface or from a material with a different acoustic impedance, intense cavitation occurs [30] with the associated chemical changes known from the field of sonochemistry. Thus, a pulsed-power discharge in water provides a highly efficient method for promoting pyrolytic, $\cdot$ OH radical, aquated electron and UV-promoted reactions in water or soil-water slurries.

Additional reaction pathways are likely to result from the direct reactions of the hydrated electrons [31] due to the release of high energy UV radiation from the energized plasma. In addition, the intense cavitation events induced by the shock waves emanating from the plasma discharge can be used to destroy halogenated hydrocarbons by sonochemical mechanisms, and to disinfect wastewater by killing bacteria and viruses [20-23]. In addition, the EHD process also has the potential to separate suspended and dissolved solids from water due to the rapidly expanding and cooling plasma gases present inside the post-discharge bubble with the chemical substrates of interest, and from indirect production of $\cdot OH$ radicals and extremely high pressures which dramatically shift chemical equilibria. If very high energy

discharges takes place in a small enough reactor at short intervals, there is also the possibility for water to exist in the supercritical phase long enough to allow super-critical fluid oxidation [28].

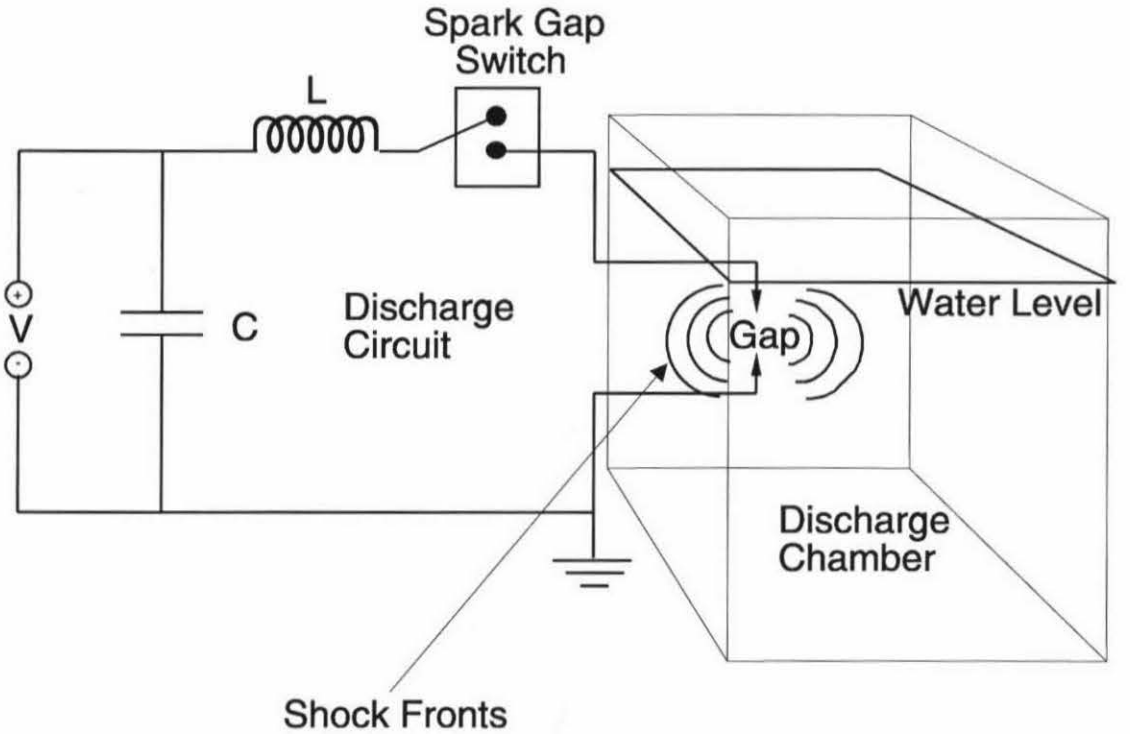

Figure 1.1
Typical Setup for generating pulsed plasma discharges. A capacitor bank C is charged to the desired voltage. The circuit is then discharged across an underwater spark gap. To ensure efficient shock wave production, a fast spark gap switch is used to close the circuit.

The decontaminating effects of the EHD generated UV radiation and shock waves on liquids have been studied previously [20-23] in the context of the removal of micro-organisms. In these cases, UV radiation was found [20-23] to play the central role in decontamination, while the shock waves were determined to have no decontaminating effects. However, Gilliland and Speck [22] were able to measure some specific chemical effects due to shock waves. Unfortunately, this study was limited in that only very weak shock waves (≤ 100 *bars*) were used. In addition, none

of these studies considered cavitation as one of the possible physical mechanisms for bactericide or chemical effects. Hence, these studies are only of limited value in a full understanding of the mechanisms leading to chemical breakdown using the Caltech Pulsed Power Facility.

The Caltech Pulsed Power Facility (CPPF) has electronics capable of generating efficient shock waves and UV producing discharges over a broad range of energies. The CPPF is similar to systems which have been built specifically for the purpose of metal forming, barnacle removal off marine structures, forming high strength metal alloys [16], electrohydraulic pumping, and pressure-testing cannon bores. The CPPF system allows the variation of energy from 500 *joules* to 32 *kilojoules* per discharge by varying the charging voltage from 5 to 25 *kV*. In principle, the capacitance can also be changed from 15 to 135 μF in 15 μF steps, but such changes require that other circuit parameters be updated as well.

1.3 Research Objectives

In this study, a general model is proposed to predict the manner in which the energy partitions into the various processes of the underwater discharge. The model should be simple to use and should generate insight into the details of the physical processes involved in the energy transfer phase. Such a thorough understanding of the physics of the underwater discharge is necessary to fully understand and optimize the chemical changes it induces.

The model allows us to simulate the plasma channel dynamics, and can be used to reconstruct a complete picture of the physical effects generated by the discharge using only a limited set of physical measurements which are practical in an industrial

setting. The model will be developed on the basis of current knowledge of the behavior of the cold plasmas that are typically found in underwater discharges.

1.4 Approach

The purpose of this section is to provide an overview of the remaining chapters of this thesis. A derivation of the ordinary, non-linear equations that predict the plasma channel dynamics is presented in Chapter 2. The main physical principles from fluid mechanics and plasma physics on which the derivation is based are summarized in the appendices for quick reference. The numerical solutions of the equations that make up the simulation are presented in Chapter 3, where the results are also compared to previously published experimental data [9,11]. Chapter 4 outlines an analytical solution to the equations derived in Chapter 2 under simplified assumptions.

In Chapter 5, the simulation is applied to make predictions for the Caltech pulsed power facility. The energy partition and maximum pressures and temperatures as a function of different EHD parameters are presented. These results show how to control and vary the electromagnetic and shock wave radiation intensity, and exploding bubble size in order to optimize the chemical effects for different classes of compounds.

Chapter 6 describes the Caltech pulsed power facility and the data acquisition system, and presents experimental results which focus primarily on radiation effects and the plasma channel itself. Some preliminary experimental results focusing primarily on the effects of shock waves are given in Appendix D, which outlines some chemical data obtained using a lithotripsy setup with focused shock waves.

Finally, Chapter 7 summarizes the key accomplishments of this research program and presents some concluding remarks. Other issues important in optimizing EHD processes are presented, along with recommendations for future research.

References

[1] Hoffmann, M. R.; Martin, S. T.; Choi, W. Y.; Bahnemann, D. W. *Chemical Reviews* **1995**, *95*, pp. 69.

[2] Penetrante, B. M.; Schultheis, S. E.; Eds. *Non-Thermal Plasma Techniques for Pollution Control Part A: Overview, Fundamentals and Supporting Technology*; Springer-Verlag: New York, 1993.

[3] Penetrante, B. M.; Schultheis, S. E.; Eds. *Non-Thermal Plasma Techniques for Pollution Control Part B: Electron Beam and Electrical Discharge Processing*; Springer-Verlag: New York, 1993.

[4] Kotronarou, A.; Mills, G.; Hoffmann, M. R. *J. Phys. Chem* **1991**, *95*, pp. 3630.

[5] Hua, I.; Höchemer, R.H.; Hoffmann, M. R. *Environ. Sci. Tech.* **1995**, (In Press).

[6] Hua, I.; Höchemer, R. H.; Hoffmann, M. R. *J. Phys. Chem.* **1995**, *99*, pp. 2335.

[7] Serpone, N.; Terzian, R.; Hidaka, H.; Pelizzetti, E. *J. Phys. Chem.* **1994**, *98*, pp. 2634.

[8] Legrini, O.; Oliveros, E.; Braun, A. M. *Chem. Rev.* **1993**, *93*, pp. 671.

[9] Martin, E.A. *J. App. Phys* . **1960,** *31* 255-265.

[10] Robinson, J. W. *J. Appl. Phys.* **1967**, *38*, pp. 210.

[11] Robinson, J. W.; Ham, M.; Balaster, A. N. *J. App. Phys* . **1973,** *44*, pp. 72.

[12] Robinson, J. W. *J. Appl. Phys.* **1973**, *44*, pp. 76.

[13] Naugolnykh, K. A.; Roy, N. A. *Electrical Discharges in Water. A Hydrodynamic Description.* technical report FTD-HC-2049-74, Foreign Technology Division, Wright-Patterson Air Force Base, Ohio. 1974.

[14] Radovanov, S. B. *A Spectroscopic and Thermodynamic Study of Pulsed Underwater Discharges*. In: *The Physics of Ionized Gases*; Tanovic', L.; Konjevic', N.; Tanovic', N. Eds. Nova Science Publishers: 1988.

[15] Buntzen, R. R. The Use of Exploding Wires in the Study of Small-Scale Underwater Explosions. *Exploding Wires, Vol 2;* Chace, W. G.; Moore, H. K. Eds. Plenum Press: New York, NY, 1962; pp. 195.

[16] Smith, K. F. *Electro-Hydraulic Forming*. In: *High-Velocity Forming of Metals*; Wilson, F. W. Ed. Prentice Hall: Englewood Cliffs, N. J. 1964; pp. 77.

[17] Coleman, A. J.; Saunders, J. E.; Crum, L. A.; Dyson, M. *Ultrasound in Med. & Biol.* **1987**, *13*, pp. 69.

[18] Simpson, D. Electrohydraulics - A review of the E.C.R.C. Research Programme 1970-1977 Electricity Research Council Publication ECRC/R1336. Great Britain 1980.

[19] Weldon, W. F. *IEEE Spectrum*, **1985**, 59-66.

[20] Edebo, L.; Selin, E. *J. Gen. Microbiol.* **1968**, *50*, 253-259.

[21] Gilliland, S.E.; Speck, M.L. *Applied Microb.* **1967,** *15*, 1031-1037.

[22] Gilliland, S.E.; Speck, M.L. *Applied Microb.* **1967,** *15*, 1038-1044.

[23] Stirling, R. Disinfection by Electrohydraulic Discharges, Electricity Research Council Publication ECRC/M508 Great Britain 1972.

[24] Clements, J.S.; Sato, M.; Davis, R.H. *IEEE Trans. Ind. Appl.*, **1987,** *IA-23*, pp. 224.

[25] Lee, W.M. *J. Appl. Phys.* **1990,** *69*, pp. 6945.

[26] Goryachev, V.L.; Remennyi, A.S.; Silin, N.A. *Sov. Tech. Phys. Lett.*, **1990,** *16*, pp. 439

[27] Chaussy, C. *Extracorporeal Shock Wave Lithotripsy* , Karger, Basel 1986, pp. 155.

[28] Gravenstein, J.S. Peter, K. *Extracorporeal Shock Wave Lithotripsy for Renal Stone Disease*, Butterworths, Boston, 1986, pp. 158.

[29] Franck, E.U. et al. Supercritical Water: A Medium for Chemistry *Engineering and Science News*, December 23, 1991.

[30] Muller, M. Focusing of Shock Waves in Water by Different Ellipsoidal Reflectors *AIP Conference Proceedings 208,* **1989** *Current Topics in Shock Waves* pp. 143

[31] Hart, E. J.*The Hydrated Electron* New York, 1970 Wiley-Interscience.

[32] Hoffmann, M. R.; Höchemer, R. H.; Kratel, A.W. H.; Lang, P. S.; Willberg, D. M. *Environmental Science and Technology* **1996** (In Press).

2 Theoretical Development of the General Dynamic Equations for the Underwater Plasma Channel

2.1 Introduction and Motivation

The primary aim of this chapter is to present a clear and concise derivation of the equations necessary to simulate the underwater plasma channel which is present during a discharge event in the electrohydraulic discharge process (*EHD*). The equations consist of conservation principles and of relations which describe the medium properties of the plasma itself. Any derivations that were deemed too lengthy have been included in the appendices for reference. The numerical solutions to the equations derived here are described in chapter 3, and are applied to the prediction of the energy partition in chapter 5. The basic equations lend themselves to a simple analytical solution which is outlined in chapter 4.

Prior to beginning work on the simulation, it is necessary to choose one of two alternative approaches to describe the dynamics of the underwater discharge. One approach is to solve the problem on a finite element grid where interactions take place between infinitesimal pieces of the medium, and no a priori distinction has to be made between the plasma medium inside the channel and the surrounding water medium. In contrast, the approach used in this simulation assumes the existence of a two-phase medium with a distinct boundary, and that the properties of the plasma inside the channel are uniform. Computational speed and physical simplicity are among the many advantageous features this approach offers.

The two-phase approach requires significantly less computation than the finite element approach for two reasons. The two-phase description leads to a set of non-linear ordinary differential equations that can be rapidly solved using standard numerical methods [1], whereas the finite element approach leads to a set of partial differential equations which require considerably more complex algorithms. Furthermore, choosing a finite element approach would require using an equation of state that describes a continuous transition from liquid water at room temperature to a cool 1-2 eV^* high pressure plasma [2,3]. Although data is available to deduce such a relation, it would unnecessarily further complicate the algorithm [21]. In contrast, the two-phase description allows for the use of a simpler equation of state for the plasma at high temperatures.

The computational speed and the physical simplicity of the two-phase approach are two features which simplify our work on reaction kinetics in the *EHD* reactor at Caltech. Such experiments require at least 100 successive shots per run [4]. Under these circumstances, it would be unrealistic to perform physical measurements within the chamber for each successive shot, given the extreme physical environment. Pressures reaching magnitudes well above 1 *kbar* per discharge [5-8] rule out the repetitive use of transducers, since any transducer would loose its calibration after only one discharge. Similarly, optical measurements require that the plasma channel take a particular, pre-determined path. This can only be accomplished with the use of exploding wires [9]. Such an approach would be impractical in an experiment requiring rapid successive discharges. Thus, a reliable model that can calculate the

---

* An eV is a unit of temperature commonly used in plasma physics. For example, 1/40 eV represents room temperature.

approximate physical conditions induced in the chamber by the discharge becomes a useful tool to guide our physical intuition regarding the chemical kinetics taking place.

2.2 Physical Description of the Discharge

A typical setup for an underwater discharge consists primarily of a capacitor bank charged to a given voltage, a fast switch, and an underwater spark gap, as illustrated in Figure 2.1. After the capacitor bank is charged to a given voltage, the fast switch is closed, and the charge stored in the capacitor bank is discharged across the underwater gap.

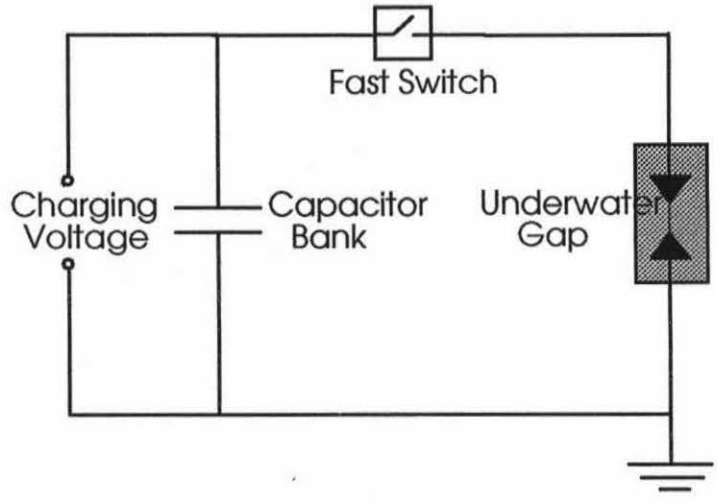

Figure 2.1
Schematic illustration of a typical setup to generate an electro-hydraulic discharge. After the capacitor bank is charged to a given voltage, the fast switch is closed, and the charge stored in the capacitor bank discharges across the underwater gap.

The underwater discharge can be separated into three distinct temporal phases as illustrated in Figure 2.2. Initially, when the switch in the circuit closes, and a voltage builds across the underwater electrodes, a discharge initiation phase takes place

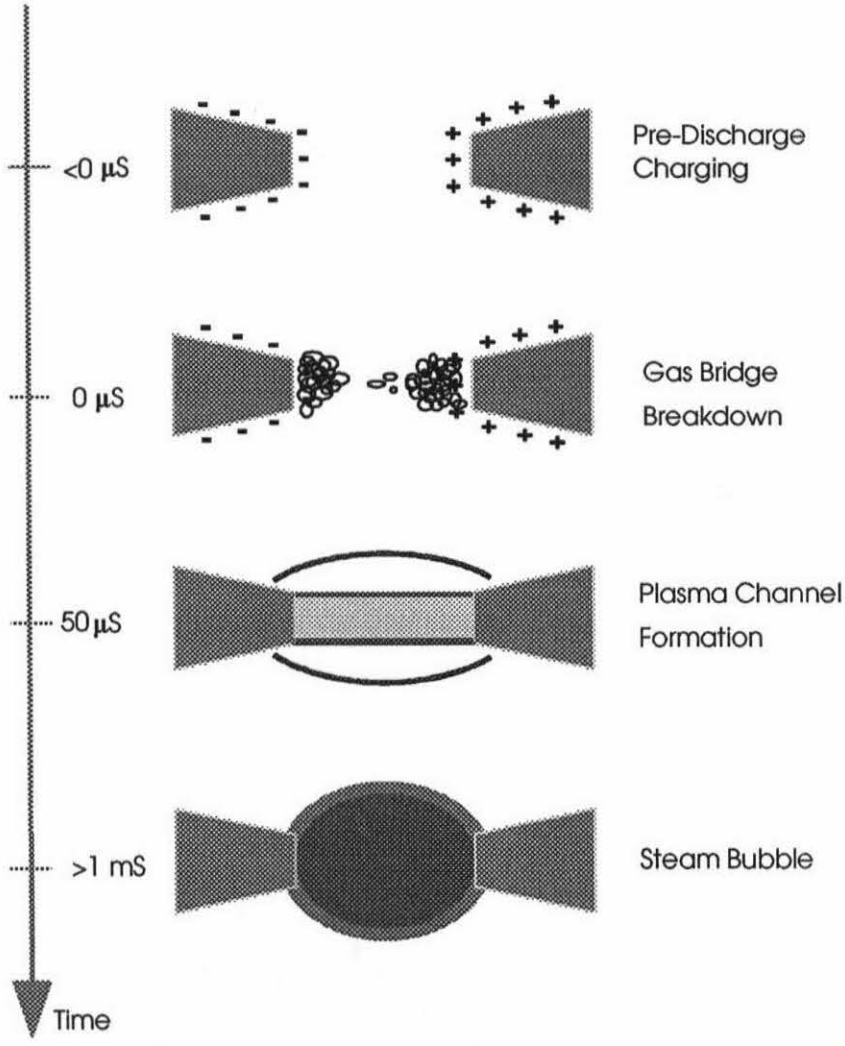

Figure 2.2
Schematic illustration of the dynamics of an underwater discharge generated by a low-voltage discharge. A gas-bridge must form before the plasma channel can be established. Once the energy transfer is completed and heat transfer processes take place, the plasma channel is replaced by a large steam bubble.

during which a plasma channel forms. For low electric field strengths, which are typical of low voltage (<50 *kV*) discharges, the plasma channel forms only once a gas phase bridge [10] is established across the electrodes. This bridge forms as a result of conduction-induced water evaporation. During the energy transfer phase, the bulk of

the energy stored in the capacitor dissipates into the plasma channel. The plasma channel in turn does work against the surrounding fluid as it expands, and in the process, generates a shock wave. Some of the energy is released as blackbody radiation with channel temperatures reaching above 20,000 K [9,11,12]. The resulting radiation wavelengths range from the infrared well into the short ultraviolet. During the energy transfer phase, energy losses due to heat conductivity are negligible [9], since the time scales involved are much too fast. Figure 2.3 illustrates that when heat conductive processes become significant, the discharge enters its final phase. Heat conduction, along with the acoustic and electromagnetic radiation that fails to escape, now contribute to the formation of the final steam bubble, which surrounds the plasma channel, and gradually replaces it.

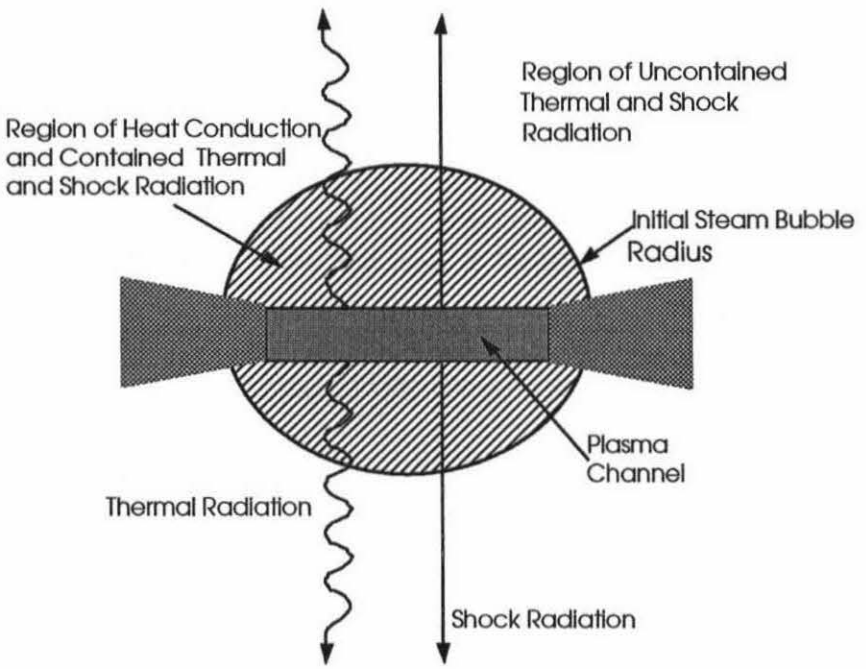

Figure 2.3

Schematic illustration of the formation of the steam bubble. Heat conduction processes, along with the acoustic and electromagnetic radiation that fails to escape into the bulk medium, contribute to heating the water surrounding the plasma channel and thus a steam bubble is formed. The plasma channel then dissipates gradually as it is completely replaced by a steam bubble.

The fluid-mechanical behavior of the bubble is typical of the types of bubbles encountered in underwater explosions [13,14]; the bubble reaches its maximum size within the first 30 milliseconds, and then collapses again. Upon collapse, one may detect another burst of radiation [14], which this time, corresponds to the sonoluminescence [15] associated with the adiabatic heating of the gas compressed during the collapse. As the bubble re-expands, it radiates a new shock pulse. This secondary shock wave, which is not associated with the plasma expansion process, is referred to as the "cavitation shock wave." The bubble will then continue to oscillate several times, gradually dissipating the remainder of its energy in the forms of viscous friction and acoustic radiation [14]. The maximum size of the bubble can be calculated from the amount of energy E_B partitioned into the bubble process as shown in eq 2.1 [13]:

$$E_B = \frac{4}{3}\pi P_a a_{\max}^3, \qquad 2.1$$

where P_a is the ambient pressure, and a_{max} is the maximum radius of the explosion bubble. The energy E_B can be calculated as the difference between the total energy transferred into the plasma channel and the energy dissipated into the shock waves and radiation.

In summary, the plasma channel partitions the energy from the capacitor bank into three different channels as illustrated by Figure 2.4: the shock wave, electromagnetic radiation, and the final steam bubble. The actual values given in Figure 2.4 are typical of an underwater discharge that has been optimized for shock wave generation. The actual energy partitioning can be controlled by varying the parameters of the discharge as will be shown in Chapter 5.

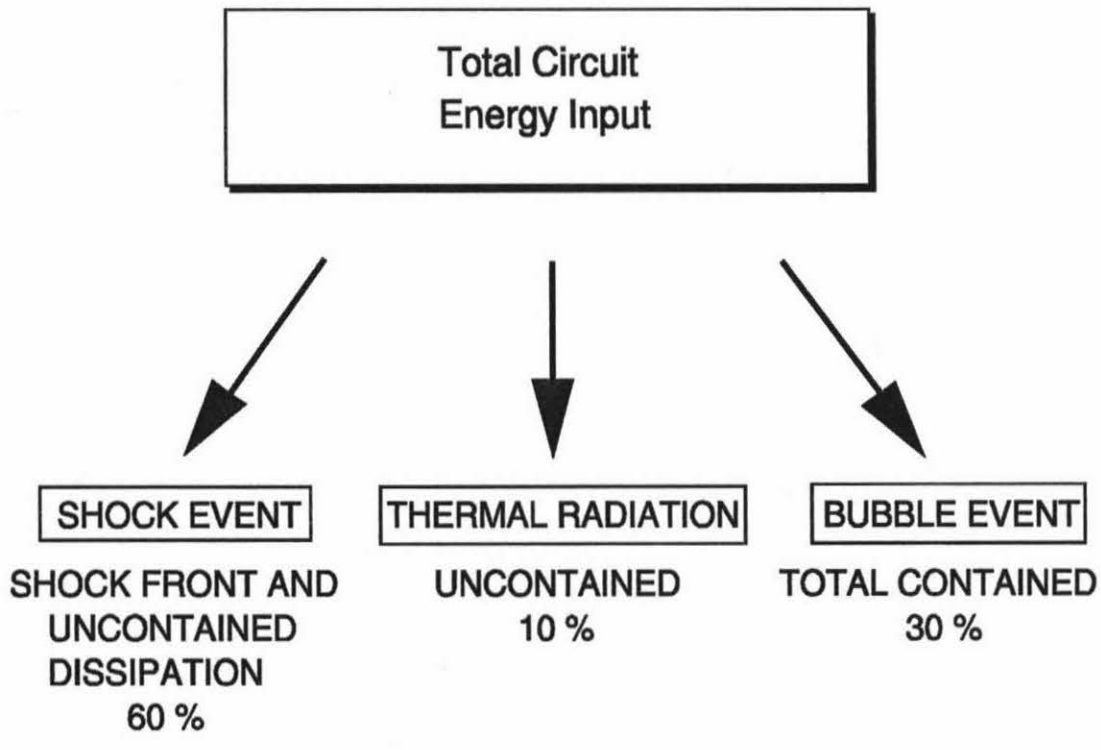

Figure 2.4
Energy partition diagram at time of maximum bubble radius and approximate percentages for a typical discharge that has been optimized to generate shock waves. (From Reference [14])

2.3 Formulation of the Fundamental Equations

Before embarking on any formal mathematical manipulations, it is wise to lay out some notational conventions to avoid any confusion. Unless denoted by an explicit time dependence *(t)*, all symbols that are not denoted by a Latin letter with a subscript, or by a Greek letter with or without a subscript, are time dependent. For example, P represents the pressure $P(t)$ which is a function of time, while P_a, as used in eq 2.1 above represents, a constant value, the ambient pressure of 1 *bar*. Please note that all symbols used in this or any other chapter of this thesis are listed in Appendix A for quick reference.

The equations derived below describe the phase, during which the bulk of the energy dissipates into the plasma channel. Many of the previously published models of this phase of the underwater discharge, [16-20] focus primarily on the electro-hydraulic effect and assume a constant temperature throughout the energy transfer phase, which in effect neglects the temperature dynamics. A notable exception is the work of Robinson [21], which focuses primarily on the radiative aspects of the discharge using a finite-element model. Our formulation of this phase of the discharge, as an initial value problem, includes both the shock waves and the resulting electromagnetic radiation with a varying plasma channel temperature. This formulation unites the fluid mechanics and the plasma physics of the discharge into one set of non-linear ordinary differential equations. We favor a macroscopic averaging procedure over a finite-element simulation [21] primarily because a macroscopic model leads to ordinary differential equations and retains physical simplicity without sacrificing predictive properties.

A complete set of basic equations describing the behavior of the underwater plasma channel can be readily derived from conservation principles such as the conservation of energy, momentum and mass. We represent the plasma with a cylindrical geometry of radius a and length ℓ, filled with N ionized gas particles at pressure P and temperature T with an internal energy density W, as shown in Figure 2.5. V denotes the volume, which is given by $\pi a^2 \ell$, and S denotes the surface area, which is given by $2\pi a \ell$. I denotes the current flowing through the plasma channel.

In an actual experiment, only discharges initiated by exploding wires will take on a uniform cylindrical geometry [9]. For discharges initiated without the help of exploding wires, the plasma channel will follow a random path between the electrodes,

only approximating a cylindrical discharge. We assume that a uniform, straight channel still holds to first order.

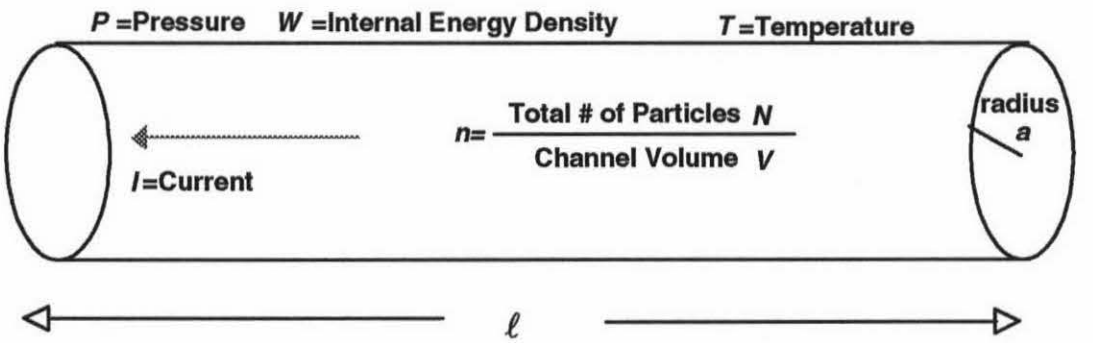

Figure 2.5

Schematic illustration of the plasma channel that has a cylindrical geometry of radius a and length ℓ and is filled with N ionized gas particles at pressure P and temperature T with an internal energy density W. V denotes the volume, S denotes the surface, and I denotes the current flowing through the plasma channel.

The energy transferred from the circuit to the plasma channel is partitioned into three processes as illustrated by eq 2.2: the mechanical work exerted on the surrounding fluid as the plasma channel expands, the internal energy of the plasma itself, and electromagnetic radiation as the channel temperature increases.

$$\frac{dE_d(t)}{dt} = \frac{d}{dt}(WV) + P\frac{dV}{dt} + (1-f)\sigma_B T^4 S. \qquad 2.2$$

Since heat conduction takes place on a much slower time scale than that of the discharge, energy losses due to heat conduction are negligible and hence are not included in eq 2.2. Once heat conduction processes begin to dissipate energy, the transfer of energy from the capacitor will have long since ceased, and the discharge will already be in its final phase. During this phase, the plasma channel cools down

and becomes a steam bubble. This phase of the discharge is beyond the scope of our simulation.

The term on the left side of eq 2.2 represents the rate at which energy is transferred from the capacitor bank to the plasma channel . The first term on the right describes the rate of change of the internal energy state of the plasma channel; W denotes the internal energy per unit volume of the plasma as a function of time. The second term on the right represents the work PdV exerted by the channel on the surrounding fluid where P is the pressure of the plasma, and V is the volume of the plasma channel. The last term on the right represents the radiative transfer from the plasma channel into the surrounding liquid phase: σ_B is the Stephan-Boltzmann constant, S is the surface of the plasma channel, and T is the temperature of the plasma. Implicit in this term is the assumption that the plasma channel behaves as a blackbody radiator [9,11,12,21]. Some of the radiation actually never escapes the plasma channel, as denoted by the factor $(1-f)$. f represents the fraction of the radiation spectrum that is absorbed in a surrounding thin layer of liquid. This thin layer is then vaporized and reincorporated into the plasma. The energy lost in this vaporization process is thus returned to the plasma channel along with the recently absorbed thin layer of fluid .

Although no energy is lost in the ionization process at the plasma channel surface, the resulting particle flux is non-negligible and contributes to the mass balance of the plasma channel. Since the plasma continually inducts particles from the channel walls into the main body of the plasma, the number of particles N in the plasma channel is not constant, as illustrated by eq 2.3:

$$\frac{dN}{dt} = \frac{fS\sigma_B T^4}{\varepsilon_{vaporization}}, \qquad 2.3$$

where $fS\sigma_B T^4$ is the radiative energy absorbed by the layer of fluid that is to be inducted into the plasma channel, N is the total number of particles in the plasma channel, and, $\varepsilon_{vaporization}$ is the energy per particle required to vaporize the surrounding liquid into the plasma. This liquid is further ionized and becomes part of the plasma. f is the fraction of the radiation spectrum absorbed in the fluid layers immediately surrounding the plasma channel, as was previously defined for eq 2.2, Although these layers contribute to geometrically negligible [11] increases in the channel radius, the resulting particle flux is high enough to offset and even reverse the expected density decrease resulting from the plasma channel expansion.

The pressure discontinuity at the plasma channel boundary has to be addressed using the equations of fluid mechanics. As far as the surrounding fluid is concerned, the plasma channel is nothing more than an expanding cylindrical piston. A simple relation between the pressure on the surface of the channel and the channel wall velocity can be obtained from the Rankine-Hugoniot relations for a shock front [23];

$$(P+\beta)^{3/7} = \left(\frac{3\sqrt{\rho_o}}{\sqrt{7}\alpha^{1/14}}\right)\frac{da}{dt} + \beta^{3/7}, \qquad 2.4$$

where a is the radius of the plasma channel. Eq 2.4 relates the pressure on the surface of the channel to its expansion velocity. The full derivation of this relation is included in Appendix B for reference. Even though this relation involves some degree of approximation*, its validity is not restricted to expansions that are slower than the

* The derivation does not use the Rankine-Hugoniot relation for energy since a shockwave must reach at least 100 kbars before any appreciable temperature changes occur across the shock wave in water.

speed of sound. The constants α, β and ρ_0 are the same ones used in the Tate equation of state for shock waves in water [23], which is given by eq 2.5 below:

$$P = \alpha\left(\frac{\rho}{\rho_o}\right)^7 - \beta, \qquad 2.5$$

where α=3001 *bars*, β = 3000 *bars*, and ρ_0=1$g\ cm^{-3}$. This equation is valid only for shock waves below 100 *kbars* and at temperatures close to 300 *K*. Both of these requirements are satisfied since pressures in the plasma channel do not exceed 20 *kbars*, and the temperature gradient at the plasma channel boundary is very sharp [12,21]. Thus, we may assume that the surrounding fluid is at ambient temperature.

To complete our set of equations, we must couple equations 2.2 through 2.4 with the equivalent discharge circuit illustrated in Figure 2.6. The plasma channel can be modeled as a resistor with a time-varying resistance *R* undergoing Ohmic heating. We apply Kirchoff's law by summing the potentials across the circuit:

$$L_c \frac{dI}{dt} + [R_c + R]I + \frac{q}{C_b} = 0, \qquad \frac{dq}{dt} = I, \qquad 2.6$$

where L_c is the inductance of the circuit, and C_b is the capacitance of the energy storage bank. The inductance and the capacitance of the plasma channel are negligible. *R* is the time-varying resistance of the plasma channel itself, given by

$$R = \frac{\ell}{\sigma_{cond}(t)\pi a^2}, \qquad 2.7$$

where $\sigma_{cond}(t)$ is the conductivity of the plasma channel as described in the next section. R_c is the constant equivalent resistance of the circuit. Its main effect is to

dissipate some of the energy that would otherwise be transferred to the underwater gap. Of the total energy in the capacitor bank $E_b = \frac{1}{2} C_b U_o^2$ (where U_o is the initial charging voltage,) only a fraction eventually makes it to the underwater gap.

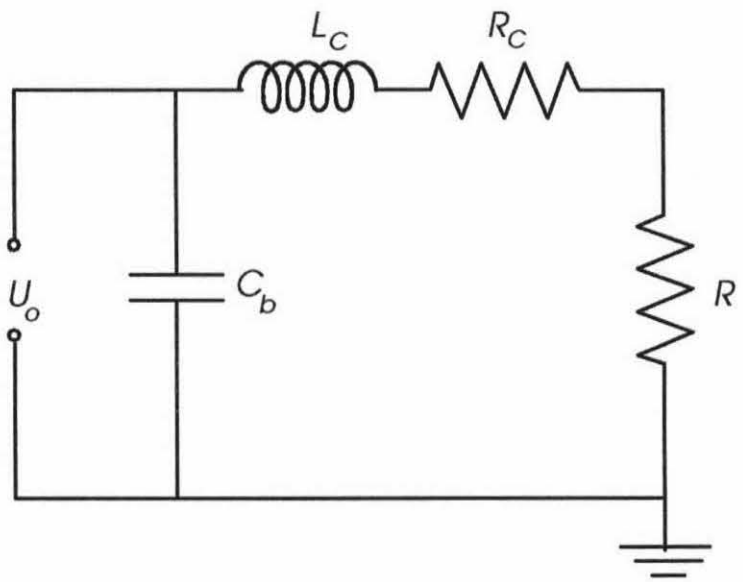

Figure 2.6
Equivalent circuit for the discharge analysis. R represents the discharge channel resistance, L_c and R_c represent the equivalent circuit inductance and resistance, respectively. C_b is the capacitance of the storage bank, and U_o is the initial charging voltage. The capacitance and inductance of the plasma channel are negligible.

In terms of Figure 2.6, the rate of energy transfer from the circuit to the plasma channel is thus given as

$$\frac{dE_d}{dt} = RI^2, \qquad 2.8$$

where RI^2 is the power dissipated across the plasma channel. Eq 2.8 effectively couples the discharge circuit with the underwater plasma channel dynamics via the plasma channel resistance R.

2.4 Description of the Plasma Medium

To complete our set of equations, we must give a full description of the medium, consisting of the equation of state of the plasma, and relations for both the internal energy and the conductivity of the plasma channel.

2.4. 1 The Equation of State

One of the advantages of a two-phase model is that we do not need an equation of state that is valid for water both in the liquid state and in the dissociated and ionized plasma state. Hence we may use the ideal gas law to describe the plasma:

$$P = nkT. \tag{2.9}$$

Eq 2.9 assumes the pressure is a result of kinetic interactions only and neglects both Coulomb inter-particle interactions and the Pinch effect, the correction in pressure due to the interaction of the charged particles with their own magnetic field. These effects require corrective terms to be added to eq 2.9:

$$P = nkT - \Delta P_{Pinch} - \Delta P_{Coulomb}, \tag{2.10}$$

where the Pinch effect correction is given by

$$\Delta P_{Pinch} = \frac{\mu_o I^2}{8\pi^2 a^2}. \qquad 2.11$$

The Coulomb interaction correction can be calculated using the following expression:

$$\Delta P_{Coulomb} = \frac{e^2}{32\pi^2 \varepsilon_o}\left(\frac{4\pi n}{3}\right)^{4/3}. \qquad 2.12$$

Eq 2.12 assumes that the Debye shielding distance is larger than the mean distance between ions. Martin [9] gives a Debye length of 4 Å, while the mean distance in between ions is actually 10 Å. Since the Debye length is the distance beyond which only collective forces exert any effects on individual particles, the use of eq 2.12 is justified.

For discharges such as those expected in the Caltech Pulsed Power Facility (CPPF), the pinch effect is negligible. If we take for example a 135 μF discharge with a gap of 8 *mm* and an initial voltage of 15 *kV*, the current typically reaches on the order of 120 *kA* with a plasma channel radius of 2.5 *mm*. The Pinch effect then amounts to a correction of 350 *bars*, which is negligible compared to the 8 *kbars* contributed by the kinetic pressure.

The Coulomb effect is slightly more pronounced and, therefore, should be included. But even for the highest energy discharges the CPPF can generate, the correction is not very large. Figure 2.7 illustrates the dependence of the Coulomb effect on the plasma particle density. Typical discharges below 20 *kjoules* do not reach particle

densities beyond 2-3x10^{27} *particles/m^3*. Hence, we can expect at most a 20% correction effect for the highest possible CPPF discharge.

Both the Coulomb interactions and the Pinch effect will effectively dampen the plasma channel expansion governed by eq 2.4, and increase the energy density as a direct consequence of lower channel radii, and by lowering the *PdV* losses term in eq 2.2. Higher energy discharges with higher current densities thus do not necessarily generate stronger shock waves. The equations and the numerical solution generator described in Chapter 3 have been formulated so that the corrections to the equation of state can be readily turned on or off by modifying the function for the pressure, depending on which type of discharge is being simulated (see the next chapter).

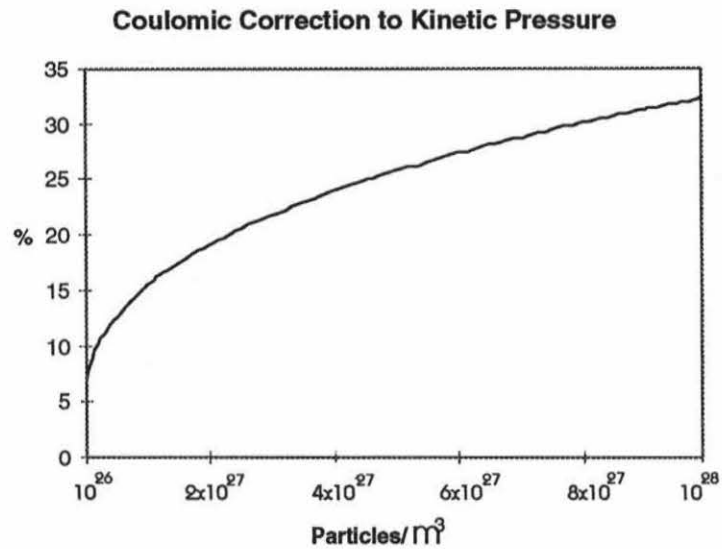

Figure 2.7
Coulombic correction $\Delta P_{coulomb}/P$ to the pressure of the plasma channel as a function of its particle density. The effect is small yet not negligible for particle densities typical of 1-20 *kJ* discharges.

2.4. 2 The Internal Energy Relation

Both Ioffe et al. [11] and Martin [9] have shown from theoretical calculations that the plasma internal energy is directly proportional to the pressure acting on the plasma channel, and is essentially independent of the temperature of the plasma channel within the temperature ranges of interest. The relation is written as

$$W = \frac{1}{\gamma - 1} P, \tag{2.13}$$

where γ =1. 22 [9,11] and P is the pressure of the plasma channel. This relation is based on the ideal gas law and the Saha ionization equation. γ is sometimes referred to as the isentropic index of the plasma. Even though the derivation of eq 2.13 assumes no particle interactions other than kinetic collisions, the relation is found to hold experimentally provided the pressure is replaced by the kinetic pressure $P_{kinetic}=nkT$ [9]. Thus, eq 2.13 becomes

$$W = \frac{1}{\gamma - 1} nKT. \tag{2.14}$$

A more detailed derivation of eq 2.14 is included in Appendix C.

2.4. 3 The Electrical Conductivity Relation

Spitzer [22] shows that in the presence of a magnetic field, a fully ionized plasma has a conductivity proportional to $T^{3/2}$. The conductivity resulting from thermal collisions alone is proportional to $T^{5/2}$. For our purposes, a semi-empirical relation is much more useful since our plasma will not necessarily be fully ionized. A useful relation is given

by Robinson [21] which is reminiscent of Spitzer's [22] formulation, with the addition of an exponential factor:

$$\sigma_{cond} = \xi T^{3/2} e^{-5000/T}. \qquad 2.15$$

In Robinson's [21] finite element analysis, the exponential factor in the above relation produces a plasma channel with well-defined boundaries. Relation 2.15 is essentially an empirical formulation for the conductivity which takes into account the nature of the plasma in the underwater discharge: the constant ξ takes on values on the order of 10^3, and can be adjusted to bring closer agreement with experimental data.

2.5 Summary of the Equations Describing the Discharge

Substituting for the plasma channel volume $V=\pi a^2 \ell$, and the surface area $S=2\pi a \ell$, equations 2.1-2.8 can be reduced to the set of equations below.

Conservation of energy:

$$\frac{I^2}{\sigma_{cond}(t) 2\pi^2 a^3} = (P + W)\frac{da}{dt} + \frac{a}{2}\frac{dW}{dt} + (1 - f)\sigma_B T^4. \qquad 2.16a$$

Conservation of mass:

$$\frac{dn}{dt} = \frac{2}{a}\left(\frac{f\sigma_B T^4}{\varepsilon_{vaporization}} - n\frac{da}{dt}\right). \qquad 2.16b$$

Conservation of momentum:

$$(p+\beta)^{3/7} = \left(\frac{3\sqrt{\rho_o}}{\sqrt{7}\alpha^{1/4}}\right)\frac{da}{dt} + \beta^{3/7}. \qquad 2.16c$$

Conservation of charge:

$$L_c\frac{dI}{dt} + \frac{\ell}{\sigma_{cond}(t)\pi a^2}I + \frac{q}{C_b} = 0, \quad \frac{dq}{dt} = I(t), \quad q(t_o) = CU_o, \qquad 2.16d$$

where α=3001 *bars*, β=3000 *bars* ρ_0=1000 kg/m^3, σ_B=5. 67051x10^{-8} $W/m^2\,{}^oK^4$ and $\varepsilon_{vaporization}$=2.54x$10^{-20}$ *joules/particle*. Note that eq 2.16b was obtained by converting eq 2.3 to particle density *n* rather than total number of particles *N* using the relation

$$N = nV = n\pi a^2\ell. \qquad 2.17$$

The four equations 2.16a through 2.16d describe four explicit time-dependent unknown functions *I(t), T(t), a(t), and n(t)* for the current, temperature, channel radius, and particle density. The equations are formulated in such a way that the properties of the plasma channel can be easily modified. In general, the functions *P*, $\sigma_{cond}(t)$ and *W* are functions of the four unknowns. These relations describe the properties of the plasma, and are given by equations 2.10 through 2.15 which are summarized below:

The equation of state:

$$P(I,T,a,n) = nkT - \frac{\mu_o I^2}{8\pi^2 a^2} - \frac{e^2}{32\pi^2 \varepsilon_o}\left(\frac{4\pi n}{3}\right)^{4/3}. \qquad 2.18a$$

The internal energy:

$$W(I,T,a,n) = \frac{nkT}{\gamma - 1}. \qquad 2.18b$$

The conductivity:

$$\sigma_{cond}(I,T,a,n) = \xi T^{3/2} e^{-5000/T}. \qquad 2.18c$$

The solutions to the equations above are dependent on the parameters ℓ, U_O, L_c, and C_b. The main empirical parameters that can be changed are the isentropic index of the plasma γ, the electrical conductivity proportionality constant ξ, and the fraction f of electromagnetic radiation energy that is reabsorbed into the channel. The full numerical solution to these equations is presented in chapters 3 and 5, and an analytical solution under simplified assumptions is outlined in Chapter 4 .

2.6 Discussion

In any low voltage discharge experiment, there are two significant sources of uncertainty. The parameters ℓ (spark gap length) and U_o (Initial voltage) both vary from shot to shot. In low voltage discharges, the initial voltage is subject to a certain level of uncertainty due to the initial current leakage during the formation of the gas steam bridge through which the final breakdown occurs [10]. At the same time, an

uncertainty in spark gap length is also introduced as the plasma channel usually follows an irregular path through the water.

These introduced uncertainties imply that any model predictions beyond a certain level of precision become useless. This fact justifies our use of the general empirical relations for the plasma given in section 2.4. A more precise model of the plasma would have to take into account the details of the various degrees of ionization of the plasma, and a more detailed description of the induction process, including a factor f which now becomes a function of temperature $f = f(T)$. The function $f(T)$ would be calculated by integrating the fraction of energy radiated at a given temperature into the portion of the electromagnetic spectrum below the water absorption cut-off. The inclusion of such a function requires additional integration steps for each time-step, thus considerably slowing down the algorithm. Such a level of precision becomes unnecessary in the light of the existing uncertainties at the laboratory level. The model presented in this work serves well as a companion to chemical kinetics experiments. Its accuracy is sufficient to predict trends pertaining to chemical efficiency. The model would also be very appropriate for an industrial setting where the only accessible physical data is the current flowing through the plasma channel, and the voltage across the underwater spark gap.

References

[1] Press, W. H. et al., *Numerical Recipes in C : The Art of Scientific Computing* Cambridge [England] ; New York : Cambridge University Press, 1988.

[2] Rice, M.H.; Walsh, J.M. *J. Chem. Phys.* **1957**, *26*, pp. 824.

[3] Keenan, J.H.; Keyes, F.G. *Thermodynamic Properties of Steam*, Whiley, New York, 1936

[4] Hoffmann, M. R.; Höchemer, R. H.; Kratel, A.W. H.; Lang, P. S.; Willberg, D. M. *Environmental Science and Technology* **1996** (In Press).

[5] Buntzen, R. R., The Use of Exploding Wires in the Study of Small-Scale Underwater Explosions. *Exploding Wires, Vol 2;* Chace, W. G.; Moore, H. K. Eds. Plenum Press: New York, NY, 1962; pp. 195.

[6] Smith, K. F. *Electro-Hydraulic Forming*. In: *High-Velocity Forming of Metals*; Wilson, F. W. Ed. Prentice Hall: Englewood Cliffs, N. J. 1964; pp. 77.

[7] Simpson, D. Electrohydraulics - A review of the E.C.R.C. Research Programme 1970-1977 Great Britain 1980 Electricity Research Council Publication ECRC/R1336.

[8] Simpson, D. Shock Wave Generation by Underwater Discharges Great Britain 1974 Electricity Research Council Publication ECRC/N779.

[9] Martin, E. A. , *J. App. Phys.* **1960**, *31,* 255-265.

[10] Naugolnykh, K.A. and Roy, M. A. : Electrical Discharges in Water, A Hydrodynamic Description, Iedatepstvo Naika, Moscow 1971.

[11] Ioffe, A. I. , Naugol'nykh, K. A., and Roi, N. A. , *Zh. Prikl. Mekhan. i Tekh. Fiz.* **1960**, *4*, pp. 108.

[12] Robinson, J. W. *J. Appl. Phys.* **1973**, *44*, pp. 76

[13] R.H. Cole, *Underwater Explosions*, Princeton University Press, 1948

[14] Buntzen, R. R. , The Use of Exploding Wires in the Study of Small-Scale Underwater Explosions in *Exploding Wires, Vol. 2,* Plenum Press, New York, 1962 , pp. 195.

[15] Sehgal, C.; Sutherland, R. G.; and Verall, R.E. , *J. Phys. Chem.* **1980**, *84*, pp. 388.

[16] Pastukhov, V. N. *Sov. Phys. Tech. Phys.* **1968,** *13*, pp. 232.

[17] Krivitskii, E. V. et al. *Sov. Phys. Tech. Phys.* **1972**, *17,* pp. 62.

[18] Krivitskii, E. V. *Sov. Phys. Tech. Phys.* **1973**, *11*, pp. 1839.

[19] Shamko,V.,V. and Krivitskii, E.V.,*Sov. Phys. Tech. Phys.* **1977**, *22*, pp. 52.

[20] Krivitskii,E. V. , Kustovskii, V..D. , and Slivinskii, A. P. *Sov. Phys. Tech. Phys.* **1980**, *25*, pp. 993.

[21] Robinson, J. W. *J. Appl. Phys.* **1973**, *44*, pp. 76.

[22] Lyman Spitzer, Jr., Physics of Fully Ionized Gases, (*Interscience, New York,* 1962) 2nd Ed. pp. 138,139, 143-145

[23] Courant, R. Friedrichs, K. O. *Supersonic Flow and Shock Waves* 1977 New York, Springer-Verlag

3 Numerical Solution of the General Dynamic Equations for the Underwater Plasma Channel

3.1 Introduction

This chapter aims to outline the numerical solution of the equations for the Electrohydraulic Discharge process (*EHD*) [1-11,14] as derived in Chapter 2. The equations to be solved form a set of initial value ordinary non-linear differential equations for which there are standard solvers such as those described in reference [12]. In Section 3.2 we outline the numerical solution, and in Section 3.3 we discuss the initial conditions. Finally, in section 3.4, we compare the results to existing data in the literature. The results are in good agreement with experimental data [2,3] and show that the model does indeed make reliable predictions.

3.2 Formulation of the Equations

The equations 2.16a-d in Chapter 2 can be rearranged to give

$$\frac{dq}{dt} = I(t) \tag{3.1}$$

$$\frac{dI}{dt} = -\frac{\ell}{L_c \sigma_{cond}(t)\pi a^2} I - \frac{q}{L_c C_b}, \tag{3.2}$$

$$\frac{dW}{dt} = \frac{2I^2}{\sigma_{cond}(t)2\pi^2 a^4} - \frac{2(P+W)}{a}\frac{da}{dt} - \frac{2(1-f)}{a}\sigma_B T^4, \tag{3.3}$$

$$\frac{da}{dt} = \left(\frac{\sqrt{7}\alpha^{1/4}}{3\sqrt{\rho_o}}\right)(p+\beta)^{3/7} - \beta^{3/7}, \tag{3.4}$$

$$\frac{dn}{dt} = \frac{2}{a}\left(\frac{f\sigma_B T^4}{\varepsilon_{vaporization}} - n\frac{da}{dt}\right), \tag{3.5}$$

where $\alpha = 3001\ bar$, $\beta = 3000\ bar$ $\rho_o = 1000\ kg/m^3$, $\sigma_B = 5.\ 67051\text{x}10^{-8}\ W/m^2\ {}^oK^4$ and $\varepsilon_{vaporization} = 2.\ 54\text{x}10^{-20}\ joules/particle$.

To allow for the future use of different and more precise mechanisms for the particle induction at the plasma channel boundaries, we define a general induction cross-section $\sigma_{Induction}(T,n)$ using the following conservation of mass relation;

$$\frac{dN}{dt} = nS\sigma_{induction}(T,n), \tag{3.6}$$

where $S = 2\pi a\ell$ is the surface area of the plasma channel. If we compare the above equation with eq 2. 3 in chapter 2, we see that the radiation induction process described in chapter 2, $\sigma_{Induction}(T,n)$ is given by

$$\sigma_{induction}(T,n) = \frac{f\sigma_B T^4}{n\varepsilon_{vaporization}}. \tag{3.7}$$

Substituting for $S = 2\pi a\ell$ and $N = nV = n\pi a^2\ell$ in eq 3.6, we find

$$\frac{dn}{dt} = \frac{2}{a}\left(n\sigma_{induction}(T,n) - n\frac{da}{dt}\right). \tag{3.8}$$

This equation supersedes eq 3.5 with the induction cross-section given by eq 3.7.

Eqs 3.1-3.4 and 3.8 are formulated such that the unknown functions to solve for are *q(t), I(t), W(t), a(t),* and *n(t).* These functions form a vector that we refer to as the internal energy representation;

$$\bar{\mathbf{y}} = \begin{bmatrix} q(t) \\ I(t) \\ W(t) \\ a(t) \\ n(t) \end{bmatrix}. \tag{3.9}$$

Using this representation implies that we need to substitute a functional relation for T in the last term of eq 3.3. Typically, the energy density W for the plasma is given as a function of the temperature *T(t)* and the particle density *n(t)* as follows:

$$W = W(T, n). \tag{3.10}$$

In the case of the energy relation given in Chapter 2 as eq 2. 18b, the function W is readily invertible to become $T = T(W,n)$. Our goal is to formulate the numerical solver code in a form as general as possible, such that other relations can readily be used, as, for example, the relation put forth by Robinson [4]:

$$W(T, n) = c_1 T - \frac{c_2}{c_3}(1 + c_4 T)\exp\left(-c_4 T - \frac{c_3}{n}\right). \tag{3.11}$$

Such a relation in not analytically invertible to obtain a temperature that is a function of W and n. Thus, we favor a representation where the set of unknown functions are given by *q(t), I(t), T(t), a(t),* and *n(t).* Thus, we replace *dW/dt* in eq 3.3 with

$$\frac{dW}{dt} = \left(\frac{\partial W}{\partial T}\right)_n \frac{dT}{dt} + \left(\frac{\partial W}{\partial n}\right)_T \frac{dn}{dt}. \tag{3.12}$$

If we define the functions $W_T(T,n)$ and $W_n(T,n)$ as

$$W_T = \left(\frac{\partial W}{\partial T}\right)_n, \quad W_n = \left(\frac{\partial W}{\partial n}\right)_T \tag{3.13}$$

and we substitute the relations above and 3.12 into eq 3.3 and solve for *dT/dt*, we obtain

$$\frac{dT}{dt} = \frac{2I^2}{W_T \sigma_{cond}(t) 2\pi^2 a^4} - \frac{W_n}{W_T}\frac{dn}{dt} - \frac{2(P+W)}{W_T a}\frac{da}{dt} - \frac{2(1-f)}{W_T a}\sigma_B T^4. \tag{3.14}$$

Finally, we can rewrite equations 3.1, 3.2, 3.4, 3.8 and 3.14 in vector form for input into the numerical equation solver: The final matrix equation is summarized in Figure 3.1. These equations essentially take the form

$$\frac{d\bar{\mathbf{y}}}{dt} = \mathbf{M}(\bar{\mathbf{y}}), \tag{3.15}$$

where the vector $\bar{\mathbf{y}}$ is defined as follows:

$$\bar{\mathbf{y}} = \begin{bmatrix} q(t) \\ I(t) \\ T(t) \\ a(t) \\ n(t) \end{bmatrix} = \begin{bmatrix} y_0 \\ y_1 \\ y_2 \\ y_3 \\ y_4 \end{bmatrix}. \tag{3.16}$$

The equations are non-linear since the right-hand side of the equation cannot be rewritten in the form $\mathbf{M}(\bar{\mathbf{y}}) = \mathbf{M} * \bar{\mathbf{y}}$, but can be readily solved using the standard

$$\frac{d\bar{y}}{dt} = \begin{bmatrix} y_1 \\ -\frac{\ell}{L_c \sigma_{cond}(\bar{y}) \pi {y_3}^2} y_1 - \frac{y_0}{L_c C_b} \\ \frac{2{y_1}^2}{W_T(\bar{y}) \sigma_{cond}(\bar{y}) 2\pi^2 {y_3}^4} - \frac{W_n(\bar{y})}{W_T(\bar{y})} \frac{2}{y_3} \left(y_4 \sigma_{induction}(\bar{y}) - y_4 \left(\left(\frac{\sqrt{7}\alpha^{4/4}}{3\sqrt{\rho_o}} \right) (P(\bar{y}) + \beta)^{4/7} - \beta^{4/7} \right) \right) - \frac{2(P(\bar{y}) + W(\bar{y}))}{W_T(\bar{y}) y_3} \left(\frac{\sqrt{7}\alpha^{4/4}}{3\sqrt{\rho_o}} \right) (P(\bar{y}) + \beta)^{4/7} - \beta^{4/7} - \frac{2(1-f)}{W_T(\bar{y}) y_3} \sigma_B {y_2}^4 \\ \left(\frac{\sqrt{7}\alpha^{4/4}}{3\sqrt{\rho_o}} \right) (P(\bar{y}) + \beta)^{4/7} - \beta^{4/7} \\ \frac{2}{y_3} \left(y_4 \sigma_{induction}(\bar{y}) - y_4 \left(\left(\frac{\sqrt{7}\alpha^{4/4}}{3\sqrt{\rho_o}} \right) (P(\bar{y}) + \beta)^{4/7} - \beta^{4/7} \right) \right) \end{bmatrix}$$

Figure 3.1

Matrix showing the equations for the model of the underwater discharge.

numerical packages from reference [12]. We used both a 4th-order Runge-Kutta approach and an implicit time stepping algorithm based on the Bulirsch-Stoer method [12]. Both approaches give identical and stable results. One can also solve the equations in the internal energy representation defined by eq 3.9 by using the forms given by equations 3.1-3.4, and 3.8. This representation gives identical results to the temperature representation. Verifying that different numerical solvers and different representations give identical results is a practical tool to verify that the chosen algorithm is stable and gives mathematically valid results.

In addition to the application of the matrix shown in Figure 3.1 , we need to define functions for the pressure $P(\overline{\mathbf{y}})$, internal energy $W(\overline{\mathbf{y}})$, electrical conduction $\sigma_{cond}(\overline{\mathbf{y}})$, and particle induction $\sigma_{induction}(\overline{\mathbf{y}})$ as follows:

Pressure
$$P(\overline{\mathbf{y}}) = y_4 k y_2 - \frac{\mu_o y_1^{\,2}}{8\pi^2 y_3^{\,2}} - \frac{e^2}{32\pi^2 \varepsilon_o}\left(\frac{4\pi y_4}{3}\right)^{4/3}. \qquad 3.17a$$

Internal Energy
$$W(\overline{\mathbf{y}}) = \frac{y_4 k y_2}{\gamma - 1}. \qquad 3.17b$$

Conductivity
$$\sigma_{cond}(\overline{\mathbf{y}}) = \xi y_2^{3/2} e^{-5000/T}. \qquad 3.17c$$

Induction Cross-Section
$$\sigma_{induction}(\overline{\mathbf{y}}) = \frac{f\sigma_B y_2^{\,4}}{y_4 \varepsilon_{vaporization}}. \qquad 3.17d$$

Furthermore, the derivatives of the internal energy W_T and W_n, defined in eq 3.13 are given by

$$W_T(\overline{\mathbf{y}}) = \frac{y_4 k}{\gamma - 1} \qquad 3.18a$$

and

$$W_n(\overline{y}) = \frac{ky_2}{\gamma - 1}. \qquad 3.18b$$

The numerical solution routines are given in Mathcad format in Appendix E.

3.3 Initial Conditions

To completely specify the numerical solution, we need to determine appropriate initial conditions for the functions *q(t), I(t), T(t), a(t),* and *n(t).* We will denote these initial conditions by q_o=*q(0),* I_o=*I(0),* T_o=*T(0),* a_o=*a(0),* and n_o=*n(0).* Not all of these initial conditions are independent from one another and from the parameters of the discharge such as the initial voltage U_o, the capacitance C_b, and the gap length ℓ. qo is determined by the initial voltage U_o determines the first of our initial conditions:

$$q_o = C_b U_o \qquad 3.19$$

where,

$$U_o = (R(0) + R_c)I_o \ , \qquad 3.20$$

$$R(0) = \frac{\ell}{\sigma_{cond}(0)\pi a^2} \ , \qquad 3.21$$

and

$$\sigma_{cond}(0) = \xi T_o^{3/2} e^{-5000/T_o}. \qquad 3.22$$

In addition, the initial conditions must also satisfy the equation of state:

$$P_o = n_o k T_o \qquad 3.23$$

for which we have neglected the Pinch and Coulomb effect since initially, the current and particle densities are too low for these effects to be significant.

Eqs 3.19 through 3.23 show that in addition to the initial voltage U_o, only three other parameters are necessary to fully specify the initial conditions. We choose as our initial condition parameters the initial resistance $R_o=R(0)$, the initial radius a_o, and the initial pressure $p_o=P(0)$ of the plasma channel. Based on the initial voltage and these parameters, the components of the initial vector:

$$\bar{\mathbf{y}}(0) = \begin{bmatrix} q_o \\ I_o \\ T_o \\ a_o \\ n_o \end{bmatrix} = \begin{bmatrix} y^o{}_0 \\ y^o{}_1 \\ y^o{}_2 \\ y^o{}_3 \\ y^o{}_4 \end{bmatrix}, \qquad 3.24$$

where the individual components are given by

$$y_0^o = C_b U_o, \qquad 3.25a$$

$$y_1^0 = \frac{U_o}{(R_c + R_o)}, \qquad 3.25b$$

solve for $y^o{}_2$ out of $$\xi\left(y_2^o\right)^{3/2} e^{-5000/y_2^o} = \frac{\ell}{\pi\left(y_3^o\right)^2 R_o}, \qquad 3.25c$$

$$y_3^o = a_o, \qquad 3.25d$$

$$y_4^o = \frac{p_o}{k y_2^o}. \qquad 3.25e$$

eqs 3.25a-e give the initial conditions that must be used in order to start the numerical iteration. Since there is no closed analytical solution for the temperature in eq 3.25c, we must solve it numerically prior to launching the simulation. The most appropriate initial conditions are chosen to be a_o= 0. 5-1 mm, R_o=1 Ω -10 $k\Omega$, and p_o=1 - 100 *bar*. We found that over the ranges indicated, the model showed little sensitivity to changes in the initial conditions. The resistance R_0 was always chosen such that the initial temperature found from solving eq 3.25c was in between 3000 to 10,000 K. The simulation is designed to start modeling the dynamics after the plasma channel is already established, yet before any major plasma expansion takes place.

3.4 Comparison with Data

Although our simulation uses results that have been previously validated experimentally [1,2,4,13], it is still useful to verify the reliability of our model by comparing our simulations to existing published data. This section demonstrates how our simulation accurately reproduces both the dynamics of measured plasma channel parameters, and the general variations in temperature as a function of the various discharge parameters.

Martin presents data [2] for a gap length of ℓ = 1. 5 *cm*gap and a discharge energy of 1. 8 kJ. Figure 3.2 shows good agreement between experimental results and our simulation. The simulation uses the same experimental parameters as those given in Martin's work [2], namely a capacitance C_B = 5. 8 μF, an initial voltage ofU_o = 25 kV, an inductance ofL_c = 260 nH, and an equivalent circuit resistance ofR_c = 42. 2 $m\Omega$. The medium is determined by the constant ξ, which we have chosen such that the simulated current matches the measured current. The best value is 14. 11x$10^{-3}K^{-3/2}\Omega^{-1}m^{-1}$. The fraction f is chosen to give the best fit for the observed temperature (e.g., f = 0. 2). A value of f = 0. 2 implies that as much as 20% of the outgoing electromagnetic radiation contributed to particle induction.

Using eq 2. 14 and solving for n provides a way of deducing the particle density as a function of time using experimental data for the internal energy W:

$$n = \frac{W(\gamma - 1)}{KT}. \qquad 3.26$$

For the same discharge illustrated in Figure 3.2, we can compare the particle density n derived from experimental data and eq 3.26, and the results of our simulation. As Figure 3.3 illustrates, the agreement is good.

Although the predicted current, channel radius, and particle density dynamics agree with the experimental results, at first glance, it appears that the predicted pressure does not agree with the experiment, as is illustrated by Figure 3.4. In addition, the fact that the pressure is at its peak initially and gradually drops with increasing time as assumed by Martin [2] contradicts other findings. [3,5-7] This discrepancy between

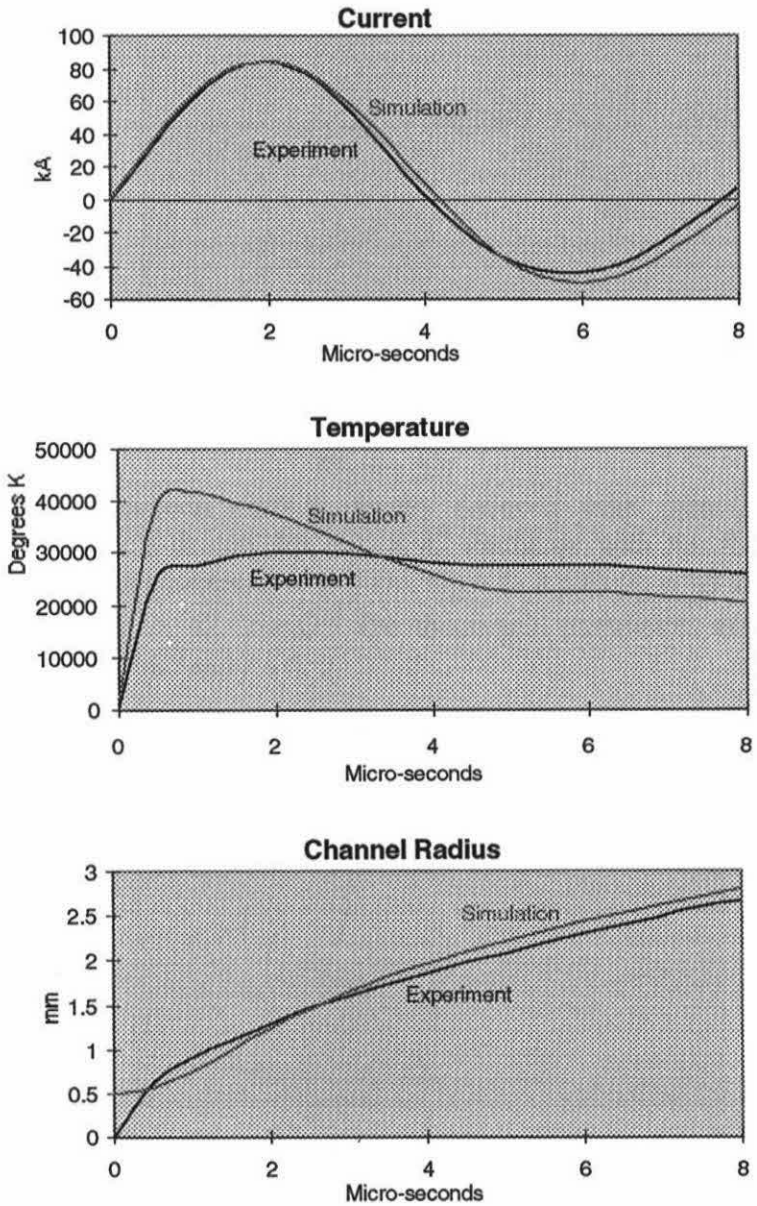

Figure 3.2

Comparison between data [2] and simulated plasma channel dynamics for a 1. 8 *kJ* discharge with the following experimental parameters: ℓ = 1. 5 *cm*, C_B = 5. 8 μF, U_0 = 25 *kV*, L_c = 260 *nH*, and R_c = 42. 2 $m\Omega$. The theoretical parameters are ξ=14. 11x$10^{-3} K^{-3/2} \Omega^{-1} m^{-1}$ and f = 0. 2.

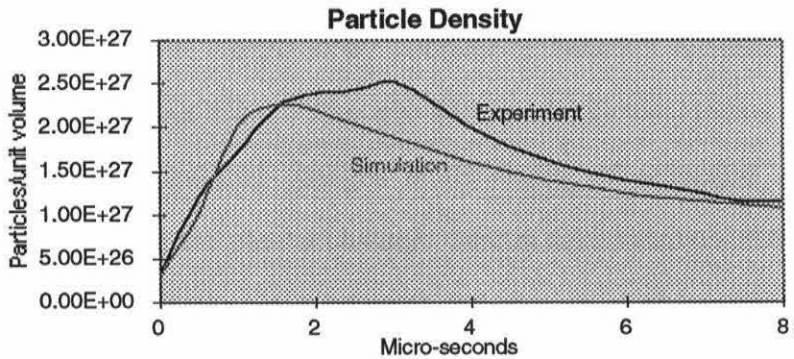

Figure 3.3

Comparison between particle density deduced from data [2] and simulated particle density for a 1. 8 *kJ* discharge with the following experimental parameters: ℓ = 1. 5 *cm*, C_B = 5. 8 μF, U_o = 25 *kV*, L_c = 260 *nH*, and R_c = 42. 2 $m\Omega$. The theoretical parameters are ξ=14. $11\text{x}10^{-3} K^{-3/2} \Omega^{-1} m^{-1}$ and f = 0. 2.

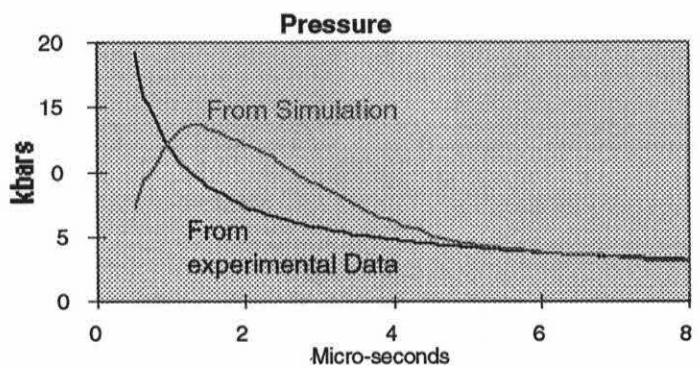

Figure 3.4

Comparison between pressure deduced from plasma channel measurements [2] which do not take into account magnifications due to density induced changes in index of refraction, and simulated particle density for a 1. 8 *kJ* discharge with the following experimental parameters: ℓ = 1. 5 *cm*, C_B = 5. 8 μF, U_o = 25 *kV*, L_c = 260 *nH*, and R_c=42. 2 $m\Omega$. The theoretical parameters are $\xi = 14.11\text{x}10^{-3} K^{-3/2} W^{-1} m^{-1}$ and f = 0. 2.

the pressure time history published by Martin and by others [3,5-7], and that predicted by our simulation can be explained by considering Martin's measurements of the plasma channel radius. He did not take into account the channel radius magnification resulting from density induced changes in the index of refraction of the water immediately surrounding the plasma channel. Martin acknowledges this problem and argues that this magnification is greatest during the initial phase of the discharge. However, he did not measure the pressure directly, but deduced it from the plasma channel radius using eq 2. 4. If the magnification in the plasma channel radius is taken into account and the pressure is recalculated, the results come into good agreement with our simulation, as is illustrated in Figure 3.5.

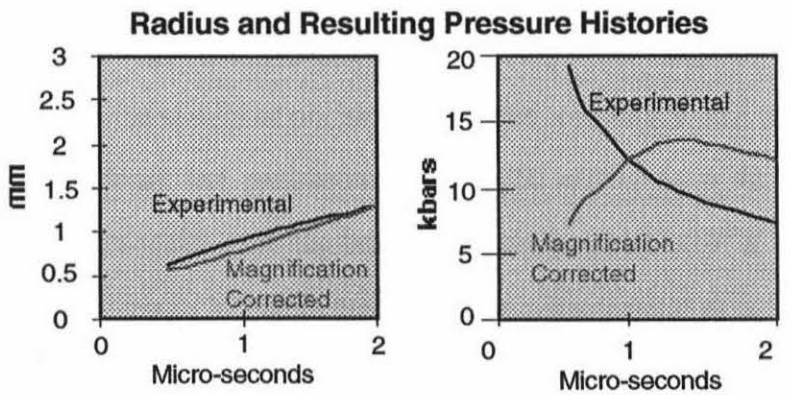

Figure 3.5

Illustration of the effect of small changes in channel radius on pressure . The data [2] which does not take into account magnification effects due to density changes near the plasma channel produces an unusually high pressure initially. A reasonable pressure history which is in good agreement with the simulation output can be obtained by correcting the channel radius to take into account the magnification effects. The data is from a 1. 8 kJ discharge with the following experimental parameters: ℓ = 1. 5 cm, C_B = 5. 8 μF, U_o = 25 kV, L_c = 260 nH, and R_c=42. 2 $m\Omega$. The theoretical parameters are $\xi = 14.11 \times 10^{-3} K^{-3/2} W^{-1} m^{-1}$ and f = 0. 2.

Figure 3.5 shows how a small reduction in the plasma channel radius history brings the resulting pressure into closer agreement with the simulated pressure data as shown in Figure 3.4. Such a reduction takes into account optical magnification effects

These results show that our simulation predicts plasma channel dynamics in agreement with experiment and that the plasma channel dynamics appear to follow the equations of our model. To further verify that our simulation is indeed successful, we must check that our model also reliably reproduces observed changes associated with varying the parameters of the discharge, such as gap length.

Robinson [3] measured both the temperature and the channel radius for $C_B = 15$ μF, $U_o = 15$ kV discharges with channel lengths varying in the range $\ell = 1.\ 27 - 5$ cm. Figure 3.6 compares the results of our simulation with Robinson's data for the various gap lengths. The circuit had parameters of$L_c = 250$ $nH$and $R_c = 42.\ 2$ $m\Omega$. The theoretical parameters which gave the best results are $\xi = 14.11\text{x}10^{-3} K^{-3/2} W^{-1} m^{-1}$ and $f = 0.\ 2$. The upper graph in Figure 3.6 shows the experimental data and the lower graph shows the corresponding simulation results. The simulation predicts an overall temperature decrease of the plasma channel as the gap length increases. This result agrees with the experimental data presented by Robinson [3].

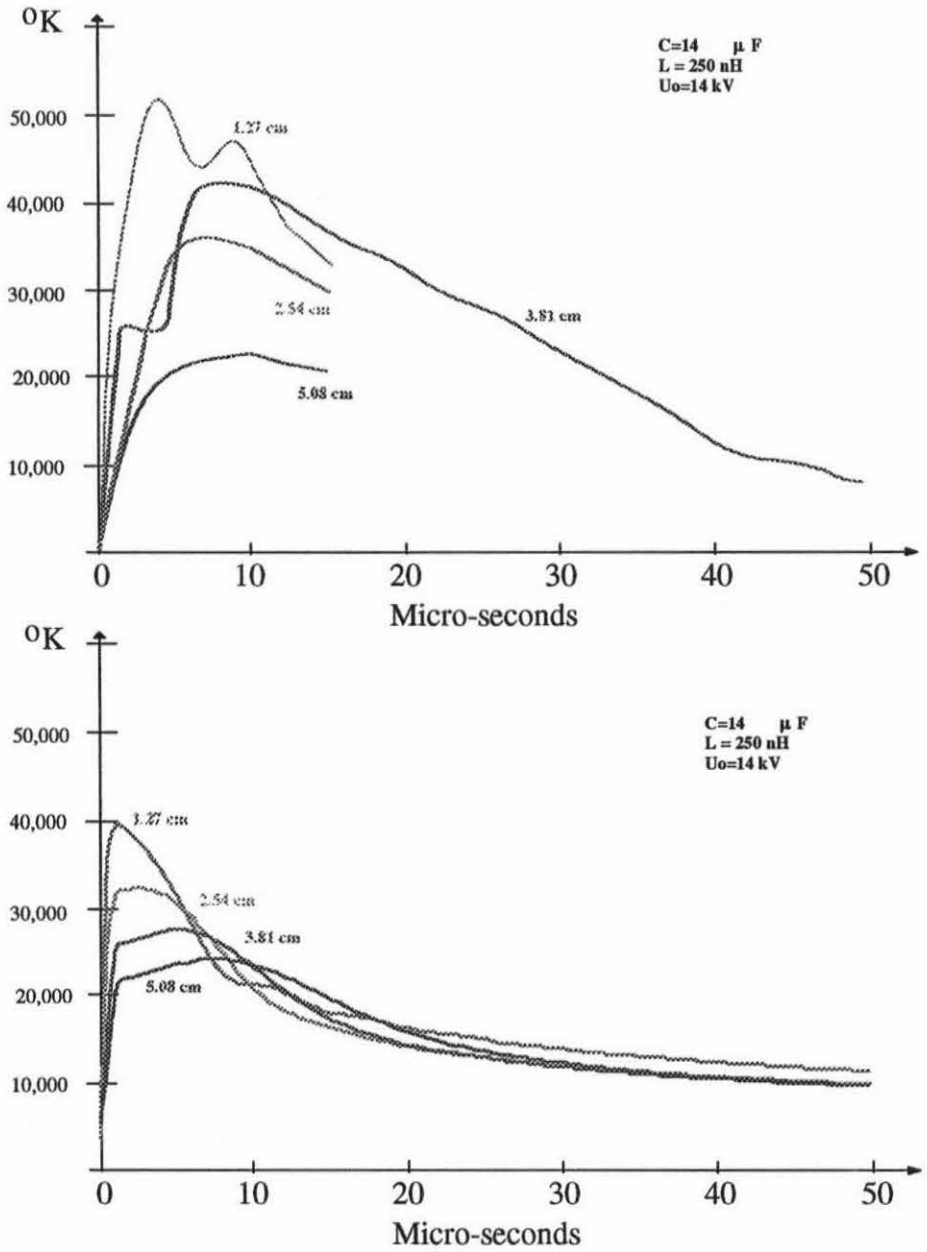

Figure 3.6

Comparison in between simulated and measured [3] temperature dynamics for a 1. 7 *kJ* discharge with the following experimental parameters: ℓ = 1. 27 - 5 *cm*, C_B = 15 μF, U_o = 15 *kV*, L_c = 250 *nH*, and R_c=42. 2 $m\Omega$. The theoretical parameters are $\xi = 14.11 \times 10^{-3} K^{-3/2} W^{-1} m^{-1}$ and f = 0. 2. The graph above shows the experimental data, and the one below shows the corresponding simulation results. The simulation predicts that the temperature of the plasma channel is overall higher for shorter gap lengths. This result agrees with the data.

3.5 Conclusions and Discussion

The simulation presented in this chapter makes predictions for both the plasma channel dynamics and the overall temperature trend as a function of gap length which are in good agreement with experiment. The simulation can thus be used reliably to make predictions on how the input energy is partitioned into the various physical processes. The simulation code is written in such a way as to allow manipulation of the constitutive equations of the plasma itself. The code can thus be used in the future for other experiments in order to explore and verify new constitutive equations for cool, dense high pressure plasmas. Such experiments could be helpful to further understand the nature of the underwater plasma channel. The use of a Spitzer-like conductivity relationship and an ideal gas law with corrective terms for the Pinch effect and the Coulombic interactions give results with better precision than is necessary for the high-repetition discharge experiments designed to measure the chemical effects of the EHD process.

References

[1] Ioffe, A. I.;Naugol'nykh, K. A.; and Roi, N. A. *Zh. Prikl. Mekhan. i Tekh. Fiz.* **1964**, *4*, pp. 108.

[2] Martin, E. A., *J. App. Phys.* **1960**, *31*, pp. 255-265.

[3] Robinson, J. W. *J. Appl. Phys.* **1973**, *44*, pp. 72.

[4] Robinson, J. W. *J. Appl. Phys.* **1973**, *44*, pp. 76.

[5] Krivitskii, E. V. et al. *Sov. Phys. Tech. Phys.* **1978,** *23*, pp. 564.

[6] Krivitskii, E. V. ; Kustovskii, V. D. ;and Slivinskii, A.P. *Sov. Phys. Tech. Phys.* **1980**, *25*, pp. 993.

[7] Tsurkin, V. N. and Shvets, I. S. , *High Temp. USSR* **1987**, *25*, pp. 160.

[8] Pastukhov,V. N. *Sov. Phys. Tech. Phys.* **1968**, *13*, pp. 232.

[9] E.V. Krivitskii et al. *Sov. Phys. Tech. Phys.* **1972**, *17*, pp. 62.

[10] Krivitskii, E.V. *Sov. Phys. Tech. Phys.* **1973**, *17*, pp. 1839.

[11] Shamko, V. V. and Krivitskii, E. V., *Sov. Phys. Tech. Phys.* **1977**, *22*, pp. 52.

[12] Press, W. H. et al. *Numerical Recipes in C : The Art of Scientific Computing* 2nd ed. New York, Cambridge University Press, 1992.

[13] Lyman Spitzer, Jr., *Physics of Fully Ionized Gases*, (*Interscience, New York,* 1962) 2nd Ed

[14] Robinson, J. W. *J. Appl. Phys.* **1967**, *38*, pp. 210

4 Analytic Solution of the General Dynamic Equations for the Initial Stage of an Underwater Plasma Channel

4.1 Introduction

The primary aim of this chapter is to present an analytical solution to the equations necessary to simulate the underwater plasma channel that is present during an electrohydraulic Discharge Process (*EHD*) event [1-12]. The analytical solution is valid only for the initial stage of the discharge during which the power rise can be approximated to be linear [1]. Some basic properties of the plasma channel such as its maximum pressure and temperature can be deduced from a simple solution without extensive numerical computations. The assumptions are the same as described in Chapters 2 and 3, namely, we assume a two-phase system with a discontinuity at the channel boundary [3]. The equations to be solved are given by

$$L_c \frac{dI}{dt} + [R_c + R]I + \frac{q}{C_b} = 0, \qquad \frac{dq}{dt} = I, \tag{4.1}$$

$$RI^2 = \frac{d}{dt}(WV) + P\frac{dV}{dt} + (1-f)\sigma_B T^4 S, \tag{4.2}$$

$$\frac{da}{dt} = \left(\frac{\sqrt{7}\alpha^{1/4}}{3\sqrt{\rho_o}}\right)(P+\beta)^{1/7} - \beta^{1/7}, \tag{4.3}$$

$$\frac{dN}{dt} = \frac{fS\sigma_B T^4}{\varepsilon_{vaporization}}, \tag{4.4}$$

where $\alpha = 3001$ *bar*, $\beta = 3000$ *bar* $\rho_o = 1000$ *kg/m*^{3}, $\sigma_B = 5.67051 \times 10^{-8}$ *W/m*^{2} $^oK^4$ and $\varepsilon_{vaporization} = 2.54 \times 10^{-20}$ *joules/particle*.

The assumption of a linear power rise of the form

$$RI^2 = Q_o t \tag{4.5}$$

eliminates the need for eq 4.1. The parameter Q_o can be deduced from simple experimental measurements of the current and voltage. The power RI^2 must be calculated experimentally using eq 4.6;

$$RI^2 = U_d(t)I(t), \tag{4.6}$$

where $U_d(t)$ is the voltage across the underwater gap, as shown in Figure 4.1, and is not to be confused with the voltage across the capacitor bank. If $U(t)$ and $I(t)$ represent respectively the measured voltage and current across the capacitor bank, then the power RI^2 is given by

$$RI^2 = \left(U(t) - R_c I(t) - L_c \frac{dI}{dt} \right) I. \tag{4.7}$$

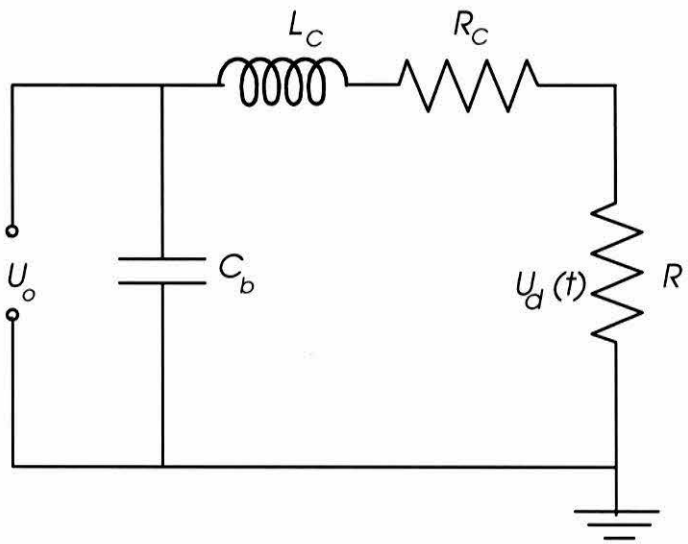

Figure 4.1

Equivalent circuit for the discharge analysis. R represents the discharge channel resistance, L_c and R_c represents the equivalent circuit inductance and resistance, respectively. C_b is the capacitance of the storage bank, and U_o is the initial charging voltage. $U_d(t)$ is the voltage across the underwater gap.

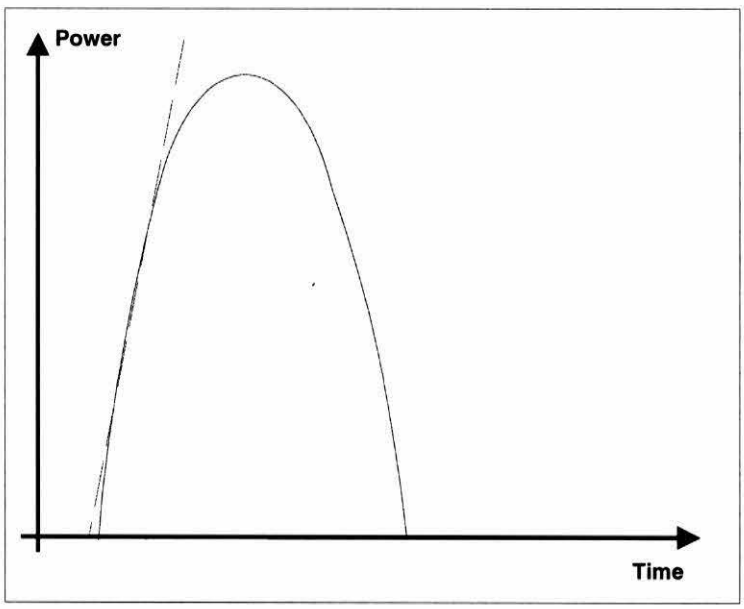

Figure 4.2

Typical power curve for the first quarter cycle. The initial power rise can usually be approximated as a linear function, as illustrated by the dashed line.

The power curve generally will take the shape shown in Figure 4.2. For the initial stage of the discharge, the assumption of a linear power rise as illustrated by eq 4.5 is reasonable [1]. In this case, an analytical solution for equations 4.2, 4.3 and 4.4 can be obtained by using the following trial functions for the plasma channel temperature, radius and particle number density:

$$\begin{aligned} a(t) &= \Theta t \\ N(t) &= N_o t^2 \\ T(t) &= T_o . \end{aligned} \tag{4.8}$$

The particle density is given by

$$n = \frac{N}{V}. \tag{4.9}$$

Using $V = \pi a^2 \ell$ and eq 4.8 implies that the particle density is constant and is given by

$$n = \frac{N_o}{\pi \Theta^2 \ell}. \tag{4.10}$$

Using the ideal gas law $P = nkT$, we find that the pressure is constant and is given by

$$P_o = \frac{N_o k T_o}{\pi \Theta^2 \ell} \tag{4.11}$$

in which the Coulomb effect has been neglected. With the Coulomb effect, the pressure is still constant, since the corrective term is only a function of the particle density, which is constant. However, the algebraic equations become considerably more complicated to solve, and the accuracy added by the Coulomb effect is

superfluous, since we have already made the approximation that the power rise is linear.

Substituting relations 4.8 into eqs 4.2, 4.3 and 4.4 yield three more algebraic equations, which, along with eq 4.11 form a set of four equations for the four unknowns N_O, T_O, Θ, and P_O.

$$\frac{\gamma}{\gamma - 1} P_o \Theta^2 + (1 - f)\sigma_B \Theta - \frac{Q_o}{2\pi\ell} = 0, \tag{4.12}$$

$$\frac{f\sigma_B T_o^4}{\varepsilon_{vapor}} = n_o \Theta, \tag{4.13}$$

$$(P_o + \beta)^{1/7} = \left(\frac{3\sqrt{\rho_o}}{\sqrt{7}\alpha^{1/4}}\right)\Theta + \beta^{1/7}. \tag{4.14}$$

eqs 4.11, 4.12 and 4.13 can be rearranged to yield the pressure, particle density, and the channel radius velocity as a function of temperature:

$$\Theta = \frac{Q_o}{2\pi\ell}\left[\frac{\gamma}{\gamma - 1}\frac{kf\sigma_B T_o^5}{\varepsilon_{vapor}} + (1 - f)\sigma_B T_o^4\right]^{-1}, \tag{4.15}$$

$$P_o = \frac{2\pi\ell kf\sigma_B T_o^5}{\varepsilon_{vapor} Q_o}\left[\frac{\gamma}{\gamma - 1}\frac{kf\sigma_B T_o^5}{\varepsilon_{vapor}} + (1 - f)\sigma_B T_o^4\right], \tag{4.16}$$

$$n_o = \frac{2\pi\ell f\sigma_B T_o^4}{\varepsilon_{vapor} Q_o}\left[\frac{\gamma}{\gamma - 1}\frac{kf\sigma_B T_o^5}{\varepsilon_{vapor}} + (1 - f)\sigma_B T_o^4\right]. \tag{4.17}$$

Finally, an equation for T_o can be obtained by substituting equations 4.15 and 4.16 into eq 4.14;

$$\left[\frac{2\pi\ell kf^2\sigma_B T_o^5}{\varepsilon_{vapor}Q_o}\left[\frac{\gamma}{\gamma-1}\frac{kf\sigma_B T_o^5}{\varepsilon_{vapor}}+(1-f)\sigma_B T_o^4\right]+\beta\right]^{7/7} - \frac{3Q_o\sqrt{\rho_o}}{2\pi\ell\sqrt{7}\alpha^{1/4}}\left[\frac{\gamma}{\gamma-1}\frac{kf\sigma_B T_o^5}{\varepsilon_{vapor}}+(1-f)\sigma_B T_o^4\right]^{-1} - \beta^{7/7} = 0 \qquad 4.18$$

There is no closed analytical solution of eq 4.18, although for T_o; however, it can be solved numerically. The numerical result for T_o can then be substituted into eqs 4.15, 4.16, and 4.17 to obtain the values for the channel velocity, the pressure, and the particle density for the plasma channel.

This solution can be used for quick first order approximations of the plasma channel characteristics using experimental data. If we take for example the experimental values for Q_o for an ℓ = 1. 5 *cm* gap 1. 8 *kJ* discharge as measured by Martin [2], where Q_o = 1. 9x10^8 *MW/sec*, we find that using f = 0. 2, the channel characteristics are T_o = 40,000 *K*, P_o = 13 *kbars*, n_0 = 2. 4x10^{27} *particles/m*^{3}, and Θ_o = 500 *m/sec*. The actual temperature measured by Martin was 30,000 *K*, so our estimate is about 10,000 *K* too high. On the other hand, using data from reference [5] for an ℓ = 1. 5 *cm* gap 2. 16 *kJ* discharge with Q_o = 3x10^{12} *W/s*, we can use eq 4.15 to estimate the radial velocity of the plasma channel Θ. Assuming f = 10%, We find Θ = 207 *m/s*, which is a good result compared to the experimental value of 200 *m/s*. In a similar fashion, we can make one more prediction for data found in reference [3] for an ℓ = 7 *cm* gap 2. 7 *kJ* discharge with Q_o = 1. 3x10^{12} *W/s*. Assuming f = 10%, We find Θ = 143 *m/s*, compared to an experimental value of 140 *m/s*.

4.2 Thermal Particle Induction

The fact that the temperature predicted for Martin's data using eq 4.18 is higher than that in the data implies that eq 4.4 underestimates the magnitude of particle induction. As the particle density increases, the energy transferred into the plasma channel is distributed over a greater number of particles, thereby reducing the temperature of the plasma channel.

Eq 4.4 assumes that the primary mechanism for particle induction is through the vaporization of particles as they absorb some of the radiation emitted by the plasma channel. It is conceivable that particles may also be inducted into the plasma channel as a result of direct thermal collisions with the plasma particles. In this section, we derive a cross-section for a purely thermal particle induction mechanism, and we use this result in a calculation which leads to similar results as shown in the previous section for the radiation induction mechanism.

The calculation of the thermal induction cross-section is based on reference [4]. In this calculation, we assume that particles are inducted into the plasma channel only as a result of thermal collisions between plasma particles and water molecules at the channel walls. Therefore, the radiation effects are ignored here, and to simplify the calculation, three-particle recombination effects will also be neglected. For particle species i, the rate at which particles are inducted into the channel is given by

$$\frac{dN_i}{dt} = \chi \frac{\frac{d\varepsilon_i}{dt}}{\varepsilon_{formation}}, \qquad 4.19$$

where $\frac{d\varepsilon_i}{dt}$ is the rate at which energy is transferred to the wall of the plasma channel as a result of collisions in between the i^{th} plasma species and the wall, and $\varepsilon_{formation}$ is the energy of formation of the gas. The proportionality constant parameter χ is 1/24; [4]. As a result of collisions, the energy transferred to the wall of the plasma channel is given by

$$\frac{d\varepsilon_i}{dt} = z_i S \Delta\varepsilon_i, \tag{4.20}$$

where z_i is the number of collisions per unit area for the plasma species i, S is the surface area of the plasma channel, and $\Delta\varepsilon_i$ is the amount of energy transferred per collision. From the kinetic theory of an ideal gas, we know that for an ideal gas of volume V with a total of N particles with an average kinetic velocity u, z is given by

$$z_i = \frac{1}{4}\frac{N_i}{V}u_i. \tag{4.21}$$

Substituting the above result into eq 4.20 and using $S = 2\pi a\ell$ and $V = \pi a 2\ell$ yields

$$\frac{d\varepsilon_i}{dt} = \frac{1}{4}\frac{N_i}{\pi a^2 \ell}u_i 2\pi a\ell\Delta\varepsilon_i = \frac{N_i u_i \Delta\varepsilon_i}{2a}. \tag{4.22}$$

The energy transferred per collisions is given as

$$\Delta\varepsilon_i = \frac{8 m_{H_2O} m_i}{3\left(m_{H_2O} + m_i\right)^2}\frac{3}{2}kT, \tag{4.23}$$

where we assume a collision in between a water molecule and a plasma species of mass m_i at temperature T. The water molecule is assumed to have zero thermal momentum compared to the plasma particle.

The mean thermal velocity of each individual plasma particle of species i is given by

$$u_i = 2\sqrt{\frac{2kT}{\pi m_i}}. \tag{4.24}$$

Now, we substitute equations 4.22, 4.23 and 4.24 into eq 4.19, which yields

$$\frac{dN_i}{dt} = \frac{\chi}{\varepsilon_{formation}} \frac{N_i u_i \Delta\varepsilon_i}{2a} = 4\sqrt{\frac{2}{\pi}} \frac{\chi m_{H_2O} (kT)^{3/2}}{\varepsilon_{formation} a} \frac{N_i \sqrt{m_i}}{\left(m_{H_2O} + m_i\right)^2}. \tag{4.25}$$

Then, summing over all the components i, we now have

$$\frac{dN}{dt} = \sum_{i=0}^{species} \frac{dN_i}{dt} = 4\sqrt{\frac{2}{\pi}} \frac{\chi m_{H_2O} (kT)^{3/2} N}{\varepsilon_{formation} a} \sum_{i=0}^{species} \frac{N_i/N \sqrt{m_i}}{\left(m_{H_2O} + m_i\right)^2}. \tag{4.26}$$

We define $\nu_i = \frac{N_i}{N}$ so that eq 4.26 becomes

$$\frac{dN}{dt} = 4\sqrt{\frac{2}{\pi}} \frac{\chi m_{H_2O} (kT)^{3/2} N}{\varepsilon_{formation} a} \sum_{i=0}^{species} \frac{\nu_i \sqrt{m_i}}{\left(m_{H_2O} + m_i\right)^2}. \tag{4.27}$$

This equation can be rewritten in the form

$$\frac{dN}{dt} = N \frac{1}{a} \left(4\sqrt{\frac{2}{\pi}} \frac{\chi m_{H_2O} k^{3/2}}{\varepsilon_{formation}} \sum_{i=0}^{species} \frac{\nu_i \sqrt{m_i}}{\left(m_{H_2O} + m_i\right)^2} \right) T^{3/2}. \tag{4.28}$$

With the surface area given by $S = 2\pi a\ell$ and the volume given by $V = \pi a^2 \ell$, we can write

$$\frac{1}{a} = \frac{1}{2}\frac{2\pi a\ell}{\pi a^2 \ell} = \frac{1}{2}\frac{S}{V} \tag{4.29}$$

such that eq 4.28 becomes

$$\frac{dN}{dt} = \frac{N}{V} S \frac{1}{2}\left(4\sqrt{\frac{2}{\pi}} \frac{\chi m_{H_2O} k^{3/2}}{\varepsilon_{formation}} \sum_{i=0}^{species} \frac{\nu_i \sqrt{m_i}}{\left(m_{H_2O} + m_i\right)^2} \right) T^{3/2}. \tag{4.30}$$

We then define the induction cross-section $\sigma_{ionize}(T)$ as

$$\sigma_{ionize}(T) = \left(2\sqrt{\frac{2}{\pi}} \frac{\chi m_{H_2O} k^{3/2}}{\varepsilon_{formation}} \sum_{i=0}^{species} \frac{\nu_i \sqrt{m_i}}{\left(m_{H_2O} + m_i\right)^2} \right) T^{3/2} = \kappa T^{3/2}, \tag{4.31}$$

where

$$\kappa = 2\sqrt{\frac{2}{\pi}} \frac{\chi m_{H_2O} k^{3/2}}{\varepsilon_{formation}} \sum_{i=0}^{species} \frac{\nu_i \sqrt{m_i}}{\left(m_{H_2O} + m_i\right)^2} \tag{4.32}$$

such that the equation for the conservation of mass takes the form

$$\frac{dN}{dt} = nS\sigma_{ionize}(T), \tag{4.33}$$

where n is the particle density, and $\sigma_{ionize}(T)$ and K are defined in eq 4.31 and 4.32, respectively. To evaluate the constant κ, we need to establish the values of the various constants in eq 4.32.

First, we evaluate each $\nu_i = \frac{N_i}{N}$. (*Vide supra*) Let β_i be equal to the number of species *i* per molecule, and let *M* represent the total number of molecules dissociated to form a plasma of *N* molecules. Then, for each species i,

$$N_j = \beta_j M \tag{4.34}$$

so that

$$\nu_i = \beta_i \frac{M}{N}. \tag{4.35}$$

But N is just the sum over the number of species present in the plasma:

$$N = \sum_{j=0}^{species} N_j \tag{4.36}$$

which, in terms of 4.34 yields

$$N = M \sum_{j=0}^{species} \beta_j . \tag{4.37}$$

Substituting the expression 4.37 for N into 4.35 finally gives

$$\nu_i = \frac{\beta_i}{\sum_{j=0}^{species} \beta_j}. \tag{4.38}$$

Using $\varepsilon_{formation}$ = 1. 29x10^{-20} *Joules*, $m_{hydrogen}$ = 6. 3x10^{-27} *kg*, m_{oxygen} = 1x10^{-25} kg, m_{H2O} = 1. 124x10^{-25} *kg*, we find that

$$\kappa = 2\sqrt{\frac{2}{\pi}}\frac{\chi m_{H_2O} k^{1/2}}{\varepsilon_{formation}}\sum_{i=0}^{species}\frac{\nu_i\sqrt{m_i}}{\left(m_{H_2O}+m_i\right)^2} = 1.81x10^{-4}. \qquad 4.39$$

This new particle induction mechanism can be used in place of eq 4.4 to yield a new solution to the linear power rise problem defined by eq 4.5. If we take the same trial solution given by eq 4.8, and we substitute it into our new particle induction equation given by

$$\frac{dN}{dt} = nS\kappa T^{1/2} \qquad 4.40$$

we then arrive at

$$\Theta = \kappa T^{1/2} \qquad 4.41$$

which, along with equations 4.12 and 4.14, forms a set of three equations for three unknowns. Combining eq 4.41 and 4.14 gives

$$p_o = \left[\left(\frac{3\sqrt{\rho_o}}{\sqrt{7}\alpha^{1/4}}\right)\kappa T_o^{1/2} + \beta^{1/7}\right]^{7/3} - \beta \qquad 4.42$$

substituting 4.42 into 4.12, we get an equation for the temperature T_o;

$$\frac{\gamma}{\gamma-1}\left[\left[\left(\frac{3\sqrt{\rho_o}}{\sqrt{7}\alpha^{1/4}}\right)\kappa T_o^{1/2} + \beta^{1/7}\right]^{7/3} - \beta\right](\kappa T_o^{1/2})^2 + (1-f)\sigma_B T_o^4(\kappa T_o^{1/2}) - \frac{Q_o}{2\pi\ell} = 0. \qquad 4.43$$

If we take the same experimental values of Q_o for an ℓ = 1. 5 *cm* gap 1. 8 *kJ* discharge as measured by Martin [2] where Q_o = 1. 9x10^8 *MW/sec*, we find that by using f=0, we obtain a temperature of only T_o = 20,000 *K*, and a particle density which is larger by a factor of 2 at n_o = 2. 4x10^{27} *particles/*m^3, while the other parameters, P_o = 13 *kbars*, and Θ_0=500 *m/sec*, are the same. The parameter f is set to zero since radiation absorption is neglected in this calculation. The value of f does not affect the result in any significant way. Even if we set f = 0. 5, we obtain a temperature change of only several hundred degrees *K*.

4.3 Discussion

The fact that the actual temperature of 30,000 *K* measured by Martin [2] is in between the two temperatures previously estimated suggests that the thermal particle induction is not as significant as is implied by our calculations, and equivalently, the radiative induction process is most likely to be accompanied by some degree of thermal induction. The extra amount of particle induction beyond just radiative processes can easily be accounted for by adjusting the value of f in our calculations to a value greater than the actual percentage of radiation below 185 *nm*, the radiation absorption cut-off for water with dissolved O2. If we use eq 4.18 with a value of f = 0. 5, the resulting temperature becomes 30,000 *K*, in good agreement with Martin's [2] measurements. For a 30,000 K blackbody spectrum, the fraction of radiation emitted below 200 *nm* is around 15%, The extra 35% in our choice of f can be interpreted as representing thermal induction processes.

The analytical solution discussed in this chapter serves as a good first approximation to gain physical insight into the underlying processes which govern the dynamics of the underwater discharge. This simple analytical solution cannot be used for predicting the parameters prior to performing the discharge, but gives a good estimate of the parameters once the experimental parameter Q_o is known.

References

[1] Roi, N. A. and Frolov, D. P. *DAN SSSR* **1958**, *118*, pp. 683.

[2] Martin, E. A. *J. App. Phys.* **1960**, *31*, 255-265.

[3] Ioffe, A. I.; Naugol'nykh, K. A; and Roi, N. A.*Zh. Prikl. Mekhan. i Tekh. Fiz.* **1964**, *4*, pp. 108.

[4] Arsentev, V. V. *Zhurnal Prikladnoi Mekhaniki i Tekhnicheskoi Fiziki* **1965** *5* 51-57.

[5] Skvortsov, Y.; Komelkov, V.; Kuznetov, N. M; Komel'kov, V. S.*Zhurnal Tekhnicheskoi Fiziki* **1960** *30* 1165-1177.

[6] Ioffe, A. I.; Naugol'nykh, K. A; and Roi, N. A.*Zh. Prikl. Mekhan. i Tekh. Fiz.* **1964** , *4*, pp. 108.

[7] Pastukhov, V. N. *Sov. Phys. Tech. Phys.* **1968**, *13*, pp. 232.

[8] Krivitskii, E. V. et al. *Sov. Phys. Tech. Phys.* **1972**, *17*, pp. 62.

[9] Krivitskii, E. V. et al. *Sov. Phys. Tech. Phys.* **1973**, *17*, pp. 1839.

[10] Shamko, V. V. and Krivitskii, E. V. *Sov. Phys. Tech. Phys.* **1977**, *22*, pp. 52.

[11] Krivitskii, E. V.; Kustovskii, V. D.; and Slivinskii, A. P. *Sov. Phys. Tech. Phys.* **1980**, *25*, pp. 993.

[12] Tsurkin,V. N. and Shvets, I. S. *High Temp. USSR* **1987**, *25*, pp. 160.

5 Prediction of the Energy Partition

5.1 Introduction

The underwater discharge [1-12] provides four distinct effects which have the potential to degrade organic contaminants: UV radiation [13], a shock wave [14], an intense plasma channel [15,16], an a super-critical water steam bubble [17]. Each of these effects induce distinctively different chemical effects. Depending on which compound is to be degraded, it may be preferable to maximize the shock wave, and minimize the radiation, or vice-versa. Hence a critical aspect of our research is to learn how to control the efficiency of each of these effects.

The primary purpose of the equations of Chapter 3 and their solutions as described in both chapters 4 and 5 is to predict radiation and shock wave energy efficiencies for various parameters of the discharge. Although our pulsed power system is equipped with a 135 μF capacitor bank, individual capacitors can be removed to vary the capacitance from 15 to 135 μF in 15 μF intervals. The voltage can be varied from 0 to 25 kV to control the total energy of the discharge. The spark gap length can also be adjusted by modifying the gap between the electrodes in the reactor chamber. A full description of the experimental apparatus is given in Chapter 6.

5.2 Calculating the Efficiency

The energy partitioning as illustrated in Figure 5.1 [18] can be readily calculated using the numerical solutions described in chapter 3. The energy transferred into the shock waves is given by

$$E_{shockwave} = \int p dv \qquad 5.1$$

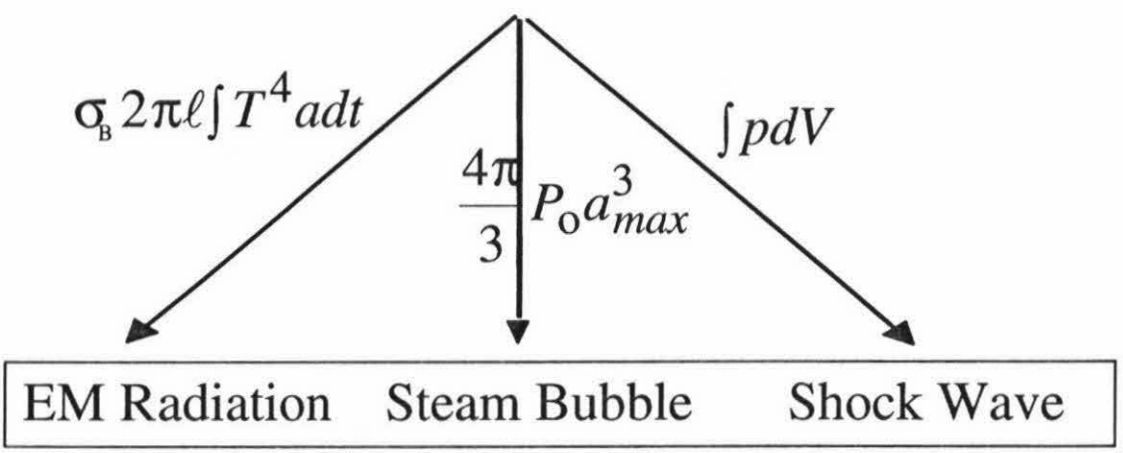

Figure 5.1
Energy distribution at time of initial steam bubble formation [18]. The energy transferred into the plasma channel is dissipated via electromagnetic radiation and shock waves. The remaining energy will then contribute to the formation of a post-discharge steam bubble.

and the energy dissipated by radiation is given by

$$E_{Radiation} = (1 - f)\int \sigma_B T(t)^4 dt. \qquad 5.2$$

The energy not dissipated by means of shock waves or radiation contributes to a post-discharge water steam bubble whose maximum radius can be estimated using the following relation:

$$E_{capacitor} - E_{shock} - E_{Radiation} = \frac{4}{3}\pi p_o a_{\max}^3, \qquad 5.3$$

where E_{total} is the total energy in the capacitor bank, which is given by

$$E_{capacitor} = \frac{1}{2} C U_o^2. \qquad 5.4$$

However, eq 5.3 ignores the fact that not all of the energy in the capacitor will be transferred to the underwater plasma. Since any discharge circuit will typically have some circuit resistance R_c as illustrated in Figure 5.2, a significant fraction of the energy in the capacitor bank may be dissipated by that resistance.

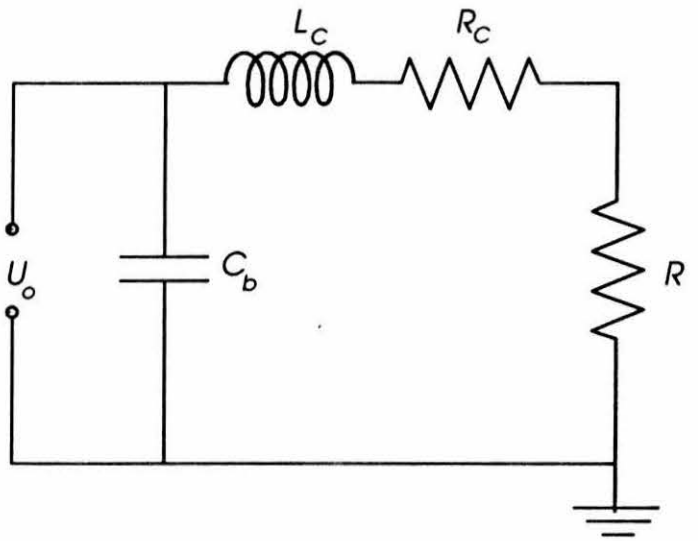

Figure 5.2
Equivalent circuit for the discharge analysis. R represents the discharge channel resistance, L_c and R_c represents the equivalent circuit inductance and resistance, respectively. C_b is the capacitance of the storage bank, and U_o is the initial charging voltage. The capacitance and inductance of the plasma channel are negligible.

Eq 5.3 should then be replaced by

$$E_{disch\,arg\,e} - E_{shock} - E_{Radiation} = \frac{4}{3}\pi p_o a_{\max}^3, \qquad 5.5$$

where $E_{discharge}$ is the energy transferred to the underwater plasma, as given by

$$E_{disch\,arg\,e} = \int R(t)I(t)^2 dt. \qquad 5.6$$

In order to factor out circuit dependent effects, we calculate the shock wave and radiation efficiencies by comparing E_{shock} and $E_{radiation}$ to $E_{discharge}$ rather than $E_{capacitor}$. At the same time, the overall discharge efficiency is obtained by comparing $E_{discharge}$ as described by eq 5.6 to $E_{capacitor}$ as described by eq 5.4.

We define the following efficiency parameters. The total efficiency η_{total} is given by

$$\eta_{total} = \frac{E_{disch\,arg\,e}}{E_{total}} 100 = \frac{10^2 \int R(t)I(t)^2 dt}{\frac{1}{2} CU_o^{\,2}}. \qquad 5.7$$

The shock wave efficiency η_{shock} is given by

$$\eta_{shock} = \frac{E_{shock}}{E_{disch\,arg\,e}} 100 = \frac{10^2 \int pdv}{\int R(t)I(t)^2 dt} \qquad 5.8$$

and the radiation efficiency $\eta_{radiation}$ is given by

$$\eta_{radiation} = \frac{E_{Radiation}}{E_{discharge}} 100 = \frac{(1-f)10^2 \int \sigma_B T(t)^4 dt}{\int R(t) I(t)^2 dt}, \qquad 5.9$$

where all of the above efficiency parameters are given as percentages. Since the resistance of the discharge varies as a function of the various parameters of the discharge, such as the capacitance, inductance, gap length and initial voltage, the total efficiency η_{total} will also vary as a function of the parameters. Eqs 5.7 through 5.9 are used in all of the calculations of the following section.

5.3 Results

The results of our calculations are summarized in Figures 5.3 through 5.12. In all calculations, unless indicated otherwise, the following parameters were used: C_b = *135* μF, U_o = *5 kV*, L_c = *250 nH*, ℓ =*0. 8 cm*, and R_c = *13* $m\Omega$. We differentiate in between control parameters and design parameters; the control parameters are values that can be changed during the course of an experiment, such as the gap length and the initial voltage. The design parameters, unlike the control parameters, typically require some circuit modification. The inductance and the capacitance generally fall under this category, since the changes in pulse length resulting from varying these parameters require other changes in the electronic circuitry to accommodate for the overall impedance and timing changes.

Figures 5.3 and 5.4 show the total energy efficiency as a function of the design and control parameters, respectively. The total energy transferred decreases for increasing initial voltage, inductance or capacitance, while it increases for increasing gap length. The most significant decrease takes place with increasing capacitance. The shock wave efficiency is illustrated in Figures 5.5 and 5.6. The only significant decreases in

shock wave efficiency take place with increasing inductance and gap length. While capacitance also decreases this efficiency, the decrease is less than 5 %, and is thus comparatively insignificant. Changes in initial voltage do not affect the shock wave efficiency at all.

The radiation efficiency is illustrated in Figures 5.7 and 5.8. Changes in all of the parameters leave the radiation efficiency relatively unchanged. A change in spark gap length from 0. 8 to 5 cm only increases the overall radiation efficiency by 2 % from 11 to 13 %. Increases in initial voltage and capacitance decrease this efficiency by 2%. Changes in inductance leave the radiation efficiency completely unchanged. Figures 5.9 through 5.12 show the magnitudes of the maximum temperature and pressure. These extremes usually occur during the first quarter cycle of the discharge. The dependencies are the same for temperature and pressure; both increase with increasing energy via both capacitance and inductance, and both decrease with increasing gap length and inductance.

However, we note that changes in initial voltage bring about the largest changes in both maximum pressure and temperature. Changes in capacitance bring about only very little change in maximum pressure. Maximum temperature is reached with the smallest capacitance and gap length. The maximum pressure decreases significantly with increasing gap length.

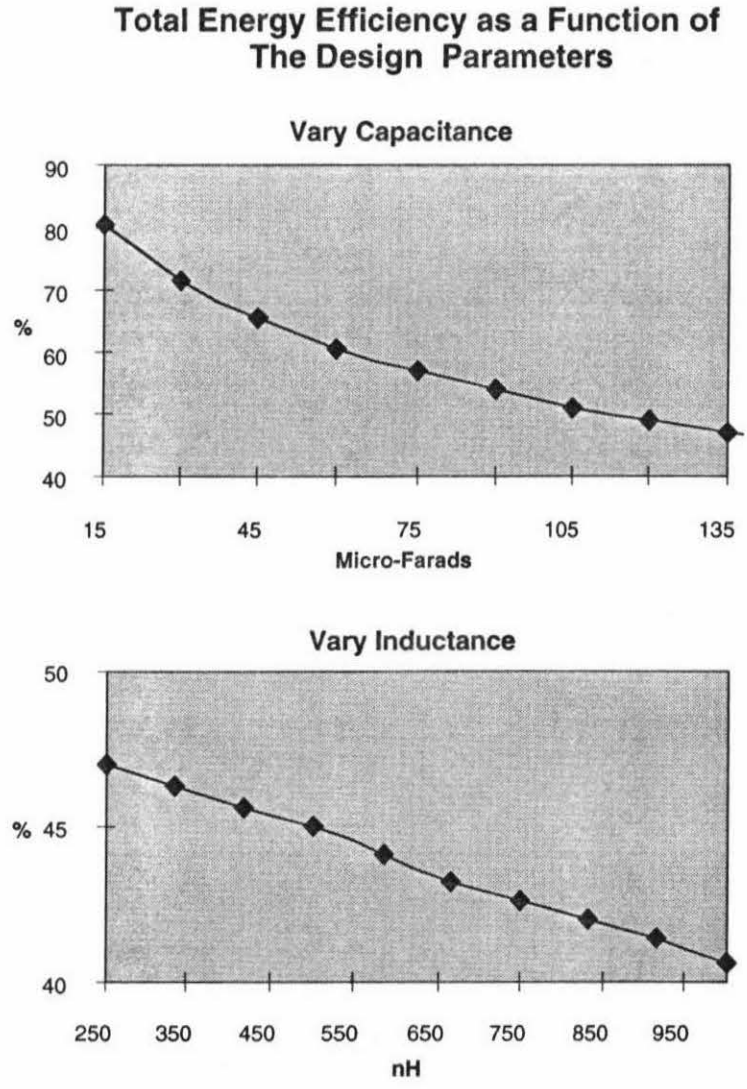

Figure 5.3

Total energy efficiency in percents as a function of capacitance and inductance as calculated using eq 5.7. The simulation assumes a circuit resistance R_c = 13 $m\Omega$, a gap length ℓ = 0. 8 cm, and an initial voltage U_o = 5 kV.

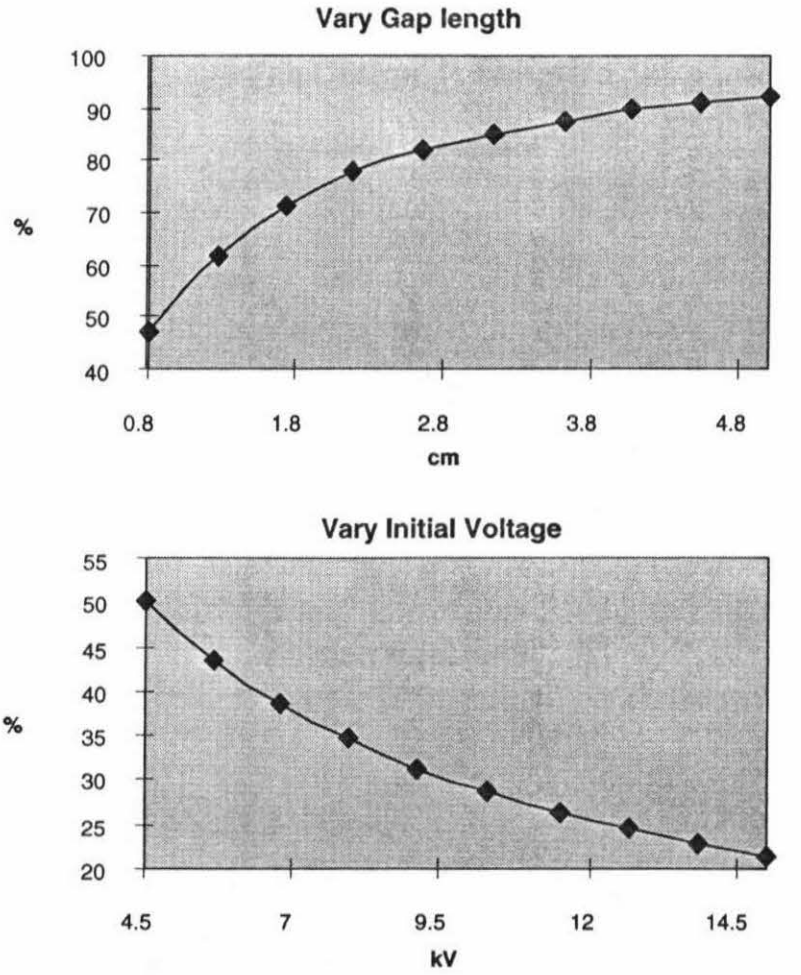

Figure 5.4

Total energy efficiency in percents as a function of gap length and initial voltage as calculated using eq 5.7. The simulation assumes a circuit resistance 13 $m\Omega$, an inductance L_c = 250 nH, and a capacitance C_b = 135 μF.

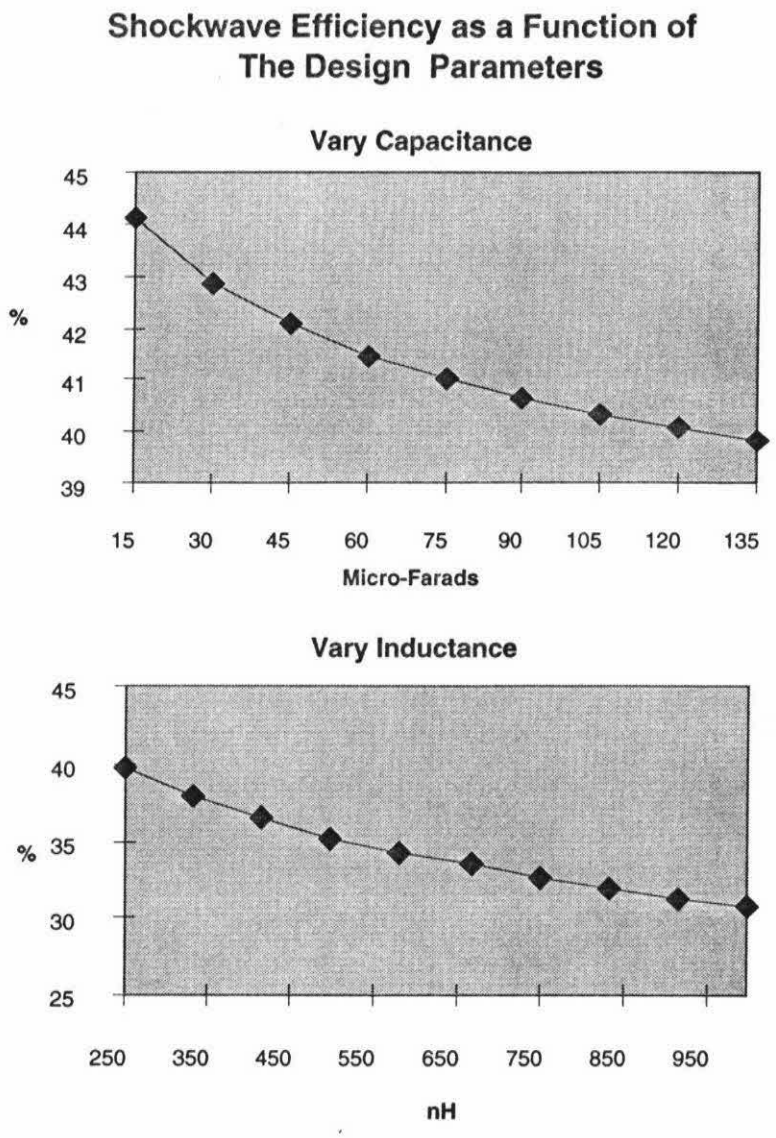

Figure 5.5

Shock wave efficiency in percents as a function of capacitance and inductance calculated using eq 5.8. The simulation assumes a circuit resistance R_c = 13 $m\Omega$, a gap length ℓ = 0. 8 cm, and an initial voltage U_o = 5 kV.

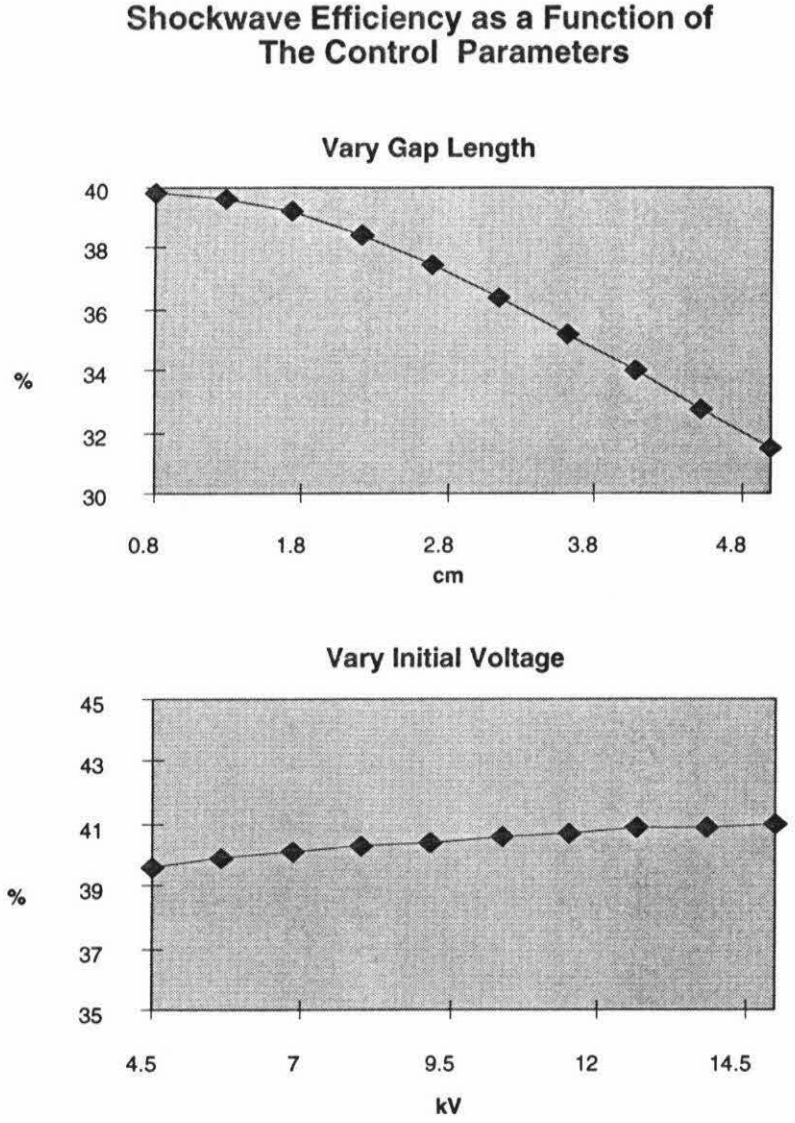

Figure 5.6

Shock wave efficiency in percents as a function of gap length and initial voltage calculated using eq 5.8. The simulation assumes a circuit resistance 13 $m\Omega$, an inductance L_c = 250 nH, and a capacitance C_b = 135 μF.

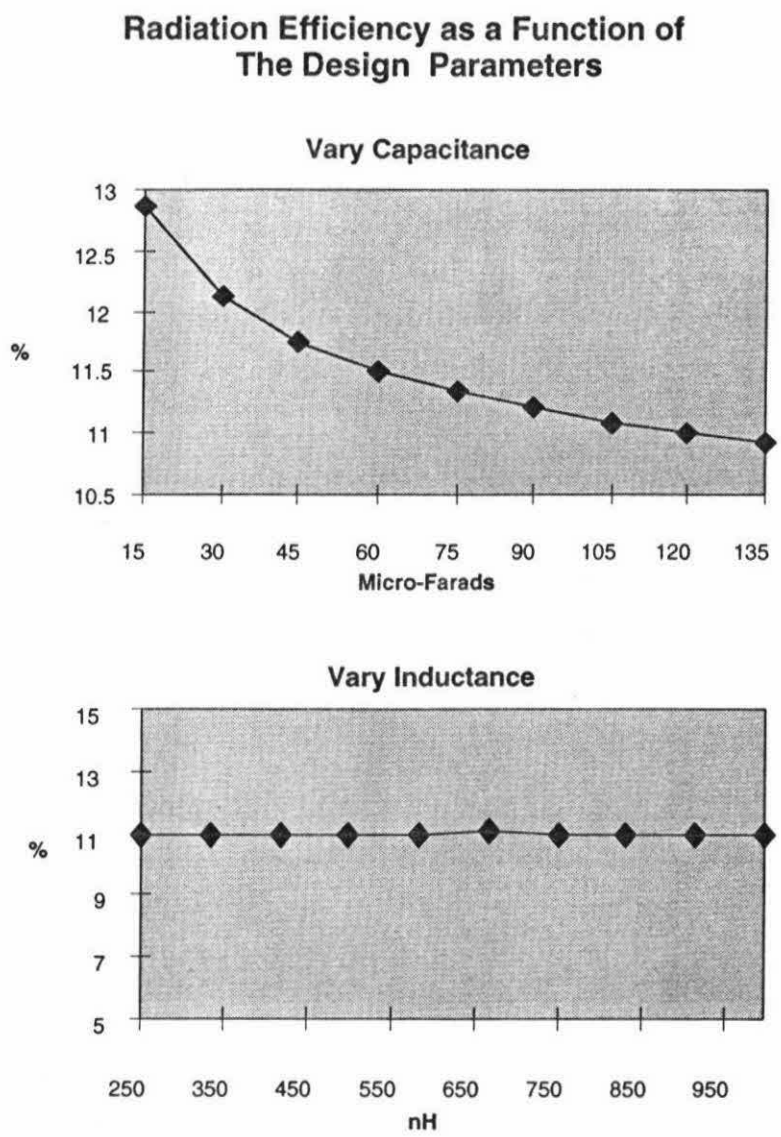

Figure 5.7

Radiation efficiency in percents as a function of capacitance and inductance calculated using eq 5.9. The simulation assumes a circuit resistance $R_c = 13\ m\Omega$, a gap length $\ell = 0.\ 8\ cm$, and an initial voltage $U_o = 5\ kV$.

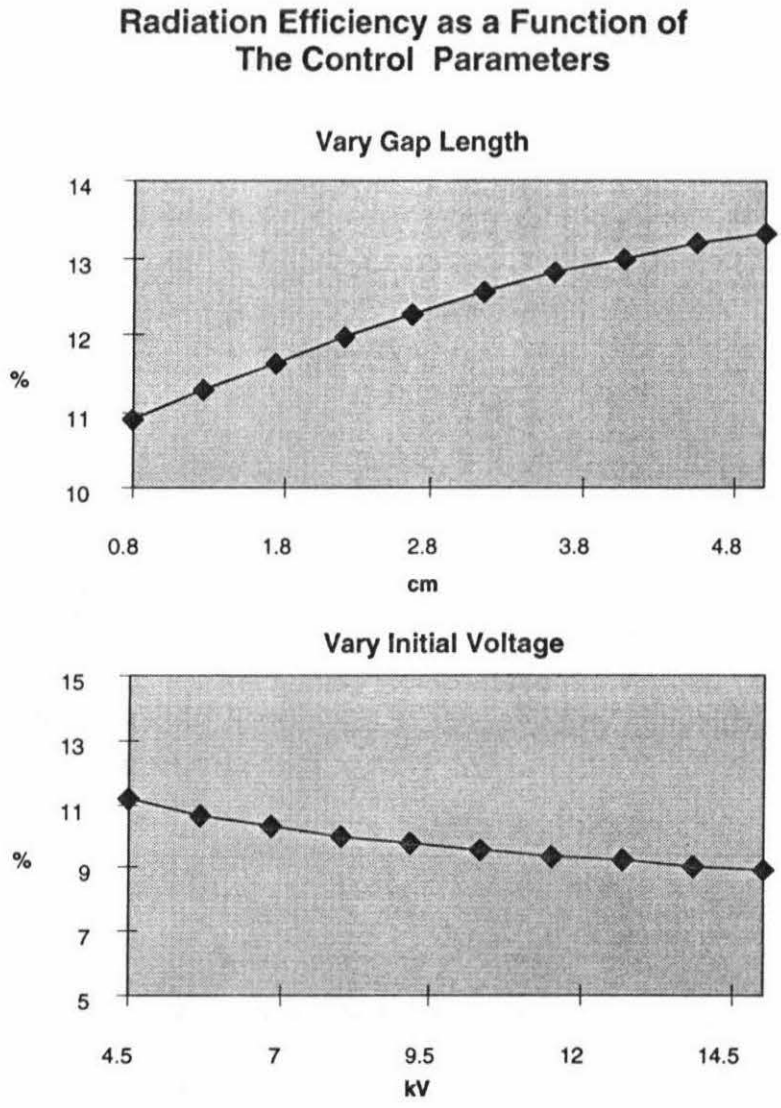

Figure 5.8

Radiation efficiency in percents as a function of gap length and initial voltage calculated using eq 5.9. The simulation assumes a circuit resistance 13 $m\Omega$, an inductance $L_c = 250\ nH$, and a capacitance $C_b =$ 135 μF.

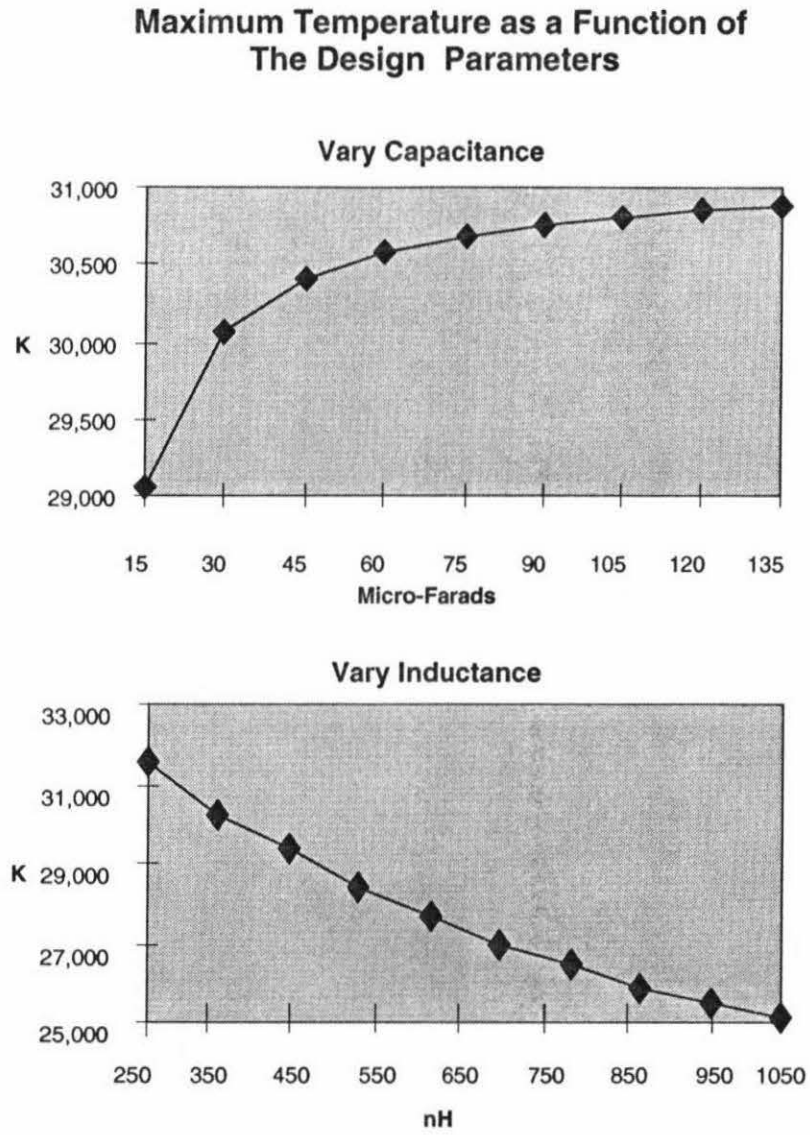

Figure 5.9

Maximum temperature in degrees Kelvin as a function of capacitance and inductance. The maximum usually occurs within the first quarter cycle. The simulation assumes a circuit resistance R_c = 13 $m\Omega$, a gap length ℓ = 0. 8 cm, and an initial voltage U_o = 5 kV.

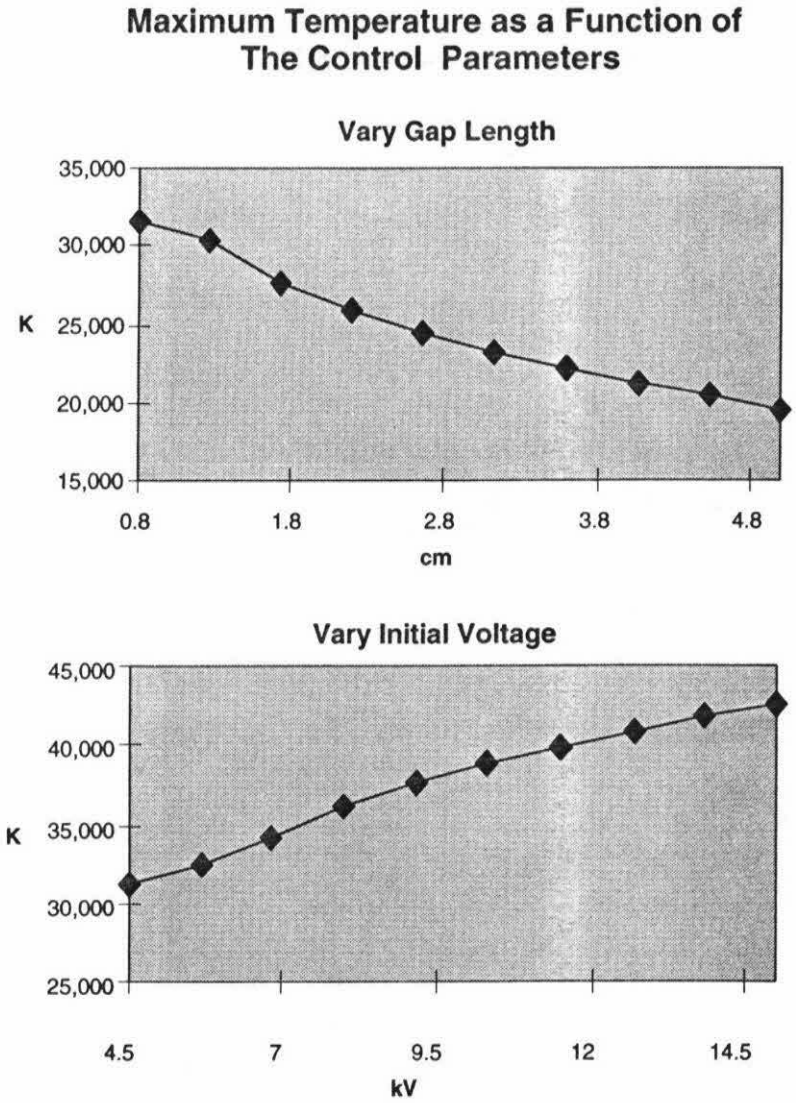

Figure 5.10

Maximum temperature in degrees Kelvin as a function of gap length and initial voltage. the maximum usually occurs within the first quarter cycle. The simulation assumes a circuit resistance 13 $m\Omega$, an inductance $L_c = 250\ nH$, and a capacitance $C_b = 135\ \mu F$.

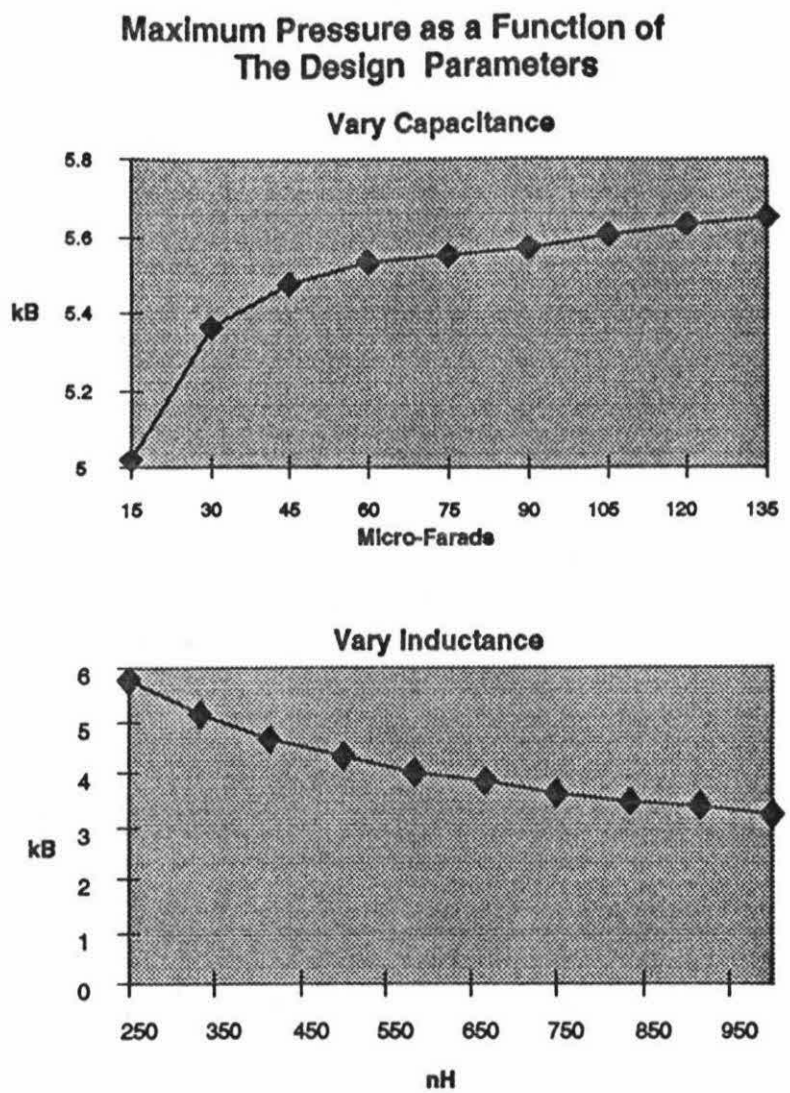

Figure 5.11

Maximum pressure in *kilobars* (10^3 *ATM*) as a function of capacitance and inductance. The maximum usually occurs within the first quarter cycle. The simulation assumes a circuit resistance R_c = 13 $m\Omega$, a gap length ℓ = 0. 8 *cm*, and an initial voltage U_o = 5 *kV*.

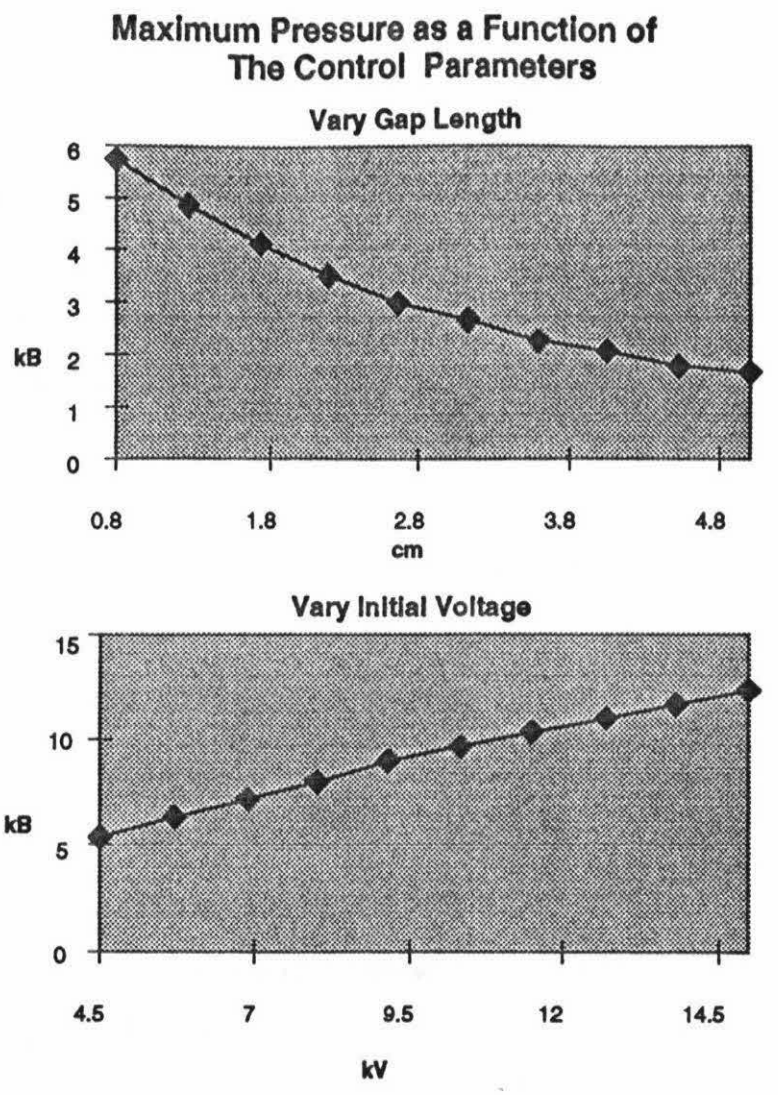

Figure 5.12

Maximum pressure in *kilobars* (10^3 *ATM*) as a function of gap length and initial voltage. the maximum usually occurs within the first quarter cycle. The simulation assumes a circuit resistance 13 $m\Omega$, an inductance $L_c = 250\ nH$, and a capacitance $C_b = 135\ \mu F$.

5.4 Discussion

In Chapter 3, we showed that the simulations match reasonably well with experimental data. For the purpose of predicting changes in the energy partitioning as a function of parameters, the model is also in agreement with data. As verified experimentally by Robinson [3], the temperature of the plasma channel does indeed decrease as a function of increasing gap length

The increase in total energy efficiency as a function of increased gap length as illustrated in Figures 5.3 and 5.4 can be easily explained by the fact that the resistance of the plasma channel is directly proportional to the gap length,

$$R = \frac{\ell}{\sigma_{cond}(t)\pi a^2} \qquad 5.10$$

and, thus increases as the gap widens, allowing a larger fraction of the energy to dissipate into the underwater plasma.

The decrease in total efficiency as the initial voltage increases can be attributed to the higher temperature reached, which, in turn, increases the conductivity

$$\sigma_{cond} = \xi T^{3/2} e^{-5000/T} \qquad 5.11$$

and, consequently decreases the resistance as illustrated by eq 5.10. The temperature increase with increasing capacitance is insufficient to account for the dramatic decrease in efficiency. But, we notice that as the capacitance increases, the average

radius of the plasma channel increases as well. As shown by eq 5.11, a larger channel radius a leads to a lower resistance, and hence decreases the total efficiency.

Even though increases in initial voltages cause both the maximum temperature and pressure to increase dramatically, we see no significant effects on the energy partitioning, Changes in the energy partition are obtained by changing the inductance and the gap length. While the gap length affects both the shock wave and the radiation efficiency, the inductance affects only the shock wave efficiency. A simple explanation is that the inductance slows down the energy transfer enough to affect the rate at which the channel radius expands. The radiation efficiency is unaffected because even though the overall temperature drops, the time over which the radiation is emitted increases.

The increases in radiation efficiency with increasing gap length can be explained by an increase in the overall plasma channel surface area, and a reduction of the discharge ringing which increases the time width of the temperature peak. Both of these effects compensate for the reduction in overall temperature, leading to a slight increase in the radiation efficiency.

As will be shown in Chapter 6, shock waves alone do not lead to significant chemical degradation, hence we do not need to take into account the shock wave efficiency. In determining which combination of parameters is best for increasing chemical efficiency, it is thus only necessary to consider both the radiation efficiency and the maximum temperature of the plasma channel. Thus, for example, even though the overall energy partitioning remains unaffected by changes in initial voltages, photochemical processes would still change as a result of the changes in temperature of the plasma channel.

The most interesting control parameter is the capacitance, since increases in capacitance lead to very small increases in both shock wave and radiation efficiencies, while the maximum temperature and pressure remain nearly constant. This would suggest that a device with a smaller capacitance would lead to very similar chemical effects. The advantage of a smaller capacitance is a faster charging time, and a decrease in net energy consumed. Hence, the total chemical oxidation process energy efficiency should be maximized by lowering the capacitance of the LRC circuit.

References

[1] Martin, E.A. *J. App. Phys* . **1960**, *31*, 255-265.

[2] Robinson, J. W. *J. Appl. Phys.* **1967**, *38*, pp. 210.

[3] Robinson, J. W.; Ham, M.; Balaster, A. N. *J. App. Phys* . **1973**, *44*, pp. 72.

[4] Robinson, J. W. *J. Appl. Phys.* **1973**, *44*, pp. 76.

[5] Naugolnykh, K. A.; Roy, N. A. *Electrical Discharges in Water. A Hydrodynamic Description.* technical report FTD-HC-2049-74, Foreign Technology Division, Wright-Patterson Air Force Base, Ohio. 1974.

[6] Ioffe,A. I.; Naugol'nykh, K. A.; and Roi, N. A. *Zh. Prikl. Mekhan. i Tekh. Fiz.* **1964.**, *44*, pp.108.

[7] Pastukhov, V. N. *Sov. Phys. Tech. Phys.* **1968**, *13* , pp. 232.

[8] Krivitskii, E. V. et al. *Sov. Phys. Tech. Phys.* **1972**, *17*, pp. 62.

[9] E. V. Krivitskii, *Sov. Phys. Tech. Phys.* **1973**, *17*, pp. 1839.

[10] Shamko,V. V.; Krivitskii, E. V., *Sov. Phys. Tech. Phys.* **1977**, *22*, pp. 52.

[11] Krivitskii, E. V.; Kustovskii,V. D.; and Slivinskii, A. P. *Sov. Phys. Tech. Phys.* **1980**, *25*, pp. 993.

[12] Tsurkin, V. N.; Shvets, I. S. *High Temp. USSR* **1987**, *25*, pp. 160.

[13] Legrini, O.; Oliveros, E.; Braun, A. M. *Chem. Rev.* **1993**, *93*, pp. 671.

[14] Hoffman, M. R.; Hua, I.; Hoechemer, R.; Willberg, D. M.; Lang, P. S.; and Kratel, A. W. H. *Chemistry under Extreme Conditions* In: Chemistry Under Extreme or Non-Classical Conditions, Ed. by R. Van Eldik and C. D. Hubbards.

[15] Penetrante, B. M.; Schultheis, S. E.; *Non-Thermal Plasma Techniques for Pollution Control Part A: Overview, Fundamentals and Supporting Technology*; Eds. Springer-Verlag: New York, 1993.

[16] *Non-Thermal Plasma Techniques for Pollution Control Part B: Electron Beam and Electrical Discharge Processing*; Penetrante, B. M.; Schultheis, S. E.; Eds. Springer-Verlag: New York, 1993.

[17] Franck, E.U. et al. Supercritical Water: A Medium for Chemistry *Engineering and Science News*, December 23, 1991.

[18] Buntzen, R. R. The Use of Exploding Wires in the Study of Small-Scale Underwater Explosions. *Exploding Wires, Vol 2;* Chace, W. G.; Moore, H. K. Eds. Plenum Press: New York, NY, 1962; pp. 195.

6 Degradation of 4 -Chlorophenol, 3,4 Dichloroaniline, and 2,4,6 Trinitrotoluene in an Electrohydraulic Discharge Reactor

6.1 Introduction

An *EHD* system consists of two major components: a pulsed-power electrical discharge circuit and a reaction chamber. Electrical energy is stored in a large capacitance (135 μF) pulsed-power circuit and is then released as a pulsed electrical discharge using fast ignitron switches. Each pulse can have energies ranging from 2 to 25 kJ with a duration of 20-100 μs and peak powers in the megawatt to gigawatt range. The reactor vessel shown on the left-hand side of Figure 6.1 contains an electrode assembly and the aqueous solution to be treated. The reactor is designed to withstand the high electrical currents and voltages, and the intense shockwaves generated by the electrohydraulic discharges.

Basic pulsed-power technology has been incorporated into other *AOTs* such as in non-thermal plasma and corona discharge treatment of hazardous wastes [2,3]. However, they depend on substantially different chemical mechanisms than the *EHD* process to achieve compound destruction. Non-thermal plasma technology has been applied primarily to gas phase waste streams. This approach relies on high-energy collisions of molecules with electrons to generate free radicals and lower-energy electrons, which subsequently react with the chemical contaminants. The corona

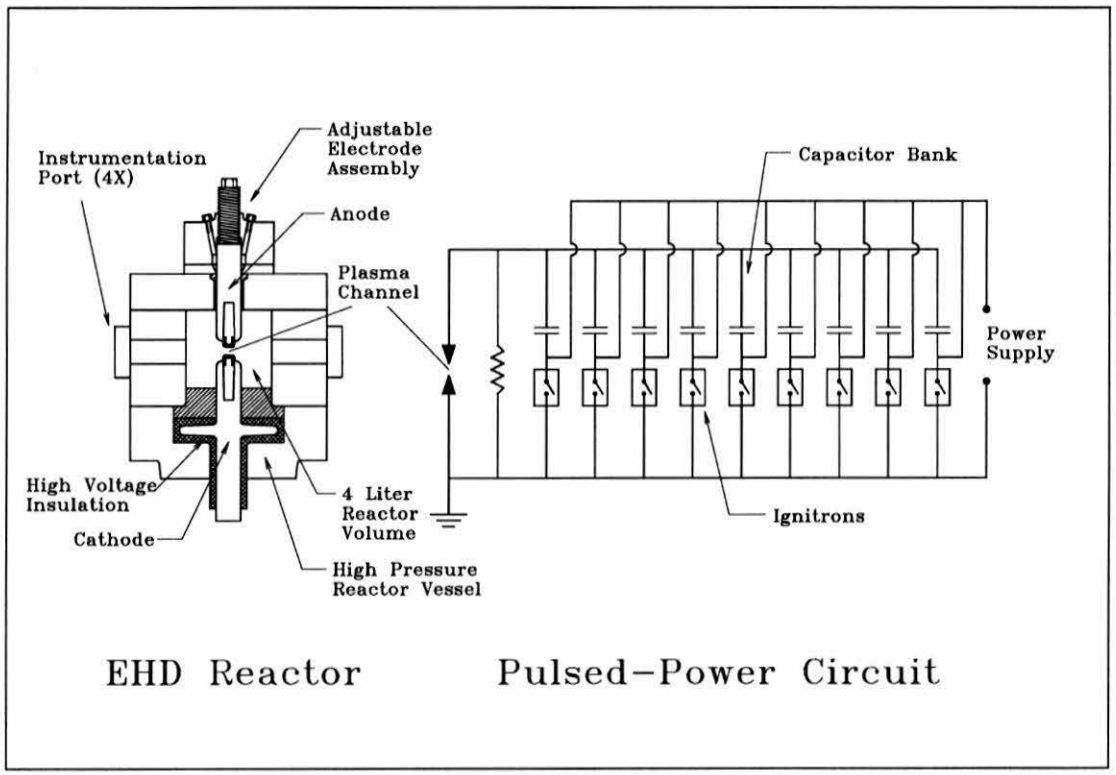

Figure 6.1
Schematic diagram of the *EHD* reactor and electronic circuit. The reactor is shown on the left, and the layout of the electronics representing the energy storage circuit and fast switches is shown on the right.

discharge method is similar in this operation to non-thermal plasmas, although it has also been applied to the treatment of liquid-phase wastes [13].

In the *EHD* process, chemical degradation also occurs within the plasma channel directly due to pyrolysis and free radical reactions. However, the small volume of the plasma channel (1-3 *mL*) limits the amount of solution that can be treated directly by

high temperature processes. On the other hand, experiments with exploding wires have shown that electrohydraulic discharges induce extreme electromagnetic and mechanical conditions in the bulk solutions outside of the plasma channel region [8,9,11,14]. These experiments have established that there are three primary physical processes — ultraviolet (*UV*) photolysis, electrohydraulic cavitation,and supercritical water oxidation — with the potential to induce significant oxidative chemistry in the bulk solution.

The plasma channel formed during an electrohydraulic discharge reaches temperatures of 10,000 - 50,000 *K* and thus functions as a blackbody radiation source with a maximum emittance in the vacuum ultraviolet (*VUV*) region of the spectrum (λ = 75 - 185 *nm*) [9]. The *VUV* emitted from the hot plasma is absorbed by the water layer immediately surrounding the plasma channel [15], and the *UV* light (λ > 185 *nm*) penetrates into the bulk of the solution. During the formation of the plasma channel (1 -2 μs) an intense 5 to 20 *kbar* shockwave is generated, due to the rapidly expanding plasma [8]. The resulting shockwave can induce pyrolytic and free radical reactions indirectly via electrohydraulic cavitation [12]. As the plasma channel cools over 1-3 ms, thermal energy is transferred to the surrounding water resulting in the formation of a steam bubble [11]. Within the steam bubble, the temperatures and pressures are high enough for the formation of transient supercritical water [14].

The simultaneous occurrence of multiple oxidative processes makes the chemistry of the *EHD* process extremely complicated. In an attempt to differentiate between these processes we group them into *localized* and *extended* effects. We define oxidative degradation that occurs within the plasma channel and within the immediate vicinity as "*localized.*" This includes pyrolysis within the high temperature plasma,

oxidation due to direct and indirect *VUV* photolysis, and supercritical water oxidation. Oxidative degradation resulting from shockwaves and *UV* radiation in the bulk aqueous solution is defined as "*extended.*"

6.2 Experimental Methods

6.2.1 The Pulsed-Power Plasma Reactor System

A schematic diagram of the important features of the Caltech *EHD* facility is shown in Figure 6.1. The reactor chamber has been designed to withstand the extreme electrical and mechanical stresses that are generated during an *EHD* event. Furthermore, it has been designed to provide reproducible conditions for >100,000 discharges. The high-voltage cathode bulkhead penetration assembly is the most critical component of the reactor. The insulation on the cathode must hold off a potential of at least 25 *kV* without shorting, and must be resistant to the erosive effects of intense shockwaves.

An opposing electrode design was selected for shock resistance and adjustability. The adjustable ground electrode assembly allows for the precise control ($\pm$ 0.1 *mm*) of the spark gap length within a range of 0 - 30 *mm*; it maintains the structural integrity of the chamber; and it provides a tight compression connection for the high current pulses. The ground electrode can be readjusted to maintain a constant spark-gap separation to offset erosion of the electrode tips. Tantalum was selected for the electrode tips because it is a refractory metal (mp = 2996°C) which minimizes electrode erosion; and tantalum and its oxide are relatively inert and do not interfere significantly with the organic chemistry under investigation. The tantalum tips are joined to the steel electrodes by incorporating them into locking Morse taper

assemblies. Flat cylindrical tips are used to minimize the effects of tip erosion during the lifetime of an experiment.

The electronics package, as illustrated in Figure 6.1, is a specialized RLC circuit designed and built by Pulsed-Power Technologies Inc. It has been specifically designed with a low inductance (250 -300 *nH*) and a relatively large capacitance (135 μF) to generate short high energy pulses. It is capable of delivering a 20 μs pulse with a total energy of 25 *kJ* and a peak power of up to 1 *GW*. Fast ignitron switches (300 *ns* risetime) are used to trigger the discharge.

Electrical current was measured on the hot electrode bus (cathode) using a Rogowski coil that has been calibrated against a 123.3 μΩ current viewing resistor from *T & M* Research. Voltages were measured on the cathode bus bar using a high voltage probe from North Star Research. Triggering of the circuit and collection of the current and voltage traces was done remotely using an Intel 486-66 PC loaded with National Instruments' LabView software.

As a specialized RLC circuit, a given discharge can be described by the governing differential equation;

$$L\frac{d^2q}{dt^2} + R(t)\frac{dq}{dt} + \frac{q}{C} = 0, \qquad 6.1$$

where L is the inductance of the circuit, C is the capacitance, and q is the stored charge. $R(t)$ is the resistance of the circuit and is dominated by the time-dependent

resistance of the plasma channel. Depending on the specific values of R, L, and C there are three regimes of discharge operation, underdamped $R < 2(L/C)^{1/2}$, critically damped $R = 2(L/C)^{1/2}$, and over-damped $R > 2(L/C)^{1/2}$. All discharges in our experiments were either underdamped or critically damped (*i.e.,* most discharges exhibit current reversal).

In a typical *EHD* experiment the large capacitor bank was charged to U_{CB} = 10.2 *kV*, which yielded the total stored energy of E_{CB} = 7 *kJ*. Subsequently the capacitor bank was discharged very rapidly using fast ignitron switches thereby charging the submerged electrodes. At this voltage the electric field strength is insufficient to cause the formation of a plasma channel directly through liquid water. Prebreakdown ionic current heats the water in the spark gap forming gas bubbles through which the discharge will occur [10]. The prebreakdown processes significantly reduce the energy available for the discharge itself from E_{CB} = 7 kJ to E_D = 2 *kJ*. After a plasma channel is formed, a current pulse arcs across the underwater spark-gap (0.8 cm). Since the plasma channel is the major resistive element in the circuit, the majority of the energy in the current pulse in deposited into the solution in the reactor chamber.

A representative set of current vs. time and voltage vs. time transients for the three different discharge configurations are shown in Figure 6.2. For 3.5 L experiments with 4-chlorophenol (*4-CP*), 3,4-dichloroaniline (*3,4-DCA*) and 2,4,6-trinitrotoluene (*TNT*), the total energy of the capacitor bank was set to E_{CB} = 7 kJ. The voltage on the cathode at the time of discharge was U_D = 5.5 ± 0.3 kV; and the energy delivered in the *EHD* pulse was E_D = 2.0 ± 0.2 kJ. The peak current of these pulses was typically 90 kA. We use E_{CB} rather than E_D for all efficiency calculations,

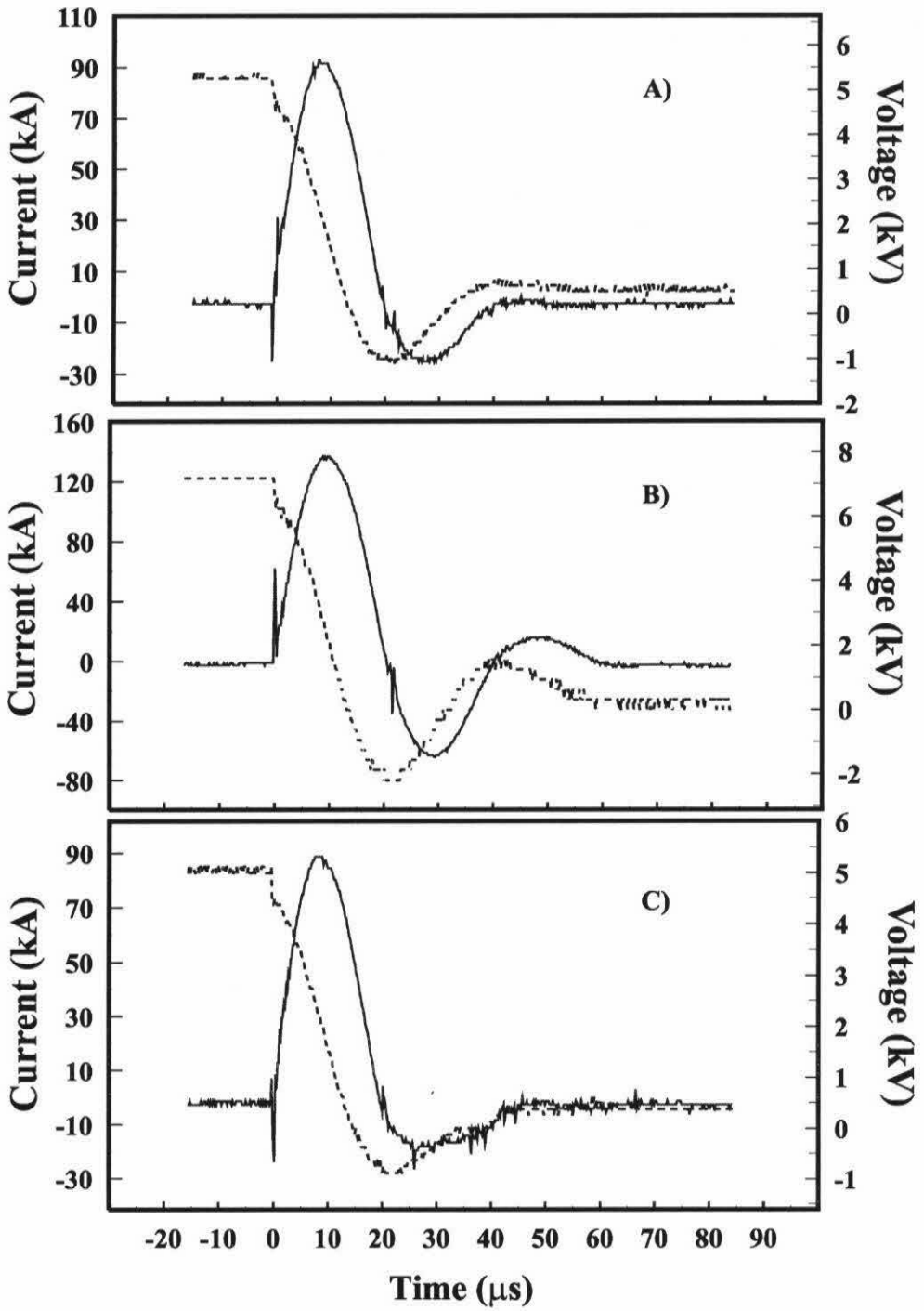

Figure 6.2

Current and voltage transients for the three different *EHD* conditions used in this study: A) V_T = 1.0 L, E_{CB} = 4.0 kJ. B) V_T = 1.0 L, E_{CB} = 7.0 kJ. C) V_T = 3.5 L, E_{CB} = 7.0 kJ. The solid and dashed lines are for the current and voltage transients respectively.

since it includes all of the energy losses due to the prebreakdown phenomena. Furthermore, it is possible that thermal degradation of organic substrates occurs during the prebreakdown period.

A high density polyethylene liner was used to reduce the chamber volume from 3.5 to 1.0 L. An unexpected side effect of the liner was the reduction of voltage losses during the pre-discharge initiation period due to ionic currents. With the liner installed, and the energy of the capacitor bank set to E_{CB} = 7 kJ, the voltage on the cathode at the time of discharge was $U_D = 7.2 \pm 0.2$ kV. The energy delivered in the *EHD* pulse was $E_D = 3.5 \pm 0.2$ kJ. For this reason, an additional set of 1.0 L experiments were performed with E_{CB} = 4 kJ. At this initial stored energy the voltages and energies of the *EHD* pulses more closely matched those of the 3.5 L / 7 kJ experiments. The voltage at the time of discharge, was $U_D = 5.2 \pm 0.1$ kV, and the energy of the *EHD* pulse was $E_D = 1.9 \pm 0.2$ kJ.

We define the lifetime of an *EHD* pulse as the period of time between the first and last time the current pulse reaches 10 % of its peak value. The duration of the pulse can be directly related to the voltage at the initiation of the plasma channel. For experiments run at 7 kJ in 3.5 L, the average current pulse lasted 41 ± 4 μs. The average current pulse for experiments run at 4 kJ in 1.0 L lasted for 40 ± 6 μs. The current pulses for experiments run at 7 kJ in 1.0 L were 51 ± 5 μs, approximately 25 % longer than for the other two experiments.

6.2.2 Materials

4-CP (Aldrich), p-benzoquinone (Aldrich), NaH_2PO_4 (EM Science), and hydroquinone (J. T. Baker) were used as received. *TNT* was obtained from Chem

Service at 99% purity (with added water for safety) and was dried before use. *3,4-DCA* (Lancaster) was recrystalized twice in toluene before use. Ozone measurements were made using potassium 5,5,7-indigotrisulfonic acid (Sigma). All solutions were made with water obtained from a MilliQ-*UV*-Plus System (R=18.2 $M\Omega\ cm^{-1}$).

NaH_2PO_4 salt was added as an electrolyte to all the solutions described in this paper to increase the conductivity and to ensure rapid formation of the plasma channel across the underwater electrode gap. A salt concentration of 0.015 M was determined experimentally to be the minimum value to facilitate reproducible *EHD* discharges across a 0.8 cm spark-gap. NaH_2PO_4 was used because of its low reactivity with hydroxyl radicals ($k_{OH\cdot}$ = 2.0 x 10^4 $M^{-1}s^{-1}$) [16]; which are produced during an electrohydraulic discharge. *4-CP*, which has a pK_a = 9.4, is present in the protonated form at pH = 5. *3,4-DCA* , with a pK_a = 2.9, is present in its neutrally charged deprotonated form.

Ozone was generated with an OREC Model V10-0 Ozonator set at 1 *AC* amp with a flow rate of 2 LPM. The solution was sparged with ozone using a specially built HDPE insulating disk with eleven 0.015" diameter vents. The O_3/O_2 mixture was pumped into the disk with a tube from the generator outside the chamber.

6.2.3 Analytical Procedures

The concentrations of *4-CP*, *p*-benzoquinone, *p*-hydroquinone, 4-chlorocatechol, and 4-chlororesorcinol were determined using a Hewlett Packard Series II 1090 HPLC with a *UV*-VIS diode array detector and a reverse phase column [17]. Analysis was done within four hours of the experiment. Chloride ion concentration was obtained

using an Orion Model 94-17B chloride electrode. The disappearance of *3,4-DCA* and *2,4,6-TNT* was monitored with HPLC. 3,4-*DCA* was separated from its oxidation products on a normal-phase column (Hewlett-Packard 5 μm MOS hypersil) using a gradient elution program (100% H_2O to 60:40 H_2O:CH_3CN at 1 mL per minute). *2,4,6-TNT* concentrations were measured with a Hewlett-Packard Hypersil BDS column and an isocratic 24:76 CH_3OH:H_2O mixture at a flow rate of 0.725 mL/min. In the *TNT*/ozone experiments samples were analyzed for total organic carbon (*TOC*) with a Shimadzu (TOC-500). Dissolved ozone concentrations were determined using the method of Bader and Hoigne [18].

6.2.4 Experimental Procedures

To determine the primary oxidative mechanisms operative in an *EHD* reactor we performed three sets of experiments. First, we treated an aqueous solution of *4-CP* with one hundred and twenty 7 kJ discharges, and determined the distribution of product concentrations. Since the degradation of *4-CP* by direct photolysis [19-23], TiO_2 photocatalysis [1,24,25], and sonolysis [6] have been investigated previously, the product distributions from each of these methods are known. Comparison of the observed product distribution with those reported in the literature yields insight into the predominant mechanism of degradation within an *EHD* reactor. A 3.5 L air-saturated solution of 200 μM *4-CP* at pH = 5 (0.015 M NaH_2PO_4) was exposed to one hundred and twenty 7 kJ electrohydraulic discharges in the *EHD* reactor. Samples were taken every 5 discharges for the first 40 shots, and every ten discharges thereafter. There was a small temperature rise of 8 °C over the lifetime of the experiment.

The second set of experiments explored the kinetics of the reactor using three different compounds, *4-CP*, *3,4-DCA*, and *TNT*. In these experiments the initial rate of substrate oxidation was measured as a function of initial substrate concentration. Since direct photolysis was suspected to be a major oxidative pathway in the *EHD* process we studied three compounds with widely different quantum yields [26-28]. These compounds are all priority pollutants and groundwater contaminants [29,30]. Furthermore, their low volatility and reasonably high solubility make them ideal for study in an *EHD* reactor. In order to determine the relative contribution of localized verses extended degradative mechanisms, the volume dependence of the degradation rates was also explored.

Apparent zero-order rate constants were measured as a function of the initial concentration of *4-CP* over the range of 50 – 800 μM. The experimental procedures were the same for each concentration (*i.e.*, 3.5 L of *4-CP* solution were treated with twenty five 7 kJ electrohydraulic discharges). Three independent 0.5 mL samples were taken after every five discharges and analyzed for *4-CP* and benzoquinone. The initial degradation rates were also measured for a 1.2 L volume reactor. In these experiments 1.0 L of *4-CP* solution was treated with 10 electrohydraulic discharges, and three independent 0.5 mL samples were taken after every two discharges. A HDPE volume-reduction liner was used for the 1.0 L experiments. At both volumes, there was 2.25 cm of free space above the solution to facilitate mixing between discharges.

Initial degradation rates were also measured for *3,4-DCA*, and *TNT*. Both of these experiments were run with the reaction chamber in the 3.5 L configuration (without the liner). The *3,4-DCA* solutions were exposed to forty 7 kJ discharges, and were

sampled after each five discharges. Initial concentrations of the 3,4-*DCA* solutions studied ranged from 100–800 μM. The *TNT* degradation kinetics experiments were performed similar to those for *4-CP* and *3,4-DCA*. The *TNT* solutions were treated with thirty 7 kJ discharges, and were sampled after every five discharges. Since the solubility of *TNT* is low, the maximum concentration of the solutions studied was 350 μM.

Direct photolysis by *UV* radiation rarely leads to complete mineralization of an organic substrate [7]. The third set of experiments examined the combination of a chemical oxidant, ozone, with the *EHD* reactor. *TNT* was chosen as the test compound for these experiments since it is refractory to both direct *UV* photolysis, and to dark reactions with ozone.

A 3.5 L solution of 159 μM *TNT,* and 15 mM NaH_2PO_4 was treated with two hundred and sixty 7 kJ electrohydraulic discharges. The solution was sparged with an O_3/O_2 gas mixture at the rate of 2 LPM for the duration of the experiment to maintain a steady-state ozone concentration. However, a true steady-state concentration could not be maintained as the temperature of the solution varies significantly during an experiment of this duration. The initial solution temperature was 23 °C and it increased linearly to a maximum value of 40 °C over 260 electrohydraulic discharges. The ozone concentration thus fluctuated from a higher value at low temperatures to a lower value at higher temperatures; several ozone measurements were made and an average ozone concentration for the experiment was determined to be 90 μM.

6.3 Results

6.3.1 4-CP Reaction Products

The chemical results of this experiment are shown in Figure 6.3. A 35 % conversion of *4-CP* was obtained after one hundred and twenty 7 kJ discharges (Figure 6.3). Chloride ion production was found to be stoichiometric within experimental error

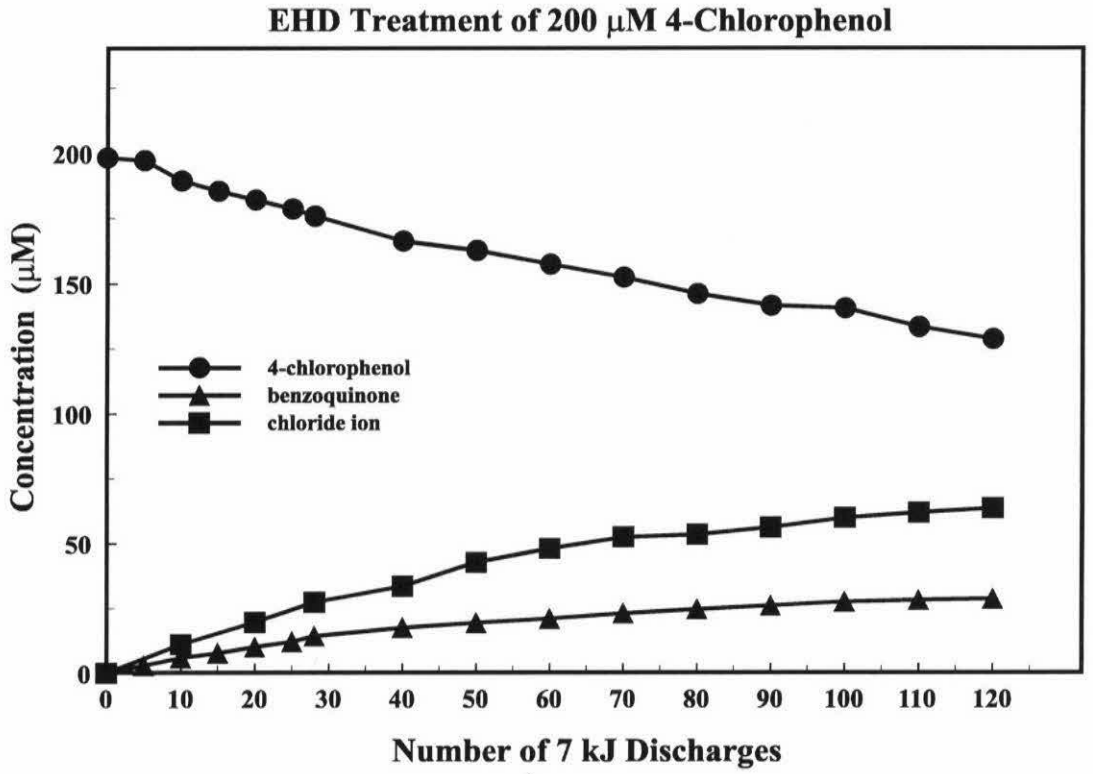

Figure 6.3

Treatment of a 3.5 liter, 200 μM *4-CP* solution (pH 5) with one hundred and twenty 7 kJ electrohydraulic discharges. Shown are the transients for the degradation of *4-CP*, and the production of benzoquinone and chloride ions.

(*e.g.*, 70 μM *4-CP* was degraded while 64 μM Cl^- was produced after 120 discharges, accounting for 91% of converted *4-CP*). 41% of the degraded *4-CP* was accounted for in the form of *p*-benzoquinone. Small concentrations of hydroquinone were detected, possibly due to the photolysis of benzoquinone or from redox equilibration with the benzoquinone in the sample vials. 4-Chlorocatechol, and 4-chlororesorcinol were not detected at greater than or equal to the 1 μM detection limit.

6.3.2 Kinetics Experiments

Direct photolysis reactions obey the following rate equation,

$$-\frac{dC}{dt} = \Phi(\lambda) I_0(\lambda, t)\left(1 - \exp(-2.303\varepsilon l C)\right) \qquad 6.2$$

where C is the concentration of the reactant, $\Phi(\lambda)$ is the photolysis quantum yield, I_0 is the intensity of the *UV* source, ε is the substrate extinction coefficient, and l is the pathlength of radiation.

Since the *UV* source in the *EHD* reactor is pulsed, $I_0(\lambda,t)$ varies significantly over the lifetime of the pulse. However, the total energy per discharge is a well-defined quantity. Thus, we assume that the total *UV* flux per discharge is relatively constant as long as the discharge conditions remain constant. Under these conditions we can replace t with the number of discharges, N, to obtain,

$$-\frac{dC}{dN} = \Phi(\lambda) Q(\lambda)\left(1 - \exp(-2.303\varepsilon l C)\right) \qquad 6.3$$

which for large values of εlC gives,

$$-\frac{dC}{dN} = \Phi(\lambda)Q(\lambda) = k_0, \qquad 6.4$$

where $Q(\lambda)$ is the radiant energy per discharge. Since N is dimensionless, the rate constants will have non-conventional units. A zero-order rate constant, k_0, will have dimensions of μM discharge^{-1}, and a first-order rate constant, k_1, will have dimensions of discharge^{-1}. Later in the discussion section we will relate these N-based kinetic constants to the intrinsic rate constants based on time.

As seen in Figure 3 the degradation of *4-CP* deviates from linear kinetics at $N >$ 30. This may be due to competitive absorption of the *UV* radiation by the accumulating light-absorbing reaction products and the Ta/Ta_2O_5 particles from the erosion of the electrodes during successive discharges. Given this limitation, the zero-order rate constants are based on the initial rates of disappearance of *4-CP* ($N <$ 25).

The values of the apparent initial zero-order rate constants (k_A = - *dC/dN*) are shown in Figure 4 as a function of initial concentration. The decline in rate at low concentrations (< 150 μM) is consistent with the exponential term in eq 6.3. At these low concentrations the *UV* radiation from the plasma channel is not completely absorbed by the solution. This decline starts at higher concentrations for the 1.0 L experiment since the maximum pathlength l is shorter when the HDPE liner is installed in the chamber.

However, at higher concentrations, the strong dependence of the apparent rate constant on the initial concentration is not consistent with eq 6.4. As long as the *UV* radiation from the plasma channel is completely absorbed by the primary chromophore, there should be no dependence of k_A on concentration. Therefore, either the strong absorbance approximation is invalid, or an additional reaction pathway is indicated.

The simplest model to account for the trends observed in Figure 6.4 is to consider the *EHD* system to be a two compartment reactor. The first reactor compartment is the bulk solution which is exposed to the extended effects (*UV* and

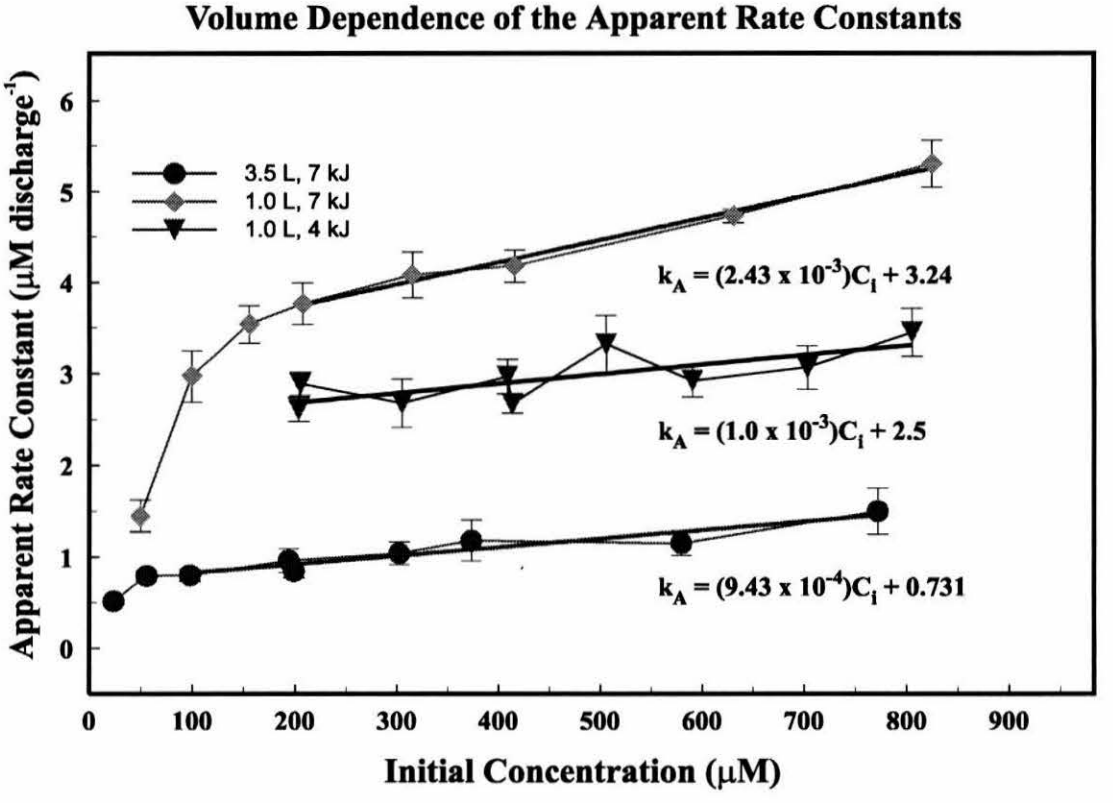

Figure 6.4
Apparent initial rate constants (k_A) vs. initial concentration (C_i) for the three sets of volume dependence experiments performed on *4-CP* .

shockwave radiation) generated by the *EHD* discharge. Discounting any cavitational effects generated by the shockwave, degradation in this region is purely photochemical.

The second reactor compartment is the small volume contained within and immediately surrounding the plasma channel. The solution in this region is exposed to the *localized* chemical effects. The substrate is oxidized within the high temperature plasma channel and by hydroxyl radicals generated by the *VUV* photolysis of water. Since the conditions in and around the plasma channel are so extreme, it is assumed that any substrate within this region will be completely oxidized. These combined processes will appear to be first-order in kinetic behavior when they are considered over the scale of the entire reactor (*vide infra*).

If the solution in the reactor chamber is well-mixed after one discharge the measured concentration of the substrate will be,

$$C = \left(\frac{V_T - V_R}{V_T}\right) C_i - k_0 \qquad 6.5$$

where C_i is the initial concentration, V_T is the total solution volume, V_R is the plasma channel volume, and k_0 (units of μM discharge^{-1}) is the zero-order rate constant due to direct photolysis. After N discharges, it can be shown that the measured concentration will be,

$$C = a^N C_i - k_0 \sum_{n=0}^{N-1} a^n = a^N C_i - k_0 \frac{\left(1 - a^N\right)}{(1 - a)} \qquad 6.6$$

where,

$$a = \left(\frac{V_T - V_R}{V_T} \right). \qquad 6.7$$

Since N can be treated as a continuous variable for the kinetics analysis, the derivative of eq 6.6 with respect to N yields,

$$\frac{dC}{dN} = = e^{ln(a)N} C_i + k_0 \frac{ln(a)e^{ln(a)N}}{(1-a)}. \qquad 6.8$$

Since $a \approx 1$ and N < 40, we can assume that $\ln(a) = (a\text{-}1)$ and $\exp(\ln(a)N) = (1 + \ln(a)N)$ to obtain,

$$\frac{dC}{dN} = ln(a)C_i - k_0 - k_0\, ln(a)N + ln^2(a)NC_i \ . \qquad 6.9$$

The last two terms of eq 6.9 can be neglected since they are much smaller in magnitude than the first two terms and are much smaller than the experimental error. Therefore, the differential equation that describes the initial rate of degradation in an *EHD* reactor can be described as the sum of zero and first-order terms as follows:

$$\frac{dC}{dN} = -k_1 C_i - k_0 = -k_A. \qquad 6.10$$

The observed first-order rate constant will be $k_1 = -\ln(a)$. The value of k_1 is a function of the ratio of V_R to V_T. In our reactor $V_R << V_T$, and therefore k_1 has a small, ($\approx 9 \times 10^{-4}$ discharge^{-1}) but significant effect.

Theoretically the data of an individual experiment should fit to eq 6.6. However, an inherently large shot-to-shot noise, a small number of experimental points, and the small values of k_1 make this impractical. Under these conditions the nonlinear least squares fitting routine rarely converges. However, eq 6.10 shows that k_A is linearly dependent on C_i where the slope yields a value for k_1, and the y-intercept yields a value for k_0. The resulting fitted values are summarized in Table 6.1. The values obtained for k_0 and k_1 can be substituted into eq 6.6 to calculate predicted experimental transients. Figure 6.5 shows the predicted dependence of C as a function of N for a *4-CP* solution (C_i = 302 μM) compared with the experimentally determined values. The predicted transients fall within experimental error of the observed rates.

Table 6.1

Experimentally Determined Constants

	k_0 (μM/dis.)	k_1 (10^{-4}/dis.)	V_R (mL)	Intrinsic Rate Constant (M/s)	G* Value (10^{-4})	Reaction Quantum Yield (Φ_r)	Ref.
4-Chlorophenol *(3.5 L, 7 kJ)*	0.73 ± 0.08	9.4 ± 1.4	3.5 ± 0.5	0.022	44	0.25	32
4-Chlorophenol *(1.0 L, 7 kJ)*	3.25 ± 0.08	24.3 ± 1.5	2.4 ± 0.2	0.073	52		
4-Chlorophenol *(1.0 L, 4 kJ)*	2.5 ± 0.36	12 ± 7	1.2 ± 0.7	0.054	38		
Dichloroaniline	0.17 ± 0.03	8.2 ± 0.6	2.8 ± 0.1	0.008	16	0.044	34
Trinitrotoluene	0.10 ± 0.03	5.6 ± 1.0	1.9 ± 0.4	0.005	10	0.0021	33
Trinitrotoluene + Ozone				0.024	48		

* These values are reported for a representative 200 mM solution of the substrate; with the exception for the TNT/ozone experiment which is at 160 mM.

Additional evidence for the validity of the two-term rate expression is evident in Figure 6.6 which shows benzoquinone production as a function of N for a number of initial concentrations. When $C_i \geq 100$ μM benzoquinone production is constant within experimental error. As discussed previously, benzoquinone is the predominant product of the direct photolysis of *4-CP*. Figure 6.6 clearly shows that within the bulk-phase compartment of the reactor, *UV* photolysis is zero-order and independent of the initial concentration.

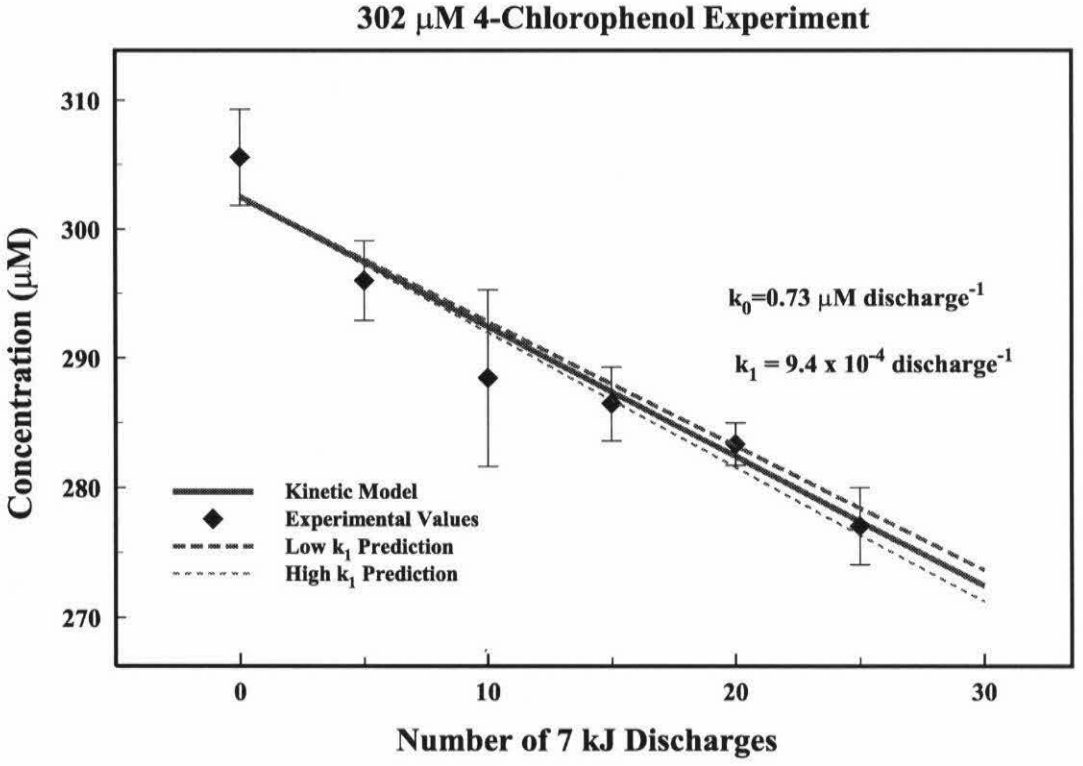

Figure 6.5

The data of a 302 μM *4-CP* experiment superimposed on the transient obtained from Eq 6.6 and the experimentally determined values for k_0 and k_1.

The degradation rates of 3,4-*DCA* and *TNT* were studied and analyzed by the same kinetic scheme applied to *4-CP*. Figure 6.7 shows the experimental results for

the 3.5 L experiments on *4-CP*, 3,4-*DCA* , and *TNT*; in which the values of k_A are plotted against C_i. The corresponding values of k_0 and k_1 are given in Table 6.1.

If the solution in the reactor chamber is well mixed after one discharge the change in the concentration of the substrate will be,

$$\Delta C = -\frac{V_R}{V_T} C - \int_{185nm}^{visible} \Phi(\lambda)\, Q(\lambda)\left[1 - \exp\{-2.303\varepsilon(\lambda) l C\}\right] d\lambda , \qquad 6.11$$

where C is the concentration, V_T is the total solution volume, and V_R is the plasma channel volume.

Since *TNT*, *4-CP* and *3,4-DCA* are strong absorbers in the 185-300 nm region of the spectrum, we can assume that *UV* radiation with wavelengths shorter than some λ_{cutoff} near 300 nm will be strongly absorbed. The absorbance of *UV* with wavelengths longer than λ_{cutoff} will depend on the concentration of the solution. Thus eq 6.11 can be written as follows,

$$\Delta C = -\frac{V_R}{V_T} C - \int_{185nm}^{\lambda_{cutoff}} \Phi(\lambda)\, Q(\lambda)\, d\lambda - \int_{\lambda_{cutoff}}^{visible} \Phi(\lambda)\, Q(\lambda)\left[1 - \exp\{-2.303\varepsilon(\lambda) l C\}\right] d\lambda . \qquad 6.12$$

The second term in eq 6.12 is a constant, k_0. The third term cannot be rigorously evaluated unless the function $Q(\lambda)$ is known. If $\varepsilon(\lambda)$ is small when $\lambda > \lambda_{cutoff}$ then eq 6.12 can be approximated by,

$$\Delta C = -\frac{V_R}{V_T} C - k_0 - 2.303 l C \int_{\lambda_{cutoff}}^{visible} \Phi(\lambda) Q(\lambda) \varepsilon(\lambda) d\lambda . \qquad 6.13$$

If we make the following definitions:

$$k_1^{\lambda} = 2.303 l \int_{\lambda_{cutoff}}^{visible} \Phi(\lambda) Q(\lambda) \varepsilon(\lambda) d\lambda, \quad k_1^{local} = \frac{V_R}{V_T}, \quad k_1 = k_1^{local} + k_1^{\lambda} \qquad 6.14$$

then eq 6.13 can be written as

$$\Delta C = -k_1 C - k_0 . \qquad 6.15$$

Eq 6.15 shows that the amount of substrate converted during each discharge should be linearly dependent on the initial concentration, and this is experimentally observed. The question remains whether the linear term results predominantly from localized reactions within the plasma channel region, or if it is due to photolysis by the weakly absorbing region of the *EHDs* emission spectrum.

Clearly we cannot quantitatively answer the above question until $Q(\lambda)$ is experimentally determined. However, two different experimental results indicate that k_1^{local} dominates the linear term in eq 6.15. First, Figure 6.6 shows that benzoquinone production is constant when the initial concentration of *4-CP* is $\geq$ 100 μM even though the amount of *4-CP* converted increases 80% as C_i varies from 100 - 800 μM.

Since benzoquinone is the primary photolysis product, one would expect its production to depend on the initial concentration of *4-CP* if photolysis was responsible for k_1. Although not conclusive, product analysis indicates that the localized plasma channel effects are predominant.

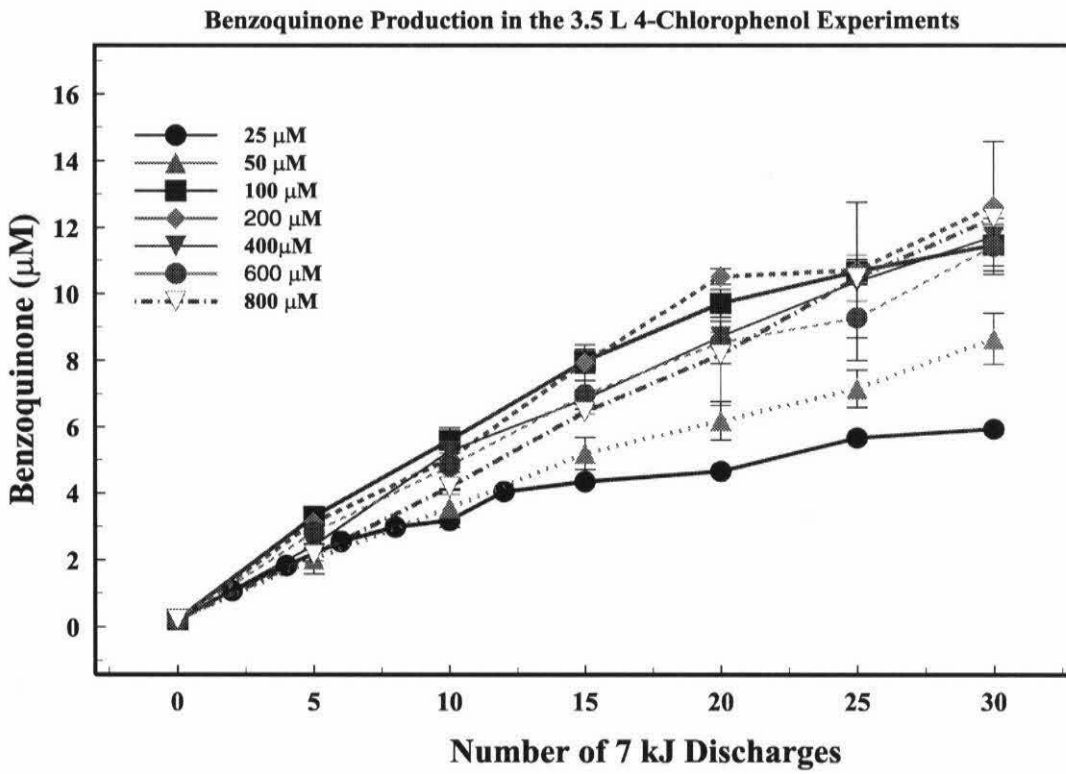

Figure 6.6

The data of a 302 μM *4-CP* experiment superimposed on the transient obtained from Eq 6.6 and the experimentally determined values for k_0 and k_1.Benzoquinone production as a function of the number of discharges for the 3.5 L *4–CP* experiments. The transients shown are for seven experiments with different initial concentrations of *4-CP*.

Second, the invariability of k_1 with respect to the compound also indicates that localized plasma channel effects dominate the linear term in eq 6.15. Since the environment within the plasma channel compartment is extremely harsh, oxidation of organic substrates within this region is non-selective. Therefore, if localized plasma channel effects predominate, k_1 should not vary significantly from one compound to another. Conversely, k_1^{λ} is dependent on $\Phi(\lambda)$ for the specific compound. If photolysis mechanisms are predominant, k_1 should be highly dependent on $\Phi(\lambda)$. Figure 6.7 shows that the values of k_1 for both *4-CP* and *3,4-DCA* are equivalent within experimental error. The value of k_1 for *TNT* is slightly less, but is within a factor of two of the values for the other two compounds.

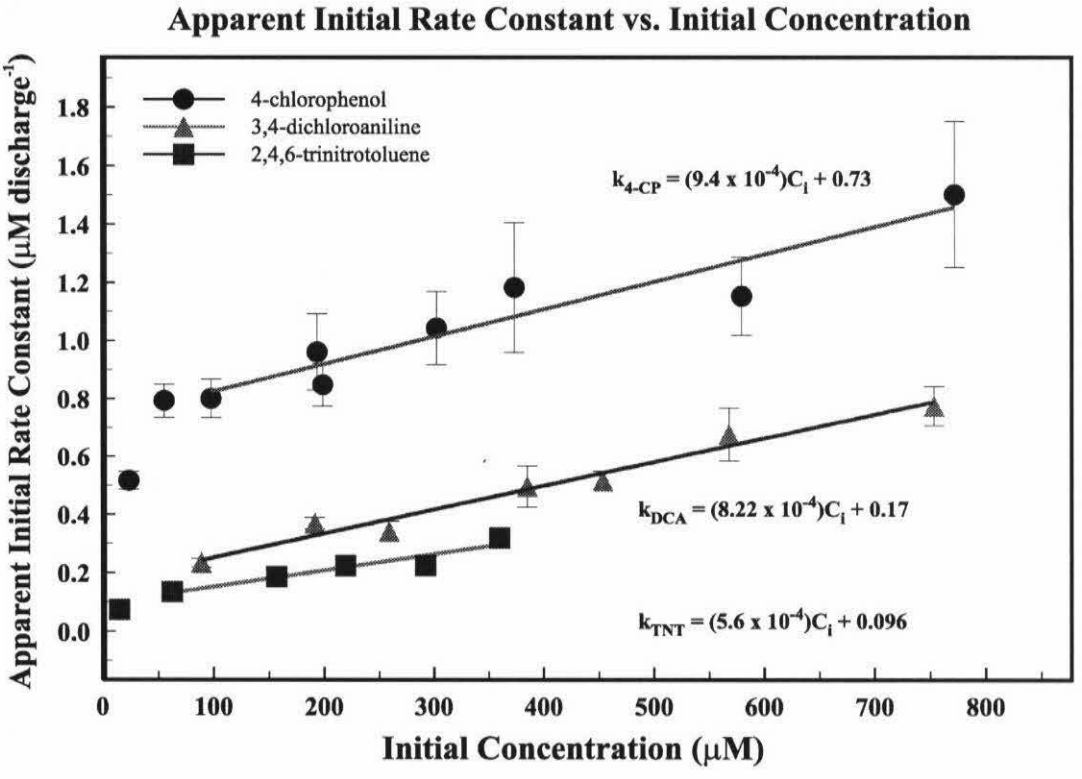

Figure 6.7
Apparent initial rate constants (k_A) vs. the initial concentration (C_i) for the three compounds studied, *4-CP*, *3,4-DCA*, and *TNT*.

6.3.3 Combined EHD/Ozone Treatment of TNT

For most organic compounds, *UV* irradiation alone is insufficient to result in complete mineralization [7]. Therefore, most photochemically based *AOTs* use *UV* radiation in combination with high redox potential chemical oxidants such as ozone or hydrogen peroxide. Photolysis of ozone produces hydroxyl radicals, which can efficiently oxidize refractory organic compounds that may not be susceptible to direct photolysis.

The combined *EHD*/ozone process was able to completely degrade a 159 μM *TNT* solution to less than detection limits (< 1 μM) over the duration of a 260 discharge experiment (Figure 6.8). The HPLC method used measured the *TNT*

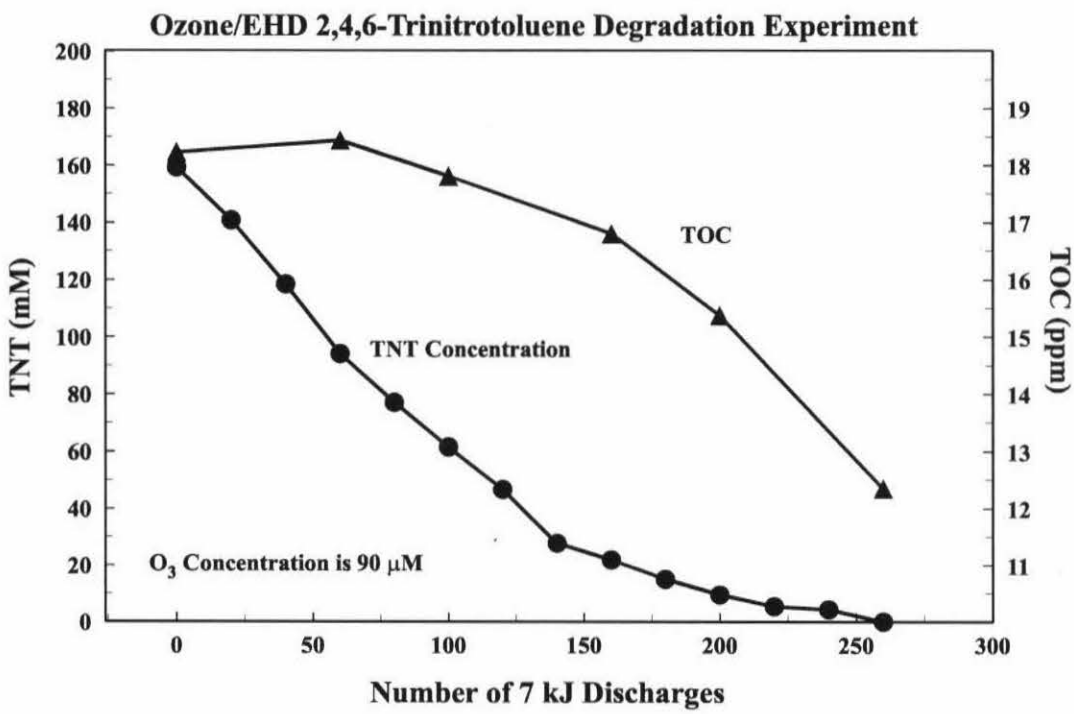

Figure 6.8
TNT concentration and *TOC* as a function of the number of discharges for the combined *EHD*/ozone experiment discussed in the text.

concentration, but did not detect oxidative intermediates. The overall *TNT* degradation kinetics appear to be complicated; however, the first 80 discharges can be fit to an apparent zero-order rate constant k_A = 1.0 ± 0.1 μM discharge^{-1}. The total organic carbon (*TOC*) content of the solution decreased by 34% from 18 ppm to 12 ppm. A control ozone experiment run for an equivalent time but without electrohydraulic discharges showed only a 7 % decrease in the *TNT* concentration.

6.4 Discussion

Reaction product distributions strongly indicate that direct photolysis is the primary mechanism of degradation of *4-CP* in the *EHD* reactor. The products observed are consistent with the distributions reported in the literature for aqueous-phase photolysis of *4-CP*. Stoichiometric production of chloride ions is consistent with the photochemical mechanism of *4-CP* which involves cleavage of the C-Cl bond in the first step [19]. Furthermore, in aqueous phase flash-photolysis experiments on *4-CP*, *p*-benzoquinone and hydroquinone are the primary and secondary photolytic degradation products [20,21,23].

Shockwaves produced during an *EHD* discharge could cause cavitational effects similar to those observed in sonochemical experiments [4,5,12]. Sonolysis of an aqueous solution of *4-CP* is known to oxidize *4-CP* to hydroquinone, 4-chlororesorcinol and 4-chlorocatechol (7). The sonolytic oxidation of *4-CP* proceeds primarily via reactions with hydroxyl radicals rather than by pyrolysis. At a concentration of 200 μM, if electrohydraulic cavitation is occurring, *4-CP* should react with hydroxyl radicals in the hydrophobic bubble interfacial regions. However,

the products of the sonolytic degradation of *4-CP* are not the same as seen during *EHDR* degradation of *4-CP*. Thus, we conclude that cavitation induced during electrohydraulic discharges does not result in discernible *4-CP* degradation.

Given the compounds tested, it appears that the *EHD* reactor functions primarily via *UV*-induced photochemical processes combined with a significant secondary contribution from direct reactions within the plasma channel. The values of k_0 for a compound should, therefore, scale with its quantum efficiency for direct photolysis. The values for all three compounds are listed in Table 6.1, along with their reported quantum efficiencies for direct photolysis (Φ_r). The ratio of $k_0^{4CP}/k_0^{DCA} = 4.3$, which is in reasonable agreement with the ratio $\Phi_r^{4CP}/\Phi_r^{DCA} = 5.7$. However the ratio of $k_0^{DCA}/k_0^{TNT} = 1.7$ is an order of magnitude off of the value of $\Phi_r^{DCA}/\Phi_r^{TNT} = 21$. One possible reason is that the reported quantum efficiency, which was measured at $\lambda = 313$ nm is not valid at the shorter *UV* wavelengths used in this experiment. Secondly, degradation products are known to significantly enhance the photolysis of *TNT* [27].

As long as all *UV* radiation is absorbed by the solution, the total number of moles of substrate converted should depend only on the *UV* flux emitted from the plasma channel, (*i.e.*, independent of the volume of the chamber). Therefore, the value of k_0 should scale inversely with the volume of the chamber (since it is a molar quantity). Difficulty arises in determining the volume dependence of k_0 since the volume reduction liner changes the discharge characteristics of the plasma channel. Changes in the peak voltages, peak currents, and lifetime of the discharge can have significant effects on the emitted *UV* flux. Therefore, it is best to compare k_0 values for systems with closely matching discharge characteristics. As discussed above, the

7 kJ - 3.5 L experiments, and the 4.0 kJ - 1.0 L experiments have similar discharge characteristics. The ratio of k_o(1.0 L)/k_o(3.5 L) = 3.4, which is in excellent agreement with the inverse ratio of the volumes.

As predicted by eq 6.13 and 6.15, k_1 demonstrates moderate dependence on the reactor volume. Table 6.1 gives the plasma channel (V_R) volumes derived from the experimental k_1 values. The values of V_R range from 1.9 to 3.5 mL and are consistent with the physical dimensions of plasma channels measured in exploding wire experiments. Even though the plasma channel is small, its effects are measurable. Plasma channel effects can even be the dominant oxidative mechanism at high concentrations of substrate, especially for compounds such as *TNT*, which have moderately low photolysis rates. Furthermore, since the plasma channel cannot be physically isolated from the rest of the system, its effects are always present as an apparent *background* degradation rate.

The addition of ozone to the *EHD* reactor dramatically increases the *TNT* degradation rate and caused greater than 99% degradation within 260 electrohydraulic discharges. This enhancement must be due to the reaction of *TNT* with the hydroxyl radicals produced by the photolysis of ozone since the dark reaction of *TNT* with ozone is very slow. In order to determine the magnitude of the effect of ozone addition on k_A, the effects due to the plasma channel and direct photolysis need to be factored out.

The apparent initial zero-order rate of degradation of *TNT* in this experiment was k_A = 1.0 μM discharge^{-1}. Since there are no differences in the electrohydraulic discharge characteristics, plasma channel oxidation (k_1) should be the same as

observed in the *TNT* experiments shown in Figure 6.7. Thus 9% of the *TNT* degradation can be attributed to first-order processes. Likewise, *TNT* has a much higher extinction coefficient than ozone and will dominate in the absorption of *UV*. Therefore, direct photolysis of *TNT* could account for up to 10% of the observed initial degradation rate. From the ozone sparging control experiment approximately 7% of the *TNT* degradation could be due to dark reactions. Then, by process balance, ≈74 % of k_A is due to the combined effects of *EHD/O₃*.

While k_A of the combined *EHD/O₃* process is of the same order of magnitude as k_A for *4-CP*, a direct photolysis process, it is less susceptible to the accumulation of oxidation products and tantalum/tantalum oxide particles. This is apparent in that the rapid initial rate of *TNT* degradation continues down to lower concentrations before leveling off, compared to *4-CP* (Figure 6.3). Furthermore, in the case of *TNT* there is a significant reduction in the *TOC* indicating that 34 % of the *TNT* has undergone complete mineralization. Since the rate of disappearance of *TOC* appears to be accelerating, complete mineralization of an organic substrate is likely given that the experiment could be extended by increasing the number of discharges.

The energy efficiency of the *EHD* process can be determined by computing the *G*-values which are listed in Table 6.1. The *G*-value is defined as the number of substrate molecules converted per 100 eV of energy stored in the capacitor bank. If the *G*-value is defined according to the energy dissipated during the actual electrohydraulic discharge then the values are even higher. The listed *G*-values have been calculated for 200 μM solutions, and include both the contributions of direct photolysis and plasma channel reactions (k_0 and k_1). We note that, at present, the *EHD* reactor and power supply have not been optimized for maximum energy

efficiency, therefore, the calculated *G*-values are apparatus specific and are not intrinsic efficiencies.

For comparison, we can convert the *N-based* rate constants k_A, k_0, and k_1, to the more conventional intrinsic rate constants, based on real-time. If we assume that the average current pulse lasts 41 or 51 μs (depending on the reactor configuration) the intrinsic rate constants k_A^t range from 5×10^{-3} M s^{-1}, to 7.3×10^{-2} M s^{-1}. Since these constants are relatively large, the rate-determining factor for the treatment of a volume of solution will be the repetition rate of the electronic circuit. The current repetition rate is approximately six discharges per minute; however rates of 5 - 10 Hz are easily achievable using current technology. At a 10 Hz repetition rate, the total treatment time for degradation of 3.5 L of 160 μM *TNT* (99% degradation) would be approximately 30 seconds with the *EHD/O_3* process.

The *EHD* process is just beginning to be explored as a method of treating hazardous chemical wastes. The parameters that influence the efficiency of this process have yet to be optimized. The *EHD* discharge operates primarily as a high intensity *UV* light source. The oxidation of organic compounds in the reactor is primarily due to photochemical processes. However, oxidation within the plasma channel region is a significant secondary oxidative process; which may actually dominate the observed reaction rates at high substrate concentrations. When the *EHD* process is combined with ozone, it has the potential for the rapid and complete mineralization of hazardous wastes in very short periods of time (seconds to minutes).

References

[1] Hoffmann, M. R.; Martin, S. T.; Choi, W. Y.; Bahnemann, D. W. *Chemical Reviews* **1995**, *95*, pp. 69.

[2] Penetrante, B. M.; Schultheis, S.E. *Non-Thermal Plasma Techniques for Pollution Control Part A: Overview, Fundamentals and Supporting Technology*; Eds. Springer-Verlag: New York, 1993.

[3] Penetrante, B. M.; Schultheis, S.E. *Non-Thermal Plasma Techniques for Pollution Control Part B: Electron Beam and Electrical Discharge Processing*; .; Eds. Springer-Verlag: New York, 1993.

[4] Hua, I.; Höchemer, R. H.; Hoffmann, M. R. *Environ. Sci. Tech.* **1995**, (In Press).

[5] Hua, I.; Höchemer, R. H.; Hoffmann, M. R. *J. Phys. Chem.* **1995**, *99*, pp. 2335.

[6] Serpone, N.; Terzian, R.; Hidaka, H.; Pelizzetti, E. *J. Phys. Chem.* **1994**, *98*, pp. 2634.

[7] Legrini, O.; Oliveros, E.; Braun, A. M. *Chem. Rev.* **1993**, *93*, pp. 671.

[8] Martin, E. A. *J. Appl. Phys.* **1958**, *31*, pp. 255.

[9] Robinson, J. W.; Ham, M.; Balaster, A. N. *J. Appl. Phys.* **1973**, *44*, pp. 72.

[10] Naugolnykh, K. A.; Roy, N. A. *Electrical Discharges in Water. A Hydrodynamic Description.* technical report FTD-HC-2049-74, Foreign Technology Division, Wright-Patterson Air Force Base, Ohio. 1974.

[11] Buntzen, R. R. *The Use of Exploding Wires in the Study of Small-Scale Underwater Explosions.* In: *Exploding Wires, Vol 2;* Chace, W. G.; Moore, H. K. Eds. Plenum Press: New York, NY, 1962; pp. 195.

[12] Coleman, A. J.; Saunders, J. E.; Crum, L. A.; Dyson, M. *Ultrasound in Med. & Biol.* **1987**, *13*, pp. 69.

[13] Sharma, A. K.; Locke, B. R.; Arce, P.; Finney, W. C. *Hazardous Waste and Hazardous Materials* **1993**, *10*, pp. 209.

[14] Ben'kovskii, V. G.; Golubnichii, P. I.; Maslennikov, S. I.*Sov. Phys. Acoust.* **1974**, *20*, pp. 14.

[15] Jakob, L.; Hashem, T. M.; Burki, S.; Guindy, N. M.; Braun, A. M. *J. Photochem. Photobiol. A: Chem.* **1993**, *7*, pp. 97.

[16] Buxton, G. V.; Greenstock, C. L.; Helman, W. P.; Ross, A. B. *Journal of Physical and Chemical Reference Data* **1988**, *17*, pp. 738.

[17] Martin, S. T.; Morrison, C. L.; Hoffmann, M. R. *J. Phys. Chem.* **1994**, *98*, pp. 13695.

[18] Bader, H.; Hoigne, J. *Water Res.* **1981**, *15*, pp. 449.

[19] Boule, P.; Guyon, C.; LeMaire, J. *Chemosphere* **1982**, *11*, 1179-1188.

[20] Oudjehani, K.; Boule, P. *J. Photochem. Photobiol. A: Chem.* **1992**, *68*, pp. 63.

[21] Lipczynska-Kochany, E.; Bolton, J. R. *J. Photochem. Photibiol. A: Chem.* **1991**, *58*, pp. 315.

[22] Lipczynska-Kochany, E.; Bolton, J. R. *Environ. Sci. Tech.* **1992**, *26*, pp. 259.

[23] Durand, A. Y.; Brattan, D.; Brown, R. G. *Chemosphere* **1992**, *25*, pp. 783.

[24] Mills, A.; Morris, S.; Davies, R. *J. Photochem. Photobiol. A: Chem.* **1993**, *70*, pp. 183.

[25] Martin, S. T.; Lee, A. T.; Hoffmann, M. R. (In Press) **1995**.

[26] Boule, P.; Guyon, C.; LeMaire, J. *Chemosphere* **1982**, *11*, pp. 1179.

[27] Mabey, W. R.; Tse, D.; Baraze, A.; Mill, T. *Chemosphere* **1983**, *12*, pp. 3.

[28] LeMaire, J.; Guth, J. A.; Klais, O.; Leahey, J.; Merz, W.; Philp, J.; Wilmes, R.; Wolff, C. J. M. *Chemosphere* **1985**, *14*, pp. 53.

[29] Crossland, N. O. *Chemosphere* **1990**, *21*, pp. 1489.

[30] Chen, T. H.; Campbell, C.; Fisco, W. J. *Characterization of Pollutants at Holston Army Ammunition Plant.* technical report ARLCD-TR-8103, United States Army ARRADCOM, 1981.

[31] Blystone, P. G.; Johnson, M. D.; Haag, W. R.; Daley, P. F. *Advanced Ultraviolet Flash Lamps for the Destruction of Organic Contaminants in Air.* In: *Emerging Technologies in Hazardous Waste Management III*; Tedder, W.; Pohland, F. G. Eds. American Chemical Society: Washington D.C. 1993; pp. 380.

[32] Gusinow, M. A. *J. Appl. Phys.* **1975**, *46*, pp. 4847.

[33] Wekhof, A. *Rev. Sci. Instrum.* **1992**, *63*, pp. 5565.

[34] Dillert, R.; Brandt, M.; Fornefett, I.; Siebers, U.; Bahnemann, D. *Chemosphere* **1995**, *30,* pp. 2333.

7 Conclusions

7.1 Summary of Results

A two-phase model that describes the Electrohydraulic Discharge process (EHD) has been described. The performance of this model has been evaluated for the Caltech Pulsed Power Facility (CPPF). It was also demonstrated through observations of the degradation of 4 -chlorophenol (4-CP), 3,4 -dichloroaniline (3,4-DCA), and 2,4,6 - trinitrotoluene (TNT) that in its current low repetition mode that the *EHD* process in the CPPF operates primarily as a high intensity *UV* light source.

In agreement with published data [1,2,3], the simulation accurately describes the dynamics of the temperature, pressure, and channel radius of the underwater plasma channel. The model is fast and easy to use since it relies on a set of ordinary differential equations which have been formulated in such a way that the constitutive equations of the plasma can be improved when necessary. The model demonstrates that the temperature and pressure of the plasma channel reaches its maximum within the first quarter cycle of the discharge. When averaged over the whole discharge cycle, the temperature may only reach 10,000 to 15,000 K. However, the instantaneous maximum during the first quarter cycle may reach temperatures in excess of 40,000 K.

The model can be applied with confidence to generate predictions of the energy partition of the underwater plasma channel. In Chapter 5, it was demonstrated that the energy partition, and the pressure and temperature extremes remain unchanged with

decreasing capacitance. Yet, lower capacitances raise the total energy transferred between the capacitor bank and the plasma channel from 45% at 135 μF to 80% at 15 μF. These results suggest that lower capacitances can lead to much higher efficiencies. Unlike the capacitance, the inductance, spark gap length, and initial voltage affect the energy partition, and the temperature and pressure extremes. Out of these parameters, the spark gap length is the most relevant parameter, since it can be readily changed in experiments and has the most pronounced useful effects. In addition to increasing the amount of energy transferred into the plasma channel, a longer spark gap also leads to a decrease in shock wave efficiency and an increase in radiation efficiency. This result implies that longer spark gap lengths will be more useful for photochemical processes.

From the perspective of chemical degradation, the *EHD* discharge operates primarily as a high intensity *UV* light source. In Chapter 6, by observing the degradation kinetics of 4-CP in a 20 mM t-butanol hydroxl scavanger solution, it was demonstrated that cavitation has no discernible effects

The simulation and experiments described in this thesis clearly shows how the EHD process can be optimized. The simulation has demonstrated that the optimal energy transfer efficiency is obtained using lower capacitance discharges. The observations that chemical degradation takes place primarily via photochemical processes and not via shock wave processes, coupled with the prediction that longer spark gap lengths lead to higher radiation efficiencies and lower shock wave efficiencies suggests that longer spark gaps would lead to more efficient chemical degradation. A longer spark gap would also lead to a larger first-order rate constant, since the plasma volume in which direct oxidation of chemical compounds can take place would also increase. The observation that ozone leads to complete degradation of TNT suggests the use of ozone in addition to both smaller capacitances and longer gap lengths.

7.2 Recommendations for Future Research

The current state of the CPPF does not allow for immediate changes of both the capacitance and the spark gap length. The pulsed power system has several design features which stand in the way. The capacitor bank consists of nine 15 μF capacitors in parallel (see Figure 7.1,) leading to a total capacitance of 135 μF. Removal of individual capacitors out of the bank has two prohibitive effects. As a direct consequence of the lower capacitance, the pulse of the discharge would be shortened considerably, incapacitating the switching circuit and leading to impedance mismatches. Furthermore, although the capacitance is additive, the inductance contributed by each capacitor is inversely additive, as illustrated by eq 7.1;

$$L_{Total} = \left(\sum \frac{1}{L}\right)^{-1} = \frac{L}{k}, \qquad 7.1$$

where L is the inductance of each capacitor, and k is the total number of capacitors. Thus, removing capacitors in turn increases the inductance. The results in Chapter 5 show that an increase in inductance does not have significant effects on the radiation efficiency, but will lower the total energy efficiency, shock wave efficiency, maximum temperature, and maximum pressure.

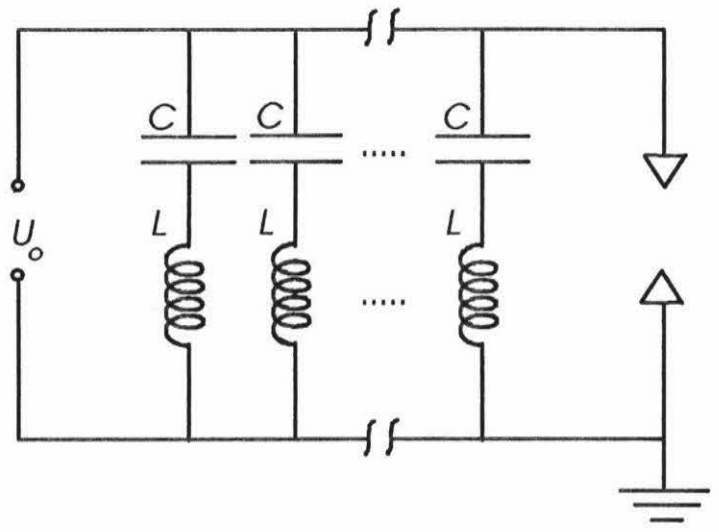

Figure 7.1
Circuit illustrating the capacitor bank for the Caltech Pulsed Power Facility (CPPF) Each capacitor contributes a net inductance of 100 nH.

Lengthening the spark gap length also presents some challenges. At voltages below 100 kV, water acts as an insulator. At these voltages, it is difficult to generate a plasma channel across larger gaps without an initiating wire. One solution is to generate a high-voltage low energy discharge prior to closing the switch on the large discharge gap. Another approach is to generate a large enough air bridge in between the electrodes. In any case, wider spark gap discharges will require some changes in the design of the CPPF.

Lower capacitance discharges also offer another advantage which may lead to higher chemical degradation efficiencies. A smaller capacitance requires less time to recharge, thus allowing faster repetition rates. the observations made in Chapter 6 that cavitation induced chemical degradation does not take place still does not rule out cavitation as a possible contributing factor in degradation via EHD processes. One reason we may not be observing cavitational effects may be due to the rather large time gaps (> 30 seconds) in between pulses. A well-known observation in sonochemistry with pulsed ultrasound is that chemical yield decreases with increasing time spacing of the ultrasound pulses [5]. Apparently, a certain activation time is necessary to generate cavitation bubbles. This fact suggests that in order to expect chemical degradation from EHD produced shock waves, the discharges should be as closely spaced as possible. On the other hand, the activation mechanism in ultrasound is quite different than with shock waves. For example, the concept of rectified diffusion and resonant radius known from sonochemistry [6,7] do not apply in shock waves. Since shock wave induced rarefaction pulses will be of much greater magnitude, we expect to get the necessary growing and collapse of bubbles from just one rarefaction pulse. Thus, activation may not be needed with shock wave irradiation. These issues should be explored experimentally before drawing any conclusions regarding the full potential of the EHD process.

References

[1] Martin, E.A. *J. App. Phys.* **1960**, *31*, 255-265.

[2] Robinson, J. W. *J. Appl. Phys.* **1973**, *44*, pp. 72 .

[3] Ioffe, I. A. , Naugol'nykh, K. A. , and Roi, N. A., *Zh. Prikl. Mekhan. i Tekh. Fiz.* **1964**, *4*, pp.108.

[4] Skvortsov, Y.; V. Komelkov, V.S.; Kuznetov, N. M. *Zhurnal Tekhnicheskoi Fiziki* **1960**, *30,* 1165-1177.

[5] Henglein, A.; Gutiérrez, M. *Int. J. Rad. Biol.* **1986** *50*, pp 527.

[6] Suslick, K.S. (Editor) *Ultrasound: Its Chemical, Physical and Biological Effects*. **1988,** New York, VCH Publishers.

[7] Gavrilov, L. R. In *Physical Principles of Ultrasonic Technology,* Rozenberg, editor, Vol. 2, part VI, **1973,** New York, Plenum Press.

Appendix A: Glossary

In this thesis, unless denoted by an explicit time dependence *(t)*, all symbols that are not denoted by a Latin letter with a subscript, or by a Greek letter with or without a subscript, are time dependent. The following is a glossary of symbols used in this thesis. Some symbols that are used only in a small section of this thesis are not listed here.

$a = a(t)$ = channel radius

a_{max} = maximum radius of the post-discharge gas bubble

E_B = Total energy stored in the capacitor bank

C_b = Capacitance of the capacitor bank

e = elementary charge constant (= $1.602 \cdot 10^{-19}$ *Coulomb*)

f = Fraction of radiation absorbed by fluid surrounding plasma channel

$I = I(t)$ = Electrical current through plasma channel

I_o = Initial current through plasma channel

k = Stephan-Boltzmann Constant $1.38 \cdot 10^{-23}\ J\ K^{-1}$

ℓ = Length of plasma channel = length of underwater spark gap

L_c = Circuit inductance

$M(\overline{y})$ = Time stepping function matrix used by the numerical equation solver

$N = N(t)$ = Total number of particles in the plasma channel

N_o = Total particle density proportionality constant used in Chapter 4

$n = n(t)$ = Number of particles per unit volume in the plasma channel

$P = P(t)$ = Pressure on the surface of the plasma channel

P_a = Ambient pressure of fluid surrounding plasma channel

P_o = Initial pressure on the surface of the plasma channel

Q_o = Linear Power rise coefficient

$q = q(t)$ = Charge stored in the capacitor bank

q_o = Initial charge stored in capacitor bank

$R = R(t)$ = Resistance of the plasma channel

R_o = Initial resistance of the plasma channel

R_c = Resistance of the discharge circuit

$S = S(t)$ = Surface area of the plasma channel

$T = T(t)$ = Temperature of the plasma channel

U_o = Initial voltage across plasma channel

$U(t)$ = Voltage across the capacitor bank

$U_d(t)$ = Voltage across the underwater spark gap

$\mathcal{U}$ = Velocity of individual shock fronts

u = Fluid velocity

$V = V(t)$ = Plasma channel volume

$W = W(t)$ = Internal energy density of the plasma channel

$\overline{\mathbf{y}}$ = Function vector used by the numerical equation solver

α = 3001 bars (Part of the Tate equation of state for water)

β = 3000 bars (Part of the Tate equation of state for water)

ε_o = The permittivity constant (= $8.85 \cdot 10^{-12}$ N/m)

$\varepsilon_{vaporization}$ = Energy/per particle required to vaporize water

μ_o = The permeability constant (= $4\pi \cdot 10^{-7}$ H/m)

γ = proportionality constant for the internal energy (= 1.22)

ρ_o = 1 $kg\ m^{-3}$ Constant for density of water at STP

κ = Thermal particle induction proportionality constant

σ_B = Stephan-Boltzmann constant for a blackbody radiator (= $5.67 \cdot 10^{-8}$ $W/m^2 K^4$)

$\sigma_{cond}(t)$ = Electrical conductivity of plasma channel

$\sigma_{ionize}(t)$ = Particle induction cross-section

ξ = Proportionality constant for the electrical conductivity of the plasma channel

Appendix B: The Pressure Relation

The pressure of the plasma channel can be related back to the channel radius *a(t)* by using the equations of fluid mechanics. The exact approach is to use the Kirkwood-Bethe equation for the channel expansion [1];

$$a\ddot{a}\left(1-\frac{\dot{a}}{c}\right)+\frac{3}{2}\left(1-\frac{\dot{a}}{c}\right)\dot{a}^2=\left(1+\frac{\dot{a}}{c}\right)H+\frac{a}{c}\left(1-\frac{\dot{a}}{c}\right)\dot{H}, \qquad \text{B-1}$$

where $c = c(\rho)$ is the speed of sound as a function of density, and H is the enthalpy of the bubble, which is given by

$$H=\int_{P_o}^{P}\frac{dP}{\rho}=\frac{c_o^2}{k-1}\left[\left(\frac{P+\beta}{\alpha}\right)^k-1\right], \qquad \text{B-2}$$

where c_o is the speed of sound at $\rho_0 = 1g\ cm^{-3}$. Equation B-2 follows from the equation of state for water: [2]

$$P=\alpha\left(\frac{\rho}{\rho_o}\right)^k-\beta, \qquad \text{B-3}$$

where $\alpha = 3001$ *bars*, $\beta = 3000$ *bars*, and $\rho_0 = 1g\ cm^{-3}$. These equations give very precise results, but introduce a high degree of non-linearity into the simulation of the underwater plamsa channel.

A much simpler relation between the pressure on the surface of the channel and the channel wall velocity can be derived from the Rankine-Hugoniot relations for a shock front [2]. First, let us consider a piston which pushes water as follows;

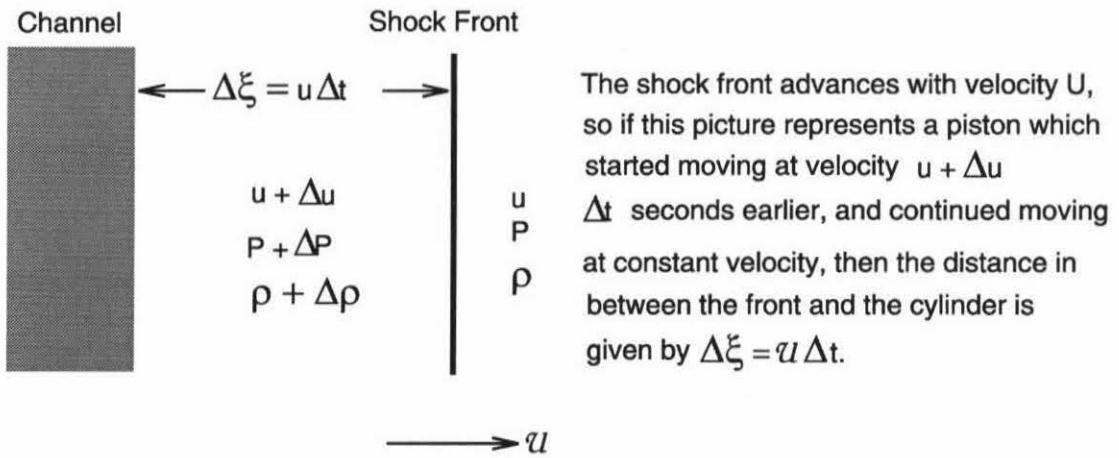

Figure B-1

The shock front of velocity $\mathcal{U}$ can be considered as a mathematical discontinuity in ρ, P and u. Generally, $\mathcal{U} >> u$, so fluid ahead of the front continually enters the front where its pressure, density and velocity changes. Conservation of mass at the front requires the following to be true:

$$\rho(\mathcal{U} - u) = (\rho + \Delta\rho)[\mathcal{U} - (u + \Delta u)]. \qquad \text{B-4}$$

Conservation of momentum at the front gives the following equation:

$$(P + \Delta P) - P = \rho(\mathcal{U} - u)(u + \Delta u - u). \qquad \text{B-5}$$

The above two relations are more generally known as the Rankine-Hugoniot relations. In addition, we use the standard equation of state for water;

$$P = \alpha\left(\frac{\rho}{\rho_o}\right)^7 - \beta . \qquad \text{B-6}$$

where α, β, and ρ_0 are given as above. Equation B-6 does not include a temperature dependance because it is insignificant for the regime of shock waves we are interested in. The above equations are solved to find a relation between the channel wall velocity u and the pressure P.

Consider a planar piston initially at rest in water, and then allow the piston to move abruptly with a constant velocity. At that instant, the pressure on the piston surface will take a value P_O as given by the above relations with $u = 0$ and Δu = piston velocity. As the piston continues moving with the same velocity, the step function in pressure created when the piston started moving will propagate with velocity $\mathcal{U}$ away from the piston into the surrounding water. A lengthening column of compressed water with constant pressure P_O will build up in front of the piston as long as the piston keeps moving at constant velocity. Behind the shock front, the fluid velocity will be Δu equal to the piston velocity, and ahead of the front, the velocity is zero. Then, if the piston abruptly increases it's velocity to a new value, a second shock front will advance into the previously compressed region. The discontinuous increase in pressure is again given by the Rankine-Hugoniot equations, but as long as the piston continues to move at this new velocity, the pressure on its surface remains constant. Thus, whenever the piston changes its velocity, a shock front leaves and advances into the water.

Now, consider a piston which originates a continuous succession of shock fronts as its velocity varies in a continuous manner.

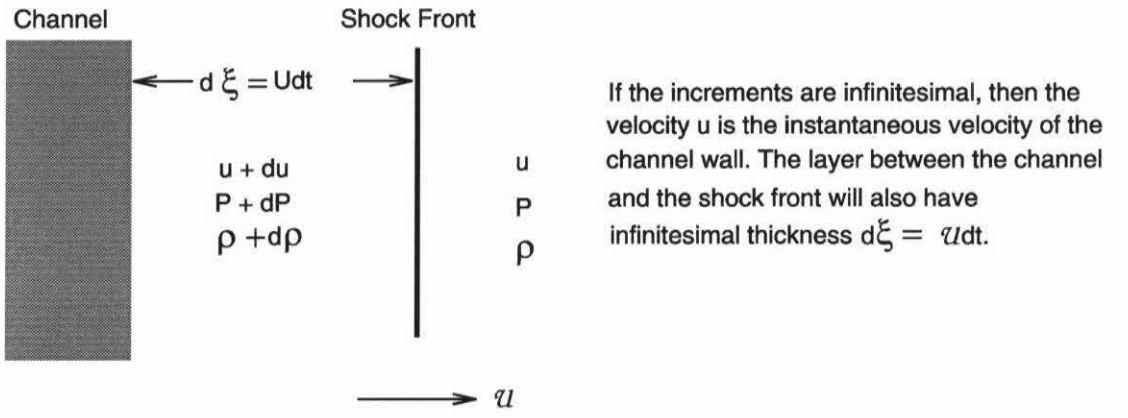

Figure B-2

The same relations as above will hold, with $\Delta \to d$ so that we have:

$$\rho(\mathcal{U} - u) = (\rho + d\rho)[\mathcal{U} - (u + du)] \qquad \text{B-7}$$

and

$$dP = \rho(\mathcal{U} - u)du. \qquad \text{B-8}$$

From these relations and the equation of state, we find

$$\frac{dP}{du} = \frac{\sqrt{7\rho_o}}{\alpha^{1/14}}(P+\beta)^{4/7}. \qquad \text{B-9}$$

This equation can be integrated by separation of variables; use the boundary conditions $P \to 1\ bar \cong 0$ as $u \to 0$ to get

$$(P+\beta)^{3/7} = \left(\frac{3\sqrt{\rho_o}}{\sqrt{7}\alpha^{1/14}}\right)u + \beta^{3/7}. \qquad \text{B-10}$$

We now have a relation between the pressure on the surface of the channel and its expansion velocity.

References

[1] Cole, R. H. *Underwater Explosions* Princeton University press, Princeton, New Jeresey, 1948

[2] Courant, R.; Friedrichs, K. O. *Supersonic Flow and Shock Waves* Springer-Verlag New York, 1977

Appendix C: Calculation of the Internal Energy

A relationship between the internal energy of the plasma and the pressure of the channel can be obtained. One of the tools needed to calculate the internal energy of the plasma is the Saha ionization equation [1]. It has been noted that spectra taken of light from the surface layers of the sun showed lines corresponding to ions of a higher level of ionization than the lines which appeared in spectra of light from deeper-lying layers [2]. This phenomenon suggests that the outer layers of the sun are hotter than the inner layers, provided that one assumes that a Boltzmann relationship describes the equilibrium population of ionized levels, as if they were exited states of the atom. But the picture of an astral body being hotter on the outside than on the inside was inconsistent with the fundamental concepts of stellar dynamics. In order to resolve this conflict, it was concluded that pressure as well as temperature must control the levels of ionization of a gas, whereas the exited levels are affected only by temperature.

The physical reason for this difference can be explained as follows. In both ionization and excitation processes, the elevation of a gas particle to a higher energy level may be brought about by similar physical events. However, the decay back to lower levels is fundamentally very different in the two cases. For excitation decay, a second particle, an electron, is not required. Thus an exited atom, whether in a dense gas or isolated in empty space, would have the same probability of decaying regardless of the presence of other particles. (Here, we neglect the distortion of the atom which may take place in a dense gas.) However, for ionization decay, an electron is required. An ionized atom, isolated in free space, would never decay, whereas it would return to its lower level rapidly if immersed in a cloud of electrons. The presence of other particles strongly affects the probability of decay. The equilibrium population of ionized levels therefore depends on gas pressure as well as temperature.

Taking into account the difference in decay processes, we can derive a relation for the ionized levels based on the Boltzann relation. The only two assumptions which are necessary are that the gas must be in thermal equilibrium and that the effects produced by inter particle fields are negligible. We will restrict ourselves to the case of a neutral atom and its first stage of ionization.

The following derivation follows directly that of reference [1]. Consider the energy level diagram of an atom as shown below in figure C-1. We will relate the population of electrons in the energy gap dE of the continuum to the population of electrons in the bound (discrete) states of the atom corresponding to ground state energy. We take the ground state energy to be the energy reference level. We start off with the generalization of the Boltzmann law;

$$\frac{dN_o^+(v)}{N_o} = \frac{dg}{g_o}\exp\left[-\frac{E}{kT}\right], \qquad \text{C-1}$$

where $dN_o^+(v)$ is the differential number of ions in the ground level with the free electron in velocity range v to $v+dv$, and N_O is the number of atoms in the ground level. g_O is the statistical weight of the ground state, and the differential statistical weight dg assigned to the energy gap dE is given as $dg = g_o^+ dg_e$ where g_o^+ is the statistical weight of the ion in its ground state, and dg_e, the differential electron statistical weight is given by

$$dg_e = \frac{2}{h^3} d^3\bar{x} d^3\bar{p}, \qquad \text{C-2}$$

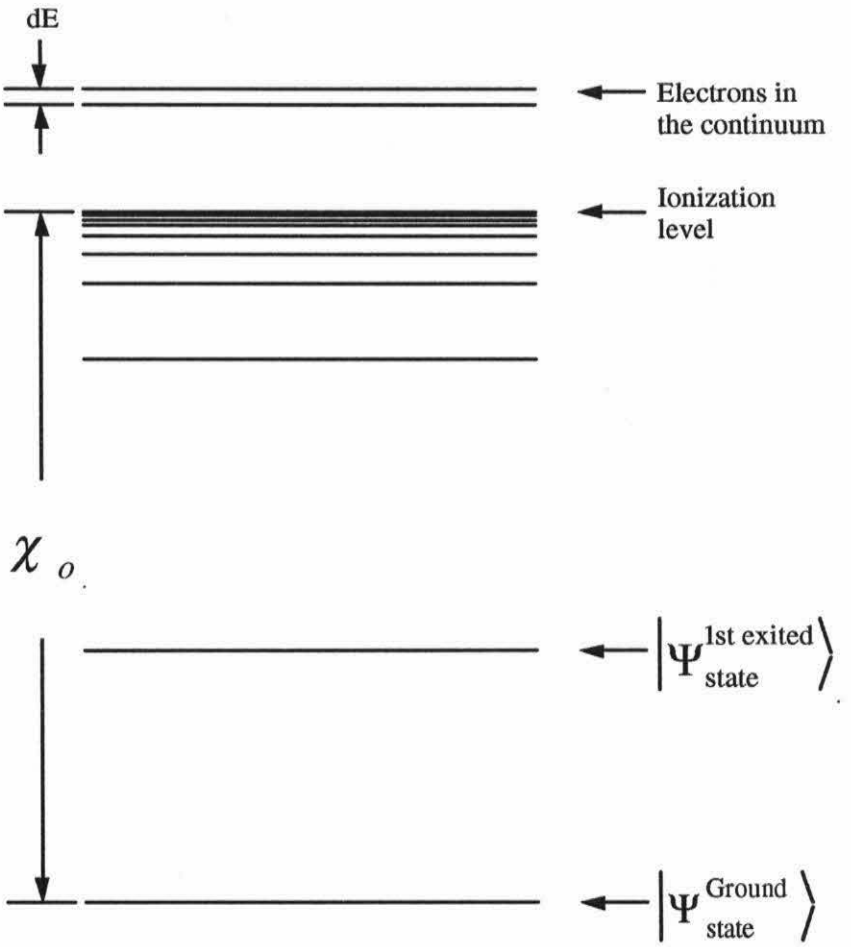

Figure C-1

Energy level diagram of an atom: χ_o corresponds to the energy required to ionize the atom from its ground state. The electrons in the band with energy between E and $E+dE$ are unbound. For oxygen, χ_o = 13.355 *eV*, and for yydrogen, χ_o = 13.53 *eV*.

where the factor of $h^3/2$ follows from dividing six-dimensional phase space into units of volume h^3 which can each contain at most two electrons, one for each spin state. The justification of this quantum statistical procedure is that the assignment of the weights leads to a compatibility, or consistency, between quantum and classical mechanics. It is a form of the correspondence principle.

The configuration space volume element satisfies $d^3\bar{x} = 1/n_e$, where n_e = electron density, since we are applying Bolzmann's law to a region containing one electron. Since the electrons have isotropic velocity distribution, we can write

$$d^3\bar{p} = 4\pi m_e^3 v^2 dv \ . \qquad \text{C-3}$$

Thus, equation C-1 becomes

$$\frac{dN_o^+(v)}{N_o} = \frac{8\pi m_e^3}{h^3}\frac{g_o^+}{n_e g_o}\exp\left[-\frac{E}{kT}\right]v^2 dv. \qquad \text{C-4}$$

To find the total number of ions in the ground level with the electron unbound, we integrate over all velocities. To do that, we must introduce the relation between E and v for the electron;

$$E = \chi_o + \frac{1}{2}m_e v^2. \qquad \text{C-5}$$

By introducing this relation, we are implicitly assuming that the electrons do not interact with each other. Then, substituting C-5 into C-4, and integrating over v with the substitution $x \equiv \sqrt{m_e / 2kT}v$, we find

$$\frac{N_o^+ n_e}{N_o} = \frac{8\pi m_e^3}{h^3}\frac{g_o^+}{g_o} e^{-\frac{\chi_o}{kT}} \left(\frac{2kT}{m_e}\right)^{3/2} \int_0^\infty e^{-x^2} x^2 dx. \qquad \text{C-6}$$

The integral has the value $\sqrt{\pi}/4$. Thus we obtain

$$\frac{n_o^+ n_e}{n_o} = \left(\frac{2\pi m_e kT}{h^2}\right)^{3/2} \frac{2g_o^+}{g_o} e^{-\frac{\chi_o}{kT}}, \qquad \text{C-7}$$

where we have substituted $n = N/V$ and $n_o^+ = N_o^+/V$. Then, to find the number of ions or atoms in any state, not just the ground state, we use the following Boltzmann distributions:

$$\frac{n_o}{n} = \frac{g_o}{B(T)} e^{-0/kT}, \text{ and } \frac{n_o^+}{n^+} = \frac{g_o^+}{B^+(T)} e^{-0/kT}, \qquad \text{C-8}$$

where $B(T)$ and $B^+(T)$ are the partition functions for the atom and ion, respectively. Substituting C-8 into C-7 then leads to Saha's equation [2]

$$\frac{n^+ n_e}{n} = \frac{2B^+(T)}{B(T)} \left(\frac{2\pi m_e kT}{h^2}\right)^{3/2} e^{-\frac{\chi_o}{kT}}. \qquad \text{C-9}$$

Note that Saha's equation can be applied to successive levels of ionization by repeating the above derivation for an atom in its *j*th level of ionization, being ionized to its *j+1*st level of ionization. The general form of Saha's equation then is

$$\frac{n_{j+1} n_e}{n_j} = \frac{2B_{j+1}(T)}{B_j(T)} \left(\frac{2\pi m_e kT}{h^2}\right)^{3/2} e^{-\frac{\chi_{j\to j+1}}{kT}}. \qquad \text{C-10}$$

Even though the Coulomb interactions between particles in the plasma in an underwater discharge cannot be neglected (See chapter 2), we can still justify the use of the Saha ionization equation based on the concept of the Debye shielding distances. In the plasma of the underwater spark, the Debye length is less than the average particle spacing, hence the effective field of an ion does not extend greatly beyond its nearest neighbors. This leads to the conclusion that the inter particle forces are not spatially extensive enough to modify the form of the Saha equation.

One of the challenges in working with the Saha ionization equation is in evaluating the partition functions. In general,

$$B(T) = \sum_i g_i e^{-E_i/kT}, \qquad \text{C-11}$$

where E_i are the energies of the levels above the ground state. Unfortunately, the partition function for an atom or ion is not convergent; in general the g_i factors in C-11 increase as the principal quantum number increases, but the E_i's are bounded by the ionization potential of the atom or ion. One method to determine how many levels should actually be included is Urey and Fermi's method of excluded volumes [3]. In this method, it is assumed that the atom or ion can be exited to a level only as high as that which will make its volume equal to the average volume of space available to the atom or ion. Excitation to a higher level is thus excluded, since the excitation electron will then more appropriately belong to a nearby atom or ion. We will generally only use equation C-9 since at any one time, atoms in only two adjacent levels will be present in appreciable numbers [4]. Most of the calculations must be done numerically, in an iterative procedure.

The outline of the calculation for the internal energy density W of the plasma during the discharge is as follows; we assume an ideal gas which is fully dissociated and partially ionized. More precisely, we include singly ionized and neutral oxygen and hydrogen atoms. Let n_H and n_O be equal to be the densities of neutral hydrogen and oxygen, respectively, let n_{HI} and n_{OI} be equal to the densities of singly ionized hydrogen and oxygen, respectively, and let n_e correspond to the electron density. The internal energy density W is then given by

$$W = \tfrac{3}{2}nkT + n_H\langle E_H\rangle + n_o\langle E_o\rangle + n_{HI}I_H + n_{OI}I_o + \tfrac{1}{3}(n-n_e)D, \qquad \text{C-12}$$

where $\langle E_H\rangle$ and $\langle E_O\rangle$ are the average energy of the neutral hydrogen and oxygen atoms, respectively, calculated using the Boltzman relation

$$n_{HExited} = n_H \frac{g_{Exited}}{B(T)} e^{-\frac{E_{Exited}}{kT}}. \qquad \text{C-13}$$

D is the dissociation energy associated with $H_2O \rightarrow H + 2O$, I_H and I_O are the respective ionization energies of hydrogen and oxygen. All we need now are all the particle numbers. These are determined as outlined below. First, we have the particle balance;

$$n_H + n_{HI} + n_O + n_{OI} + n_e = n, \qquad \text{C-14}$$

where the total number of particles is given by the ideal gas law,

$$P = nkT, \qquad \text{C-15}$$

where we take the temperature and pressure as given parameters. We can get another relation from the stoichiometry of water dissociation:

$$n_H + n_{HI} = 2(n_O + n_{OI}). \qquad \text{C-16}$$

We also have a relation from conservation of charge; for every ionized atom, we get one electron.

$$n_{HI} + n_{OI} = n_e. \qquad \text{C-17}$$

Finally, we get two additional relations from the Saha ionization equation;

$$n_{HI} n_e = n_H S_H \qquad \text{C-18a}$$

$$n_{OI} n_e = n_O S_O, \qquad \text{C-18b}$$

where the Saha ionization factors are given by

$$S = \frac{2B_I(T)}{B(T)} \left(\frac{2\pi m_e k}{h^2} \right)^{\frac{3}{2}} T^{\frac{3}{2}} e^{-\frac{11{,}600V}{T}} \qquad \text{C-18c}$$

with $B(T)$, $B_I(T)$ being the partition functions for the neutral and ionized atoms, respectively, V is the ionization potential, and m_e is the mass of the electron. Of course, atoms will also be exited, so that we need to include the additional Boltzmann relation

$$n_{HExited} = n_H \frac{g_{Exited}}{B(T)} e^{-\frac{E_{Exited}}{kT}}. \qquad \text{C-19}$$

Finally, the above relations can be used to calculate the internal energy using equation C-12. Although the results cannot be expressed analytically, numerical calculations show that the resulting internal energy is proportional to the pressure and almost completely independent of temperature [4,5]. Thus, we can write

$$W = \frac{1}{\gamma - 1} P, \qquad \text{C-20}$$

where γ takes on the value 1.22 [4,5]. This relation can then be applied to the energy balance equation for the underwater plasma.

References

[1] Rybicki, G. B.; Lightman, A. P. *Radiatove Processes in Astrophysics* Wiley Interscience, New York, 1979

[2] Saha, M. N. *London Philosophical Magazine* **1920**, *40*, pp. 472

[3] Fowler, R. H. *Statistical Mechanics; the Theory of the Properties of Matter in Equilibrium*, University Press, 2nd ed. Cambridge [Eng.] 1966

[4] Martin, E.A. *J. App. Phys.* **1960,** *31* 255-265

[5] Ioffe, A. I.; Naugol'nykh, K.A.; Roi, N.A. *Zh. Prikl. Mekhan. i Tekh. Fiz.*, **1964**, *4*, pp.108

Appendix D: Chemical Effects of Focused Shock Waves in Water.

D.1 Introduction and Motivation

This appendix describes a preliminary study focused on exploring the potential for inducing chemical degradation by using Electrohydraulic Discharge (EHD) generated shock waves. This study was done using elliptical reactor geometries such as those typical of devices employed in lithotripsy [1]. This work is included as an appendix because most of the results have not been verified for reproducibility due to our limited access to the experimental apparatus used.

All of this preliminary work was done in collaboration with Dr. Sturtevant in Aeronautics. His research is directed towards understanding the linkage between mechanical effects of focused shock waves and medical injury. He has kindly agreed to give us access to his lithotriptor to run some simple chemical degradation experiments. We took advantage of this opportunity to examine the effects of focused shock waves on solutions of potassium iodide (KI).

D.2 Background

Shock waves can induce chemical changes in aqueous solutions by two principal mechanisms: changes of state of the liquid at the shock front, and shock wave induced cavitation. Since chemical effects associated with shock wave induced changes of state occur only at pressure amplitudes of at least 10^5 *bars,* our preliminary research was focused primarily on the chemical changes brought about by shock wave induced cavitation. Our main focus will be to study the shock wave induced chemical changes

on iodide, which serves as a dosimeter for cavitational effects. From the resulting I^- oxidation, we were able to draw conclusions regarding the physical nature of the shock wave induced cavitation.

Elliptical reflectors provide a controlled and well-known shock wave environment. Hence, these reflector geometries provide an ideal setting for the study of shock wave induced cavitation and its associated chemical degradation. When a spherical underwater shock wave is generated at one of the two foci of an elliptical cavity, the reflected shock wave focuses at the second focus point [2,3]. This technique is widely applied in lithotripsy with a half ellipsoidal shape. The procedure is shown in Figure D.1. The shock wave is generated at the focal point f_1 of a rotationally symmetrical semi-ellipsoid. The shock wave then spreads in a circular form until it reaches the ellipsoid wall. Each point of the ellipsoid wall becomes a generating point for a new circular wave. The envelope of these elementary waves forms the reflected shock wave. These wave fronts envelopes are sketched as they appear at different times. With increasing time, the waves move towards the right until they convene at the second focal point f_2. The focusing effect of the ellipsoid leads to clearly definable transmission time because all the shock waves which are reflected from the ellipsoid wall convene at the objective focal point.

The geometrical approximation of the shock wave focusing mechanism described above is valid for weak shock waves in the acoustic limit. The area of high pressure can be treated more or less as a point. As the shock waves generated at f_1 become stronger, the area of high pressure becomes larger and larger, and since the focusing mechanism is highly non-linear, the ratio of high pressure amplitude at focus P_f to generated shock wave amplitude P_g decreases. At the same time, the optics of focused shock waves are very sensitive to the nature of the generated shock wave. The shock

wave source at f_1 must be a pure point. Any deviations from a point source will strongly affect the area of high pressure at the focus f_2. Since the shock wave is generated by a cylindrical plasma channel, the point source approximation will only be accurate for small spark lengths ℓ.

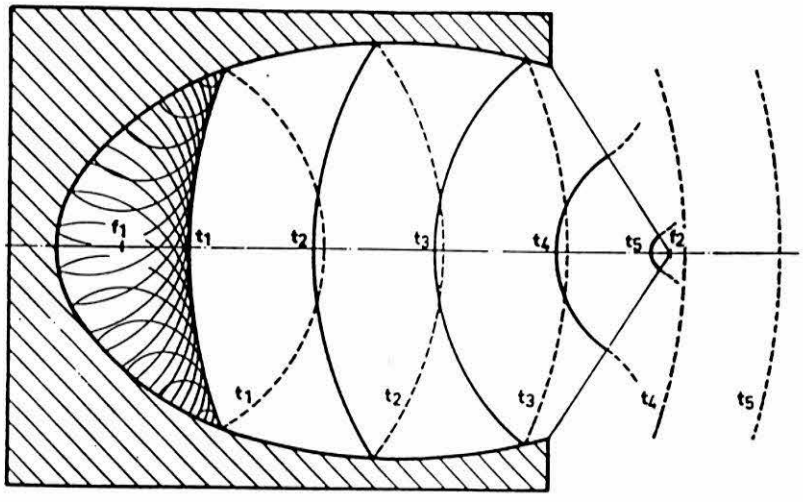

Figure D.1

Diagram illustrating the shock wave focusing mechanism. A shock wave is generated at the focal point f_1 of a rotationally symmetrical semi-ellipsoid. the shock wave then spreads in a circular form until it reaches the ellipsoid wall. Each point of the ellipsoid wall becomes a generating point for a new circular wave. The envelope of these elementary waves forms the reflected shock wave. These wave fronts envelopes are sketched as they appear at different times. With increasing time, the waves move towards the right until they convene at the second focal point f_2.

D.3 Experimental Procedure

We exposed samples in various locations in the elliptical reactor illustrated by Figure D.2. The KI samples were kept in polyethylene bottles to prevent the samples from coming into direct contact with the discharge. We also filled the elliptical reactor with a KI solution in order to explore some of the effects of direct contact with the discharge, including radiation, shock waves, hydrated electrons, and other radicals.

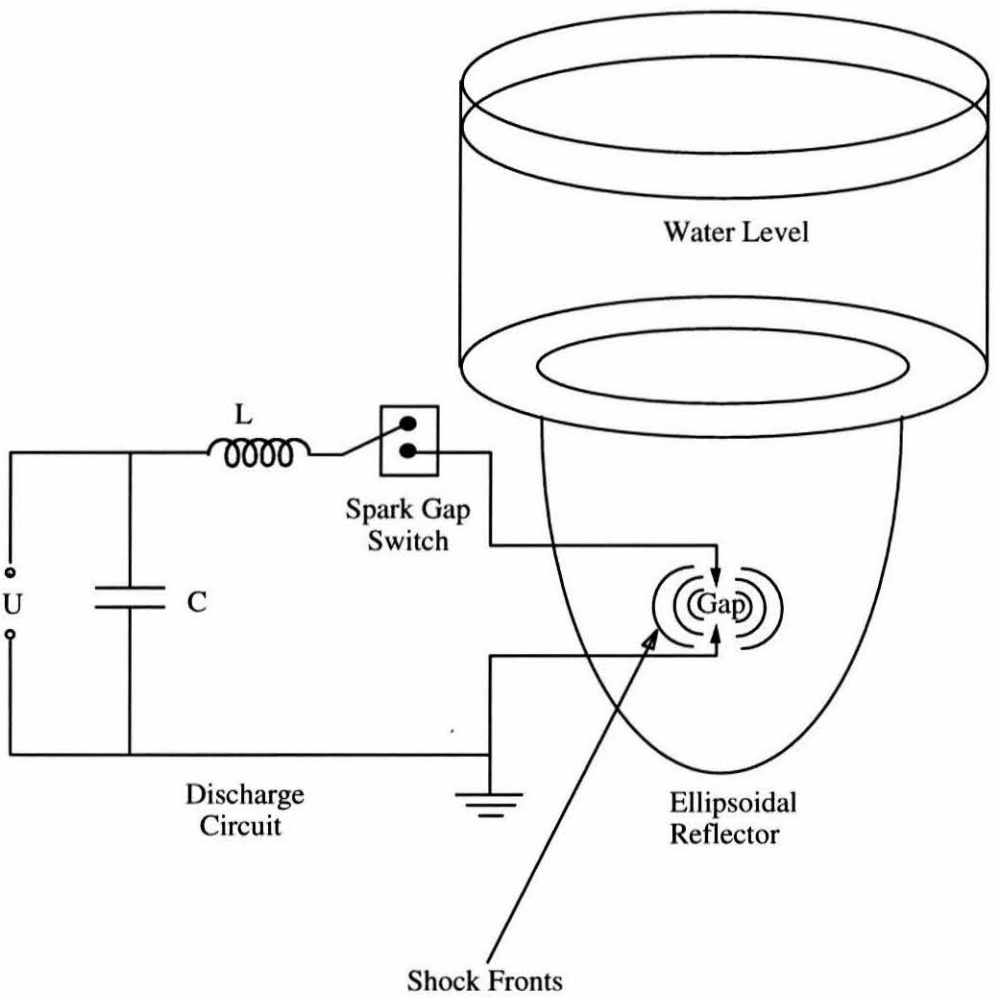

Figure D.2
Diagram illustrating the experimental setup for an EHD process involving an elliptical reflector geometry.

Figure D.3 shows a picture of the lithotriptor apparatus in Dr. Sturtevant's laboratory. On the left are two digital oscilloscopes and the water pump system with associated gauges. The pump serves to fill and empty the ellipsoid bath. On the right is a large cylindrical vessel which contains the ellipsoid and the discharge electrodes. The casing underneath the tub contains the electronics for the discharge. Figure D.4 shows the general outline of the lithotriptor bath. Shock waves are generated at the discharge f_1 and are reflected from the ellipsoid to the focus f_2. The geometry of the ellipsoid is shown in figure D.5. The dimensions of the brass semi-ellipsoid are a = 14 *cm*, b = 7.98 *cm*, and h = 12.497 cm. These dimensions are the same as the ellipsoid in the Dornier HM3 lithotriptor [1].

The electronic circuit is shown in Figure D.6 An EG&G 11A trigger circuit triggers an EG&G GP-12B gas-filled thyatron spark gap to close. A capacitor with C_b=0.337 μF is charged up to a voltage of U_o. The stored energy is given by

$$E_{capacitor} = \tfrac{1}{2} C_b U_o^2. \qquad \text{D.1}$$

This stored energy is then discharged into the underwater spark gap. However, the actual amount of energy E_d transferred into the discharge is given by [4]

$$E_d = \frac{R}{R + R_c}, \qquad \text{D.2}$$

where R is the average resistance of the gap, and R_c is the resistance of the circuit. For a plasma channel generated during a 1-2 joule discharge, the gap resistance can be estimated to be around 5×10^{-3} Ω per *mm* of gap length. Under ideal conditions, the circuit resistance should be smaller than the gap resistance. In this setup, the capacitor

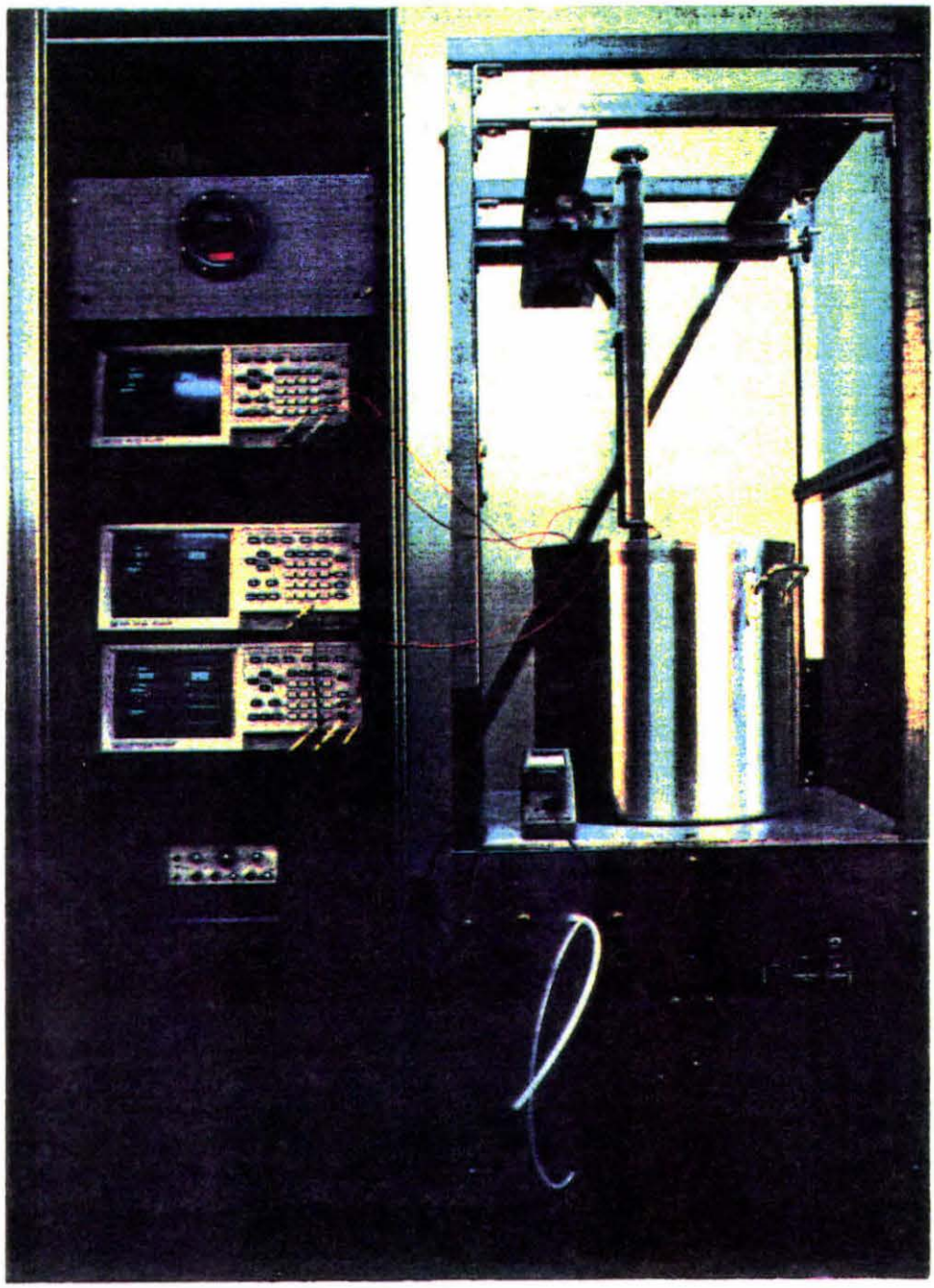

Figure 5.1

Research lithotriptor. Right: bottom, power supply; center, bath; top, 3 degrees of freedom traversing mechanism. Left: center, digital oscilloscopes (6 channels); top, vacuum controls.

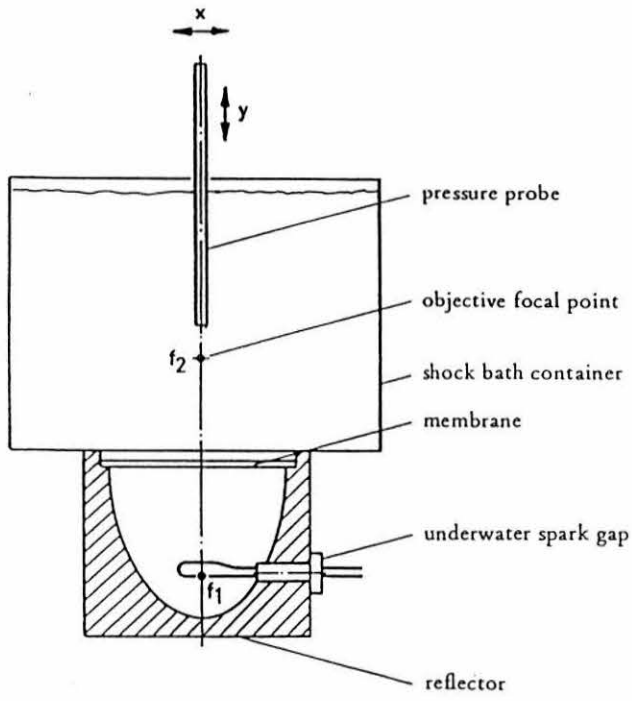

Figure D.4
Schematic diagram of the spark-gap lithotriptor system used in our preliminary studies .

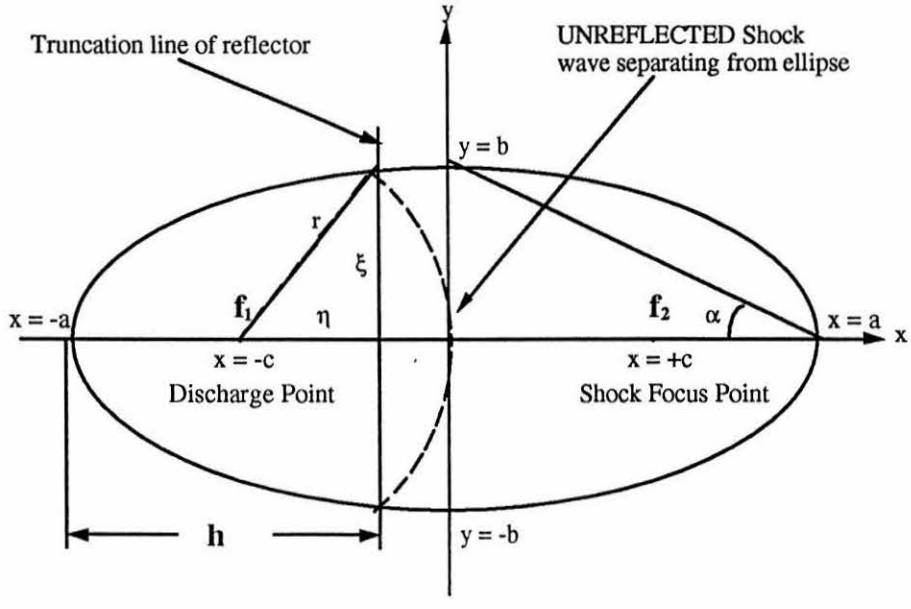

Figure D.5
Schematic outline of the elliptical reflection geometry of the lithotriptor experimental apparatus.

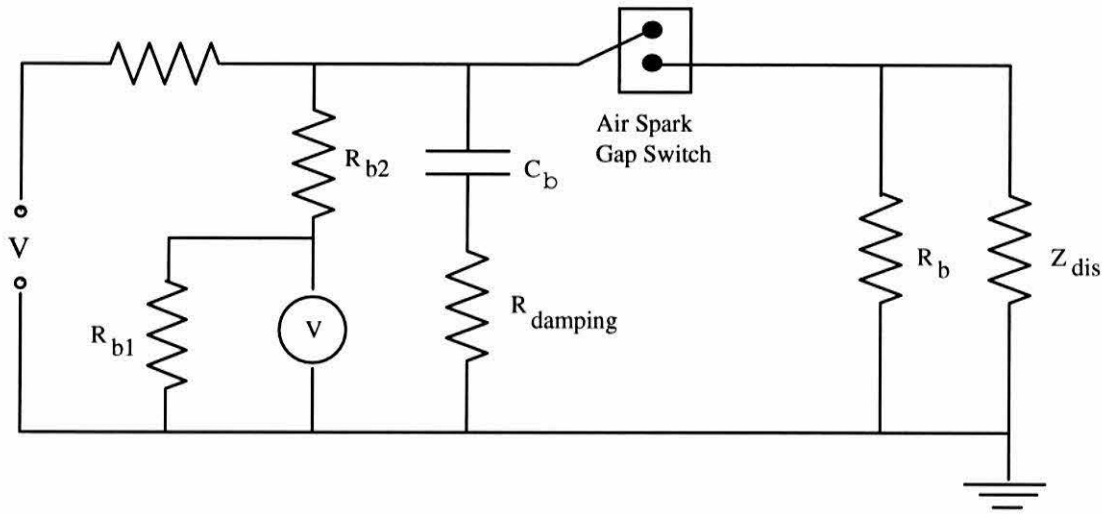

Figure D.6
Circuit diagram of the Discharge Electronics. R_b is a resistor which allows bleeding after discharges for safety reasons. R_{b1} and R_{b2} comprise a voltage divider to measure the charging voltage. $R_{damping}$ is a damping resistor to keep the discharge form ringing.

is only rated for 30 *kV*. Thus, as shown in Figure D.5, the discharge was damped with a 1 Ω resistor ($R_{damping}$) to prevent ringing with peak-to-peak voltages exceeding the capacitor rating. Thus, $R_c = R_{damping} = 1\Omega$. As a consequence, the net energy discharged per pulse was very small. (e.g. eq. D.2.)

All discharges were performed with a charging voltage U_o = 18 *kV*. At this voltage, the energy stored in the capacitor for each pulse was 54.5 *joules*. However, the actual energy discharged, as given by equation D.2, was only 0.5 joules per discharge. Adding the fact that the circuit was not optimized for shock wave production efficiency, we assumed that at most only 2% of the energy originally in the capacitor bank was actually converted into shock waves. Figure D.7 shows a current vs. time trace of the discharge, as measured with a Regowski coil.

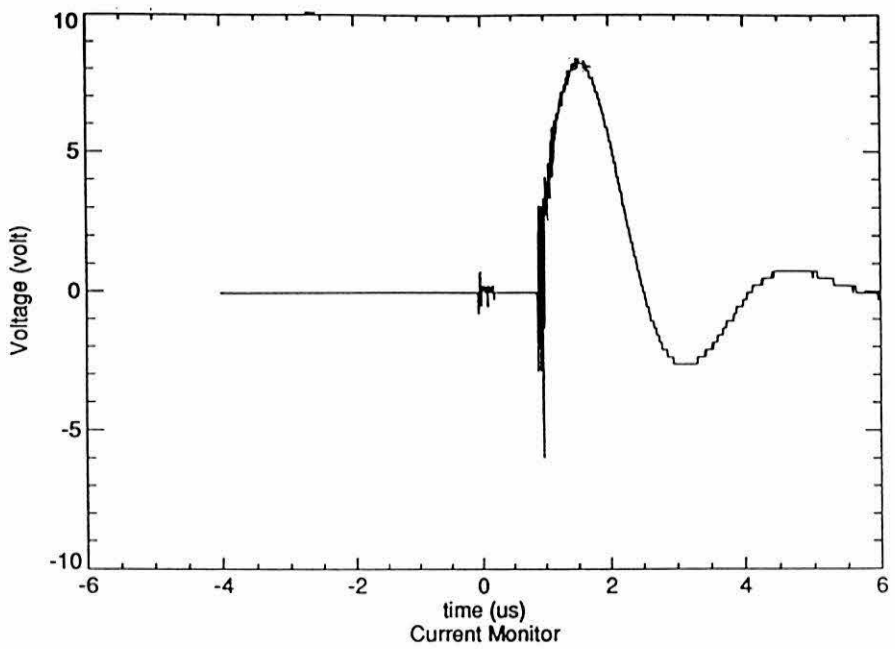

Figure D.7
Oscilloscope traces of the Gap Current During a U_0 = 10 volt discharge.

The amount of time corresponding to the discharge is approximately 5 μs.

The primary aim of the experiments was to follow the oxidation of I^- under various circumstances by measuring the production of triiodide ions (I_3^-) produced. The basic assumption is that OH radicals formed during the discharge lead to the production of iodine (I_2), (as shown in Reaction D.3) which then combines with another iodide ion to form a triiodide ion via the equilibrium reaction D.4:

$$2H + 3I^- + 2 \cdot OH \rightarrow I_2 + 2H_2O \qquad \text{D.3}$$

$$I_2 + I^- \longleftrightarrow I_3^- \,. \qquad \text{D.4}$$

An HP 8450 spectrophotometer was used to measure the concentration of tri-iodide present after exposure to the discharges. Triiodide has an extinction coefficient of 26,400 $M^{-1}cm^{-1}$ [5] at 352 nm. The spectrophotometer is capable of performing seven measurements in one second for one sample, and immediately calculates the standard deviation of the result. The resolution is typically on the order of 2 nm.

D.4 Results

Four kinds of polyethylene bottles where used, each having a volume of 15 *ml*: amber, and clear high density polyethylene, and amber, and clear low density polyethylene. The results are summarized in Table E1. First, we tested to see if we can measure any overall degradation. We placed low density polyethylene bottles both at the focus and just above the discharge. Because I^- is also sensitive to photo-oxidation, there was a possibility that the higher yield for samples placed just above the discharge was due to light emission from the discharge. We confirmed this result by using both light and amber polyethylene bottles. We also noticed that there was a I_3^- concentration change dependent on polyethylene density. But again, this difference was attributed to radiation. We examined the transmission of the two types of polyethylene in the UV range of the electromagnetic spectrum. The results are shown in Figure D.8. This figure explains the increased production of I_3^- in low density polyethylene in terms of an increased transmission coefficient.

From that point on, we used amber polyethylene bottles. The UV transmission coefficient for these bottles may be different; the low density bottle was not available in the amber version, so a low-density bottle was painted with an amber color. The results show that there is indeed a difference at the focus based on the density of the polyethylene, but this difference is not significant enough to lead to any conclusions.

Low Density Polyethylene Bottles

Focus	$A=9.323\times10^{-3}$	C=0.353	G=0.0026
Above gap	$A=4.298\times10^{-2}$	C=1.628	G=0.0118
Sonifier	*$A=2.046\times10^{-2}$*	*(C=0.775)*	*G=0.00027*
(23 W/60 secs)			

Different Bottles Above Spark Discharge

Amber HD	$A=1.663\times10^{-2}$	C=0.630	G=0.0046
Clear HD	$A=1.782\times10^{-2}$	C=0.675	G=0.0049
Clear LD	$A=2.864\times10^{-2}$	C=1.085	G=0.0079

HD vs LD Dark Bottles at Focus

HD	$A=4.580\times10^{-3}$	C=0.017	G=0.00013
LD	$A=9.310\times10^{-3}$	C=0.035	G=0.00026

where we irradiated 15 ml bottles of 0.1 M KI solutions in Millipore purified water of resistivity $<10^{-17}\ \Omega^{-1}cm^{-1}$ with 40 discharges of 0.5 Joules each.

A is the absorbance at 352 nm
C is in μM of I_3^- (C=A/2.6400x10^{-2} μM)
G is in I_3^- molecules/100eV of deposited energy ($G = 9.64\frac{CV}{NE}$)

Useful Acoustic Impedances:

Distilled Water	$Z=1.49\times10^6$ Kg/m^{2}s
Sea Water	$Z=1.57\times10^6$ Kg/m^{2}s
Polyethylene	$Z=1.76\times10^6$ Kg/m^{2}s

Table D.1

Results obtained for various 15 ml bottle types. (Clear Low Density: Nalgene 2003, Clear High Density: Nalgene 2002, Amber High Density: Nalgene 2004, available from VWR)

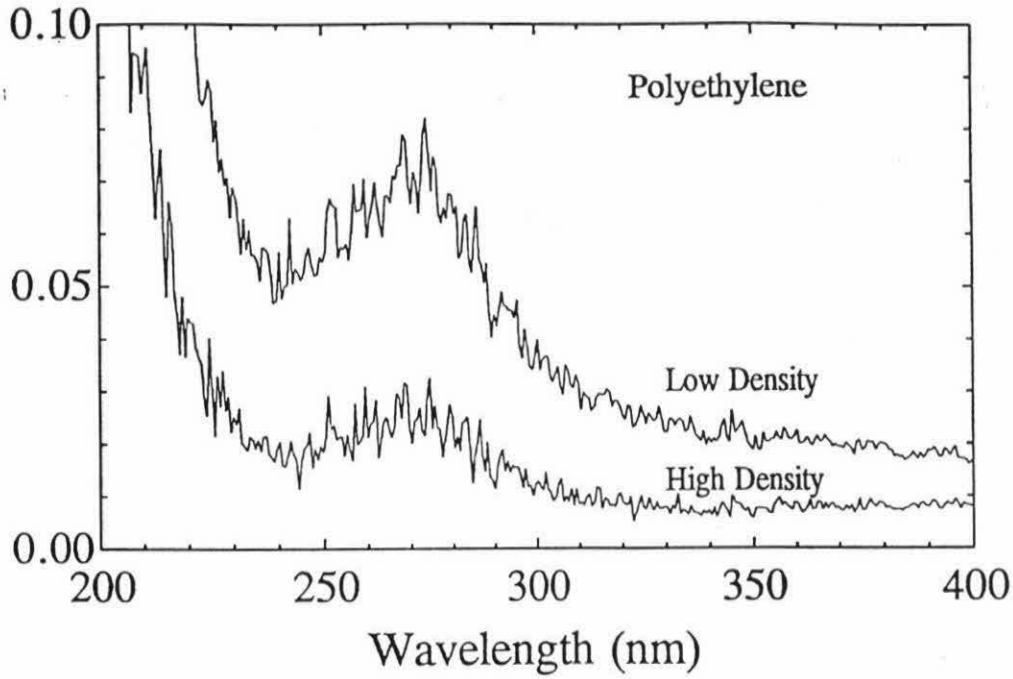

Figure D.8
Transmission Coefficient of Low Density vs. High Density Polyethylene. Courtesy of George Rossman, Geology

The second set of experiments consisted of eliminating the containers all together and replacing the water solution in the ellipsoid by a 0.1 *M* solution of I^-. Thus, the solution experiences the full effects of the discharge, including the underwater plasma, the electromagnetic radiation, the post-discharge bubble and the shock waves. We exposed the solution to subsequent discharges, removing a few mL of solution at each increment of 30 discharges. A curve of concentration versus discharge number is given in Figure D.9.

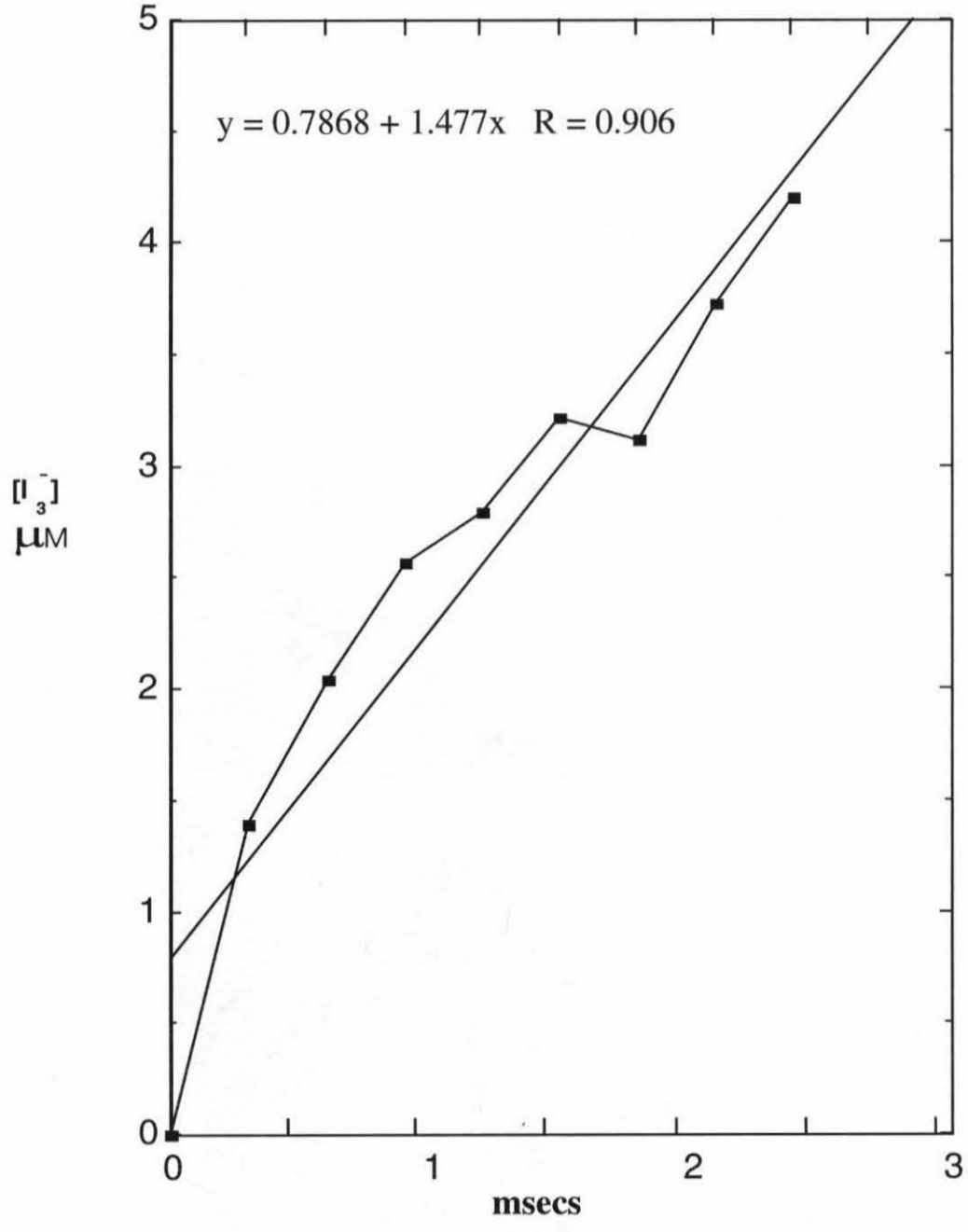

Figure D.9

Production of I_3^- as a function of discharges. The kinetics scale was estimated on the basis of Equation D.7, which states that each discharge has a duration of 5 μs.

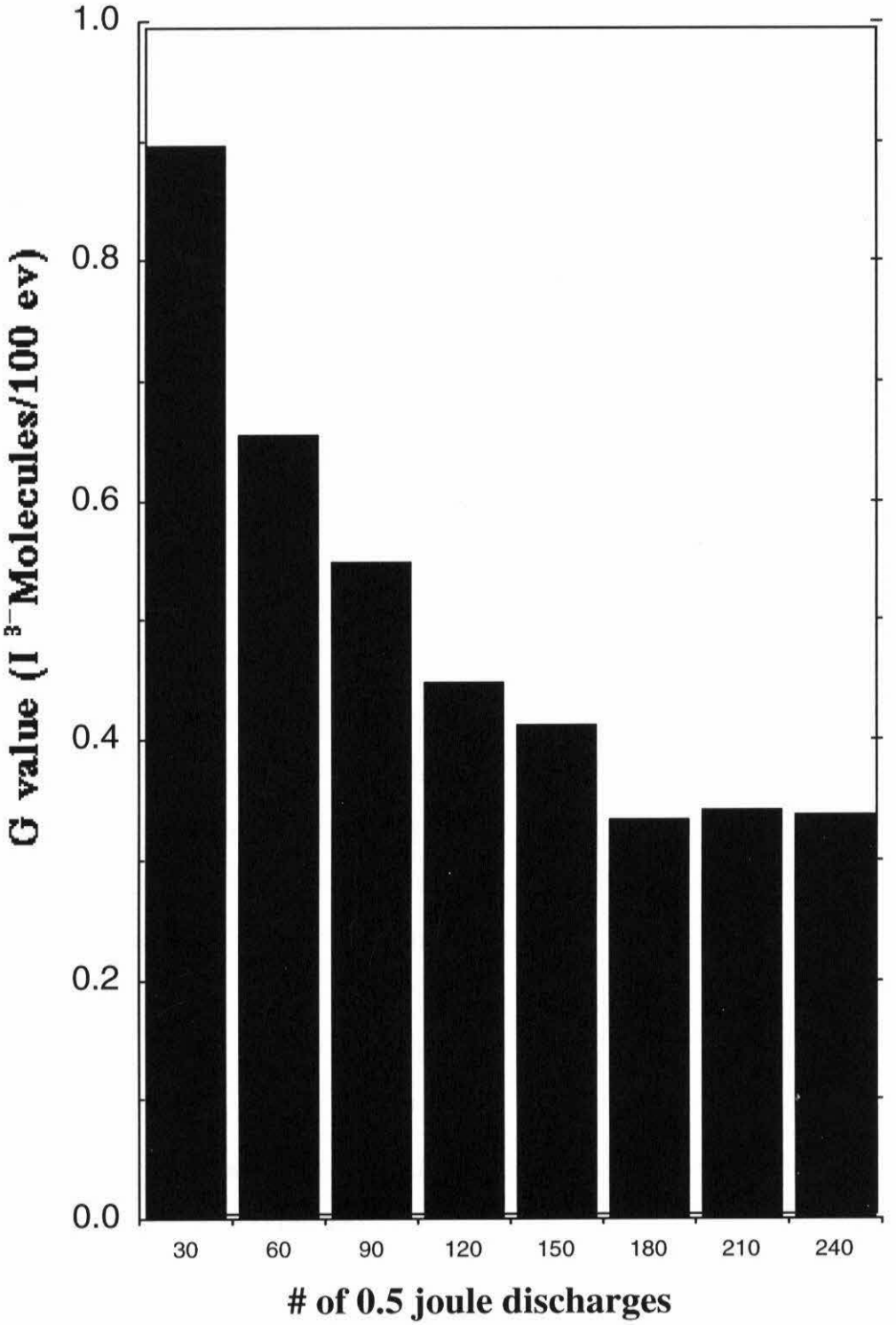

Figure D.10

G values for I_3^- production as a function of number of discharges. As the number of discharges increases, the efficiency decreases.

Figure D.10 shows the decrease in G-value for the measurements shown in figure D.9. The G-value corresponds to the molecules of I_3^- generated per 100 eV of input energy. We assumed 0.5 *joules* per discharge as given by Equation D.2.

D.5 Discussion

The higher I_3^- concentrations shown in Table D.1 for amber bottles versus clear bottles suggest that radiation seems to be an important mechanism for inducing the oxidation of I^-. Most of the other results shown in Table D.1 are inconclusive, since data on the UV transmission coefficient for the dark bottles is lacking. Figure D.9 shows that the concentration of iodide increases as a function of number of discharges, but begins to taper off. The results beyond 150 discharges are probably biased due to a number of effects, including exposure to radiation, absorption of I_3^- to the bottle walls, and oxidation of I_3^- to IO_3^-. The tapering off of the efficiency can also be explained by noting that with the presence of hydrated electrons [6], two competing pathways exist for the creation and destruction of I_3^-. Radiation leads to the destruction of I_3^- by the following mechanism;

$$I^- \xrightarrow{h\nu} I^{\cdot} + \bar{e}_{aq}. \qquad \text{D.5}$$

Electromagnetic radiation induced and Cavitation induced OH radicals also contributes to the net oxidation:

$$\begin{aligned} I^- + OH^{\cdot} &\rightarrow I^{\cdot} + OH^- \\ I^{\cdot} + I^- &\leftrightarrow I_2^{\cdot-} \\ I_2^{\cdot-} + {}^{\cdot}OH &\rightarrow I_2 + OH^- \\ I_2 + I^- &\leftrightarrow I_3^- \end{aligned} \qquad \text{D.6}$$

while hydrated electrons generated from electromagnetic radiation and from the discharge plasma lead to the destruction of I_3^-:

$$I_3^- + \bar{e}_{aq} \longrightarrow I_2^{\cdot -} + I^-. \qquad \text{D.7}$$

The presence of OH radicals can also lead to a decrease in $[I_3^-]$, because of the equilibrium reaction $I_2 + I^- \leftrightarrow I_3^-$. Any I_2 present will undergo reactions with OH radicals:

$$I_2 + OH^{\cdot} \rightarrow IOH + I^{\cdot}. \qquad \text{D.8}$$

We define

$$[I_3^-]_{Total} = [I_3^-] + [I_2]. \qquad \text{D.9}$$

Hence we propose the following equation to explain the observed kinetics:

$$\frac{d}{dt}[I_3^-] = k_{Cavitation}[OH^{\cdot}][I^-] + k_{\gamma}[I^-] - k_{Hydrated}[\bar{e}_{aq}][I_3^-] - k_{OH}[OH^{\cdot}][I_2]. \qquad \text{D.10}$$

Equation D.10 would explain the flattening of the curve in figure D.9 and the decrease in I_3^- yield shown in Figure D.10. But direct modeling of the kinetics is difficult unless we have a fast repetitive pulsed discharge system. The discharges in this experiment were triggered manually, and therefore, at least 15 to 20 seconds elapsed in between each discharges, making the assignment of a time scale somewhat arbitrary.

The data obtained so far shows no significant chemical effects at the focus which are attributed to cavitation induced shock waves. The evidence is conclusive that the oxidation of I^- in the reactor is primarily due to photochemical processes. Two possible explanations have been presented for the observed gradual decrease in efficiency: I_2 evaporation and competing hydrated electron reduction processes.

These conclusions do not rule out that the shock waves could be used to induce chemical degradation. As mentioned previously, the total amount of energy transferred from the capacitor to the discharge is only 0.5 joules per discharge. This energy implies the shock waves may not have very high pressure amplitudes.. The second factor which may be relevant is that the system is not capable of pulsed discharges in rapid succession. The discharge was triggered manually; requiring that at least 15 seconds passed in between each discharge. Hence, no cavitation activation could take place, and any air bubbles created in a previous discharge would have had time to dissipate. This fact is well known from work [7] in sonochemistry with pulsed ultrasound. More studies have to be done with high repetition EHD systems.

References

[1] Gravenstein, J.S.; Peter, K. *Extracorporeal Shock -Wave Lithotripsy for Renal Stone Disease*, Butterworths, Boston,1986, pp. 20

[2] Schaaffs, W. Frequenz; *Zeitschrift für Schwingungs- und Schwachstromtechnik*

[3] Hertz, G, German Patent DRP 749021, 1940

[4] R.R. Buntzen, The Use of Exploding Wires in the Study of Small-Scale Underwater Explosions In: *Exploding Wires, Vol. 2*, Ed. by W.G. Chase and H.K. Moore, Plenum Press, New York, 1962

[5] A.O. Allen et al., *J. Phys. Chem.* **1952,** *56*, 575-586

[6] V.L. Goryachev, A.S. Remennyi, N.A. Silin, *Sov. Tech. Phys. Lett.*, **1990** *16*, pp. 439

[7] Henglein, A.; Gutiérrez, M. *Int. J. Rad. Biol.* **1986** *50*, pp. 527,

Appendix E: Mathcad Programs

First, we initialize the constant parameters of the discharge:

First water constant α:	$\alpha := 3001 \cdot 10^{5}$	Pascals
Second water constant β:	$\beta := 3000 \cdot 10^{5}$	Pascals
Third water constant ρ_o:	$\rho_o := 1 \cdot 10^{3}$	kg/m^3
Stefan-Boltzmann constant σ_B:	$\sigma_B := 5.67051 \cdot 10^{-8}$	W/m^2 °K^4
Stefan-Boltzmann constant k:	$k := 1.38066 \cdot 10^{-23}$	J/°K
The permeability constant:	$\mu_o := 4 \cdot \pi \cdot 10^{-7}$	H/m
The permittivity consant:	$\varepsilon_o := 8.85419 \cdot 10^{-12}$	F/m
The elementary charge unit:	$e := 1.602 \cdot 10^{-19}$	Coulombs
Avogrado's Number:	$N_A := 1.602 \cdot 10^{23}$	Particles/Mole
Energy of H_2O Vaporization:	$\varepsilon_{vapor} := 2.54 \cdot 10^{-20}$	Joules/particle evaporated
Constants of the equ. of state:	$\Omega_B := 45.010507$	$m_H := 1.008 \cdot 10^{-3}$
	$\Omega_C := 8.33527 \cdot 10^{8}$	$m_O := 16 \cdot 10^{-3}$
	$\Omega_D := 1.08318 \cdot 10^{-3}$	$M := \frac{1}{N_A} \cdot \left(\frac{2}{3} \cdot m_H + \frac{1}{3} \cdot m_O \right)$
	$\Omega_E := 3.06708 \cdot 10^{2}$	

Next, we initialize the parameters of the discharge we want to vary:

Variable:	Starting Value:	Ending Value:	Units:
The inductance L:	$L_i := 250 \cdot 10^{-9}$	$L_f := 250 \cdot 10^{-9}$	Henries
The capacitance C:	$C_i := 13.7 \cdot 10^{-6}$	$C_f := 13.7 \cdot 10^{-6}$	Farads
The electrode gap l:	$l_i := 1.5 \cdot 10^{-2}$	$l_f := 1.5 \cdot 10^{-2}$	Meters
The integration constant c_1:	$c1_i := 1.2 \cdot 10^{4}$	$c1_f := 1.2 \cdot 10^{4}$	Joules/Deg K
The Initial Voltage U_o:	$U_i := 14 \cdot 10^{3}$	$U_f := 14 \cdot 10^{3}$	Volts
Conduc. Prop. Constant c_2:	$c2_i := 0.014$	$c2_f := 0.014$	
The equilibrium constant γ:	$\gamma_i := 1.22$	$\gamma_f := 1.22$	Dimensionless
The induction constant κ:	$\kappa_i := 1.81 \cdot 10^{-4}$	$\kappa_f := 1.81 \cdot 10^{-4}$	
% of Spectrum contributing to particle induction f:	$f_i := 0.2$	$f_f := 0.2$	Dimensionless
The circuit resistance R_c:	$Rc_i := 0$	$Rc_f := 0$	Ohms
The conductivity cut-off:	$Tc_i := 5000$	$Tc_f := 5000$	°K

LC constant: $2 \cdot \pi \cdot \sqrt{L_i \cdot C_i} \cdot 10^{6} =$ seconds

Assuming we know conductivity, and we take an initial temperature: what should T_c be?

$c_2 := c2_i \quad T_o := 23000 \quad \sigma_o := 43700 \cdot 10^3$

$$T_c := T_o \cdot \ln\left[\frac{c_2 \cdot T_o^{\frac{3}{2}}}{\sigma_o}\right] \quad T_c = -1.563 \cdot 10^5 \quad c_2 \cdot T_o^{\frac{3}{2}} \cdot \exp\left(-\frac{5000}{T_o}\right) = 3.929 \cdot 10^4$$

The parameter vector is given by

The inductance L:	$L=m_0$
The capacitance C:	$C=m_1$
The electrode gap l:	$l=m_2$
The integration constant c_1:	$c_1=m_3$
The Initial Voltage U_o:	$U_o=m_4$
Conduc. Prop. Constant c_2:	$c_2=m_5$
The equilibrium constant γ:	$\gamma=m_6$
The induction constant κ:	$\kappa=m_7$
% of Spectrum contributing to induction:	$f=m_8$
The circuit resistance R_c:	$R_c=m_9$
The conductivity cut-off T_c:	$T_c=m_{10}$

$$m_{trial} := \begin{bmatrix} L_i \\ C_i \\ l_i \\ c1_i \\ U_i \\ c2_i \\ \gamma_i \\ \kappa_i \\ f_i \\ Rc_i \\ Tc_i \end{bmatrix}$$

The function vector is given by:

The charge q:	$q=y_0$
The current I:	$I=y_1$
The temperature T:	$T=y_2$
The channel radius a:	$a=y_3$
The density ρ:	$\rho=y_4$

We define the functions:

The Pressure

$$p(y,m) := y_4 \cdot k \cdot y_2 - \frac{\mu_0 \cdot (y_1)^2}{8 \cdot \pi^2 \cdot (y_3)^2} - \frac{e^2}{32 \cdot \pi^2 \cdot \varepsilon_0} \cdot \left(\frac{4 \cdot \pi \cdot y_4}{3}\right)^{\frac{4}{3}} \qquad \delta p \delta y_1(y,m) := -\left[\frac{2 \cdot \mu_0 \cdot y_1}{8 \cdot \pi^2 \cdot (y_3)^2}\right]$$

$$\delta p \delta y_2(y,m) := y_4 \cdot k \quad \delta p \delta y_3(y,m) := \frac{2 \cdot \mu_0 \cdot (y_1)^2}{8 \cdot \pi^2 \cdot (y_3)^3} \qquad \delta p \delta y_4(y,m) := k \cdot y_2 - \frac{e^2}{32 \cdot \pi \cdot \varepsilon_0} \cdot \frac{4}{3} \cdot \left(\frac{4 \cdot \pi \cdot y_4}{3}\right)^{\frac{1}{3}} \cdot \frac{4 \cdot \pi}{3}$$

The Internal Energy

$$w(y,m) := \frac{y_4 \cdot k \cdot y_2}{m_6 - 1}$$

$$\delta w \delta y_2(y,m) := \frac{y_4 \cdot k}{m_6 - 1}$$

$$\delta w \delta y_4(y,m) := \frac{k \cdot y_2}{m_6 - 1}$$

$$w_T(y,m) := \frac{y_4 \cdot k}{m_6 - 1}$$

$$\delta w T \delta y_2(y,m) := 0$$

$$\delta w T \delta y_4(y,m) := \frac{k}{m_6 - 1}$$

$$w_\rho(y,m) := \frac{k \cdot y_2}{m_6 - 1}$$

$$\delta w \rho \delta y_2(y,m) := \frac{k}{m_6 - 1}$$

$$\delta w \rho \delta y_4(y,m) := 0$$

The Conductivity

$$\sigma(y,m) := m_5 \cdot (y_2)^{\frac{3}{2}} \cdot \exp\left(\frac{-m_{10}}{y_2}\right)$$

$$\delta\sigma\delta y_1(y,m) := 0$$

$$\delta\sigma\delta y_2(y,m) := \frac{3}{2} \cdot m_5 \cdot \sqrt{y_2} \cdot \exp\left(\frac{-m_{10}}{y_2}\right) + 5000 \cdot \frac{m_5}{\sqrt{y_2}} \cdot \exp\left(\frac{-m_{10}}{y_2}\right)$$

$$\delta\sigma\delta y_4(y,m) := 0$$

The Particle Induction Cross-section

$$\sigma_{induct}(y,m) := m_8 \cdot \frac{\sigma_B \cdot (y_2)^4}{\varepsilon_{vapor} \cdot y_4}$$

$$\delta\sigma induct\delta y_1(y,m) := 0$$

$$\delta\sigma induct\delta y_2(y,m) := m_8 \cdot \frac{4 \cdot \sigma_B \cdot (y_2)^3}{\varepsilon_{vapor} \cdot y_4}$$

$$\delta\sigma induct\delta y_4(y,m) := -m_8 \cdot \frac{\sigma_B \cdot (y_2)^4}{\varepsilon_{vapor} \cdot (y_4)^2}$$

The equations which govern the model:

The rate of change of the charge dq/dt is given by I(t):

$$dq(y,m) := y_1$$

The rate of change of the current dI/dt is given by:

$$dI(y,m) := -\frac{m_2}{m_0 \cdot \sigma(y,m) \cdot \pi \cdot (y_3)^2} \cdot y_1 - \frac{y_0}{m_0 \cdot m_1} - \frac{m_9}{m_0} \cdot y_1$$

The rate of change of the plasma channel radius is given by:

$$da(y,m) := \frac{\sqrt{7} \cdot \alpha^{\frac{1}{14}}}{3 \cdot \sqrt{\rho_0}} \cdot \left[(|p(y,m)| + \beta)^{\frac{3}{7}} - \beta^{\frac{3}{7}} \right]$$

$$\delta da \delta y_1(y,m) := \frac{1}{7} \cdot \sqrt{7} \cdot \frac{\alpha^{\left(\frac{1}{14}\right)}}{\left[\sqrt{\rho_0} \cdot (|p(y,m)| + \beta)^{\left(\frac{4}{7}\right)} \right]} \cdot \delta p \delta y_1(y,m)$$

$$\delta da \delta y_2(y,m) := \frac{1}{7} \cdot \sqrt{7} \cdot \frac{\alpha^{\left(\frac{1}{14}\right)}}{\left[\sqrt{\rho_0} \cdot (|p(y,m)| + \beta)^{\left(\frac{4}{7}\right)} \right]} \cdot \delta p \delta y_2(y,m)$$

$$\delta da \delta y_4(y,m) := \frac{1}{7} \cdot \sqrt{7} \cdot \frac{\alpha^{\left(\frac{1}{14}\right)}}{\left[\sqrt{\rho_0} \cdot (|p(y,m)| + \beta)^{\left(\frac{4}{7}\right)} \right]} \cdot \delta p \delta y_4(y,m)$$

The rate of change of the plasma channel density is given by: condens := 1

$$d\rho(y,m) := \left[2 \cdot \frac{y_4}{y_3} \cdot \left(\sigma_{induct}(y,m) - da(y,m) \right) \right] \cdot condens$$

$$\delta d\rho \delta y_1(y,m) := \left[2 \cdot \frac{y_4}{y_3} \cdot \left(\delta\sigma induct\delta y_1(y,m) - \delta da\delta y_1(y,m) \right) \right] \cdot condens$$

$$\delta d\rho \delta y_2(y,m) := \left[2 \cdot \frac{y_4}{y_3} \cdot \left(\delta\sigma induct\delta y_2(y,m) - \delta da\delta y_2(y,m) \right) \right] \cdot condens$$

$$\delta d\rho \delta y_3(y,m) := \left[-2 \cdot \frac{y_4}{(y_3)^2} \cdot \left(\sigma_{induct}(y,m) - da(y,m) \right) \right] \cdot condens$$

$$\delta d\rho \delta y_4(y,m) := \left[\frac{2}{y_3} \cdot \left(\sigma_{induct}(y,m) - da(y,m) \right) + 2 \cdot \frac{y_4}{y_3} \cdot \left(\delta\sigma induct\delta y_4(y,m) - \delta da\delta y_4(y,m) \right) \right] \cdot condens$$

We solve the energy balance equation for dT/dt, so that we get:

$$dT(y,m) := \frac{(y_1)^2}{\pi^2 \cdot \sigma(y,m) \cdot w_T(y,m) \cdot (y_3)^4} - \frac{w_\rho(y,m)}{w_T(y,m)} \cdot d\rho(y,m) - 2 \cdot \frac{w(y,m) + p(y,m)}{y_3 \cdot w_T(y,m)} \cdot da(y,m)$$

$$- 2 \cdot \sigma_B \cdot \frac{(y_2)^4}{w_T(y,m) \cdot y_3}$$

We define the vector D to put into rkdumb:

$$DD(t,y,m) := \begin{bmatrix} dq(y,m) \\ dI(y,m) \\ dT(y,m) \\ da(y,m) \\ d\rho(y,m) \end{bmatrix}$$

We write out the Jacobian:

Collumn 0: Differentiate DD(t,y,m) with respect to t:

$$\delta D\delta t(t,y) := \begin{bmatrix} 0 \\ 0 \\ 0 \\ 0 \\ 0 \end{bmatrix}$$

Collumn 1: Differentiate DD(t,y,m) with respect to y_0:

$$\delta D\delta y_0(t,y,m) := \begin{bmatrix} 0 \\ \dfrac{-1}{(m_0 \cdot m_1)} \\ 0 \\ 0 \\ 0 \end{bmatrix}$$

Collumn 2: Differentiate DD(t,y,m) with respect to y_1:

$$\delta D\delta y_1(t,y,m) := \begin{bmatrix} \dfrac{1}{\dfrac{m_2}{m_0 \cdot \sigma(y,m)^2 \cdot \pi \cdot (y_3)^2} \cdot y_1 \cdot \delta\sigma\delta y_1(y,m) - \dfrac{m_2}{m_0 \cdot \sigma(y,m) \cdot \pi \cdot (y_3)^2} - \dfrac{m_9}{m_0}} \\ 2 \cdot \dfrac{y_1}{\pi^2 \cdot \sigma(y,m) \cdot w_T(y,m) \cdot (y_3)^4} - \dfrac{(y_1)^2 \cdot \delta\sigma\delta y_1(y,m)}{\pi^2 \cdot \sigma(y,m)^2 \cdot w_T(y,m) \cdot (y_3)^4} - \dfrac{w_\rho(y,m)}{w_T(y,m)} \cdot \delta d\rho\delta y_1(y,m) - 2 \cdot \dfrac{w(y,m) + p(y,m)}{y_3 \cdot w_T(y,m)} \cdot \delta da\delta y_1(y,m) \\ \dfrac{1}{7} \cdot \sqrt{7} \cdot \dfrac{\alpha^{\left(\frac{1}{14}\right)}}{\left[\sqrt{\rho_0} \cdot (p(y,m) + \beta)^{\left(\frac{4}{7}\right)}\right]} \cdot \delta p\delta y_1(y,m) \\ \left[2 \cdot \dfrac{y_4}{y_3} \cdot \left(\delta\sigma\text{induct}\,\delta y_1(y,m) - \delta da\delta y_1(y,m)\right)\right] \cdot \text{condens} \end{bmatrix}$$

Collumn 3: Differentiate DD(t,y,m) with respect to y_2:

$$\delta D\delta y_2(t,y,m) := \begin{bmatrix} 0 \\ \dfrac{m_2}{\left[m_0\cdot\left[\sigma(y,m)^2\cdot\left[\pi\cdot\left(y_3\right)^2\right]\right]\right]}\cdot y_1\cdot\delta\sigma\delta y_2(y,m) \\ \dfrac{1}{7}\cdot\sqrt{7}\cdot\dfrac{\alpha^{\left(\frac{1}{14}\right)}}{\left[\sqrt{\rho_0}\cdot(p(y,m)+\beta)^{\left(\frac{4}{7}\right)}\right]}\cdot\delta p\delta y_2(y,m) \\ \left[2\cdot\dfrac{y_4}{y_3}\cdot\left(\delta\sigma\text{induct}\delta y_2(y,m)-\delta da\delta y_2(y,m)\right)\right]\cdot\text{condens} \end{bmatrix}$$

where

$$fD(t,y,m) = \frac{-\left(y_1\right)^2\cdot\delta\sigma\delta y_2(y,m)}{\pi^2\cdot\sigma(y,m)^2\cdot w_T(y,m)\cdot\left(y_3\right)^4} - \frac{\left(y_1\right)^2\cdot\delta wT\delta y_2(y,m)}{\pi^2\cdot\sigma(y,m)\cdot w_T(y,m)^2\cdot\left(y_3\right)^4} - \frac{\delta w\rho\delta y_2(y,m)}{w_T(y,m)}\cdot d\rho(y,m)$$

$$-\frac{w_\rho(y,m)}{w_T(y,m)^2}\cdot d\rho(y,m)\cdot\delta wT\delta y_2(y,m) - \frac{w_\rho(y,m)}{w_T(y,m)}\cdot\delta d\rho\delta y_2(y,m) - 2\cdot\frac{\delta w\delta y_2(y,m)+\delta p\delta y_2(y,m)}{y_3\cdot w_T(y,m)}\cdot da(y,m)$$

$$+\ 2\cdot\frac{(w(y,m)+p(y,m))}{y_3\cdot w_T(y,m)^2}\cdot da(y,m)\cdot\delta wT\delta y_2(y,m) - 2\cdot\frac{w(y,m)+p(y,m)}{\left(y_3\cdot w_T(y,m)\right)}\cdot\delta da\delta y_2(y,m) - \frac{8\cdot\sigma_B\cdot\left(y_2\right)^3}{y_3\cdot w_T(y,m)}$$

$$+\ 2\cdot\sigma_B\cdot\frac{\left(y_2\right)^4\cdot\delta wT\delta y_2(y,m)}{y_3\cdot w_T(y,m)^2}$$

Collumn 4: Differentiate DD(t,y,m) with respect to y_3:

$$\delta D\delta y_3(t,y,m) := \begin{bmatrix} 0 \\ 2\cdot\dfrac{m_2}{m_0\cdot\sigma(y,m)\cdot\pi\cdot(y_3)^3}\cdot y_1 \\ -4\cdot\dfrac{(y_1)^2}{\pi^2\cdot\sigma(y,m)\cdot w_T(y,m)\cdot(y_3)^5} - \dfrac{w_\rho(y,m)}{w_T(y,m)}\cdot\delta d\rho\delta y_3(y,m) + 2\cdot\dfrac{w(y,m)+p(y,m)}{(y_3)^2\cdot w_T(y,m)}\cdot da(y,m) - 2\cdot\dfrac{\delta p\delta y_3(y,m)}{y_3\cdot w_T(y,m)}\cdot da(y,m) + 2\cdot\sigma_B\cdot\dfrac{(y_2)^4}{(y_3)^2\cdot w_T(y,m)} \\ \dfrac{1}{7}\cdot\sqrt{7}\cdot\dfrac{\alpha^{\left(\frac{1}{14}\right)}}{\left[\sqrt{\rho_0}\cdot(p(y,m)+\beta)^{\left(\frac{4}{7}\right)}\right]}\cdot\delta p\delta y_3(y,m) \\ \left[-2\cdot\dfrac{y_4}{(y_3)^2}\cdot\left(\sigma_{induct}(y,m) - da(y,m)\right)\right]\cdot condens \end{bmatrix}$$

Collumn 5: Differentiate DD(t,y,m) with respect to y_4:

$$\delta D\delta y_4(t,y,m) := \begin{bmatrix} 0 \\ \dfrac{m_2}{m_0\cdot\sigma(y,m)^2\cdot\pi\cdot(y_3)^2}\cdot y_1\cdot\delta\sigma\delta y_4(y,m) \\ \dfrac{1}{7}\cdot\sqrt{7}\cdot\dfrac{\alpha^{\left(\frac{1}{14}\right)}}{\left[\sqrt{\rho_0}\cdot(p(y,m)+\beta)^{\left(\frac{4}{7}\right)}\right]}\cdot Df2(t,y,m)\cdot\delta p\delta y_4(y,m) \\ \left[\dfrac{2}{y_3}\cdot\left(\sigma_{induct}(y,m)-da(y,m)\right)+2\cdot\dfrac{y_4}{y_3}\cdot\left(\delta\sigma induct\delta y_4(y,m)-\delta da\delta y_4(y,m)\right)\right]\cdot condens \end{bmatrix}$$

where

$$Df2(t,y,m) = \frac{-(y_1)^2}{\pi^2\cdot\sigma(y,m)^2\cdot w_T(y,m)\cdot(y_3)^4}\cdot\delta\sigma\delta y_4(y,m) - \frac{(y_1)^2\cdot\delta wT\delta y_4(y,m)}{\pi^2\cdot\sigma(y,m)\cdot w_T(y,m)^2\cdot(y_3)^4}$$

$$-\frac{\delta w\rho\delta y_4(y,m)}{w_T(y,m)}\cdot d\rho(y,m) + \frac{w_\rho(y,m)}{w_T(y,m)^2}\cdot d\rho(y,m)\cdot\delta wT\delta y_4(y,m) - \frac{w_\rho(y,m)}{w_T(y,m)}\cdot\delta d\rho\delta y_4(y,m)$$

$$-2\cdot\frac{\delta w\delta y_4(y,m)+\delta p\delta y_4(y,m)}{y_3\cdot w_T(y,m)}\cdot da(y,m) + 2\cdot\frac{w(y,m)+p(y,m)}{y_3\cdot w_T(y,m)^2}\cdot da(y,m)\cdot\delta wT\delta y_4(y,m)$$

$$-2\cdot\frac{w(y,m)+p(y,m)}{y_3\cdot w_T(y,m)}\cdot\delta da\delta y_4(y,m) + 2\cdot\sigma_B\cdot\frac{(y_2)^4}{y_3\cdot w_T(y,m)^2}\cdot\delta wT\delta y_4(y,m)$$

Next, we set the initial conditions:

The initial conditions are fully determined by U_o, R_o, a_o and p_o.

$q_o = C \cdot U_o$ charge on a capacitor law

$I_o = \frac{U_o}{R_o + R_c}$ Ohm's law

a_o is given

Then, we can obtain the initial temperautre and conductivity from the following two equations:

$\frac{1}{\sigma \cdot \pi \cdot a^2} = R_o$ definition of conductivity $p_o = p(T_o, \rho_o)$ equation of state.

So we need to solve for T_o and ρ_o out of the following equations:

$\frac{1}{\pi \cdot R_o \cdot a_o^2} = c_2 \cdot T_o^{\frac{3}{2}} \cdot \exp\left(\frac{-T_c}{T_o}\right)$ solve for T out of this equation

$p_o = \rho \cdot k \cdot T$ solve for ρ_o out of this equation.

Now, we are ready to evaluate the initial conditions:

Some typical initial values are: $p_o = 1 \cdot 10^5$ $a_o = 0.3 \cdot 10^{-3}$ $w_o = 4.545 \cdot 10^8$ $n_o = 1 \cdot 10^{27}$

we define the parameters which determine all the initial conditions:

Variable:	Starting Value:	Ending Value:	Units:
The initial *pressure p:*	$P1_i := 100 \cdot 10^5$	$P1_f := 100 \cdot 10^5$	*pascals*
The initial *Resistance R_o:*	$P2_i := 100$	$P2_f := 100$	*Ohms*
The initial *radius a:*	$P3_i := 0.5 \cdot 10^{-3}$	$P3_f := 0.5 \cdot 10^{-3}$	*meters*

$$pp_{trial} := \begin{bmatrix} 0 \\ P1_i \\ P2_i \\ P3_i \end{bmatrix}$$

We define the functions to solve for temperature and density:If we have T_o, what R_o should we use?

$x1 := 1000 \quad ^oK$

$$temp(m, pp) := root\left[m_5 \cdot x1^{\frac{3}{2}} \cdot \exp\left(\frac{-m_{10}}{x1}\right) - \frac{m_2}{\pi \cdot pp_2 \cdot (pp_3)^2}, x1 \right] \qquad R(T, c_2) := \frac{m_{trial_2}}{\pi \cdot P3_i^{\,2} \cdot c_2 \cdot T^{\frac{3}{2}} \cdot \exp\left(\frac{-m_{trial_{10}}}{T}\right)}$$

We test out this function: $temp(m_{trial}, pp_{trial}) = 2.353 \cdot 10^3 \qquad I(T, c_2) := \frac{m_{trial_4}}{R(T, c_2) + m_{trial_9}}$

We figure out a trial number for density: $R(1000, 0.0032) = 2.80 \quad I(1000, c2_i) = 2.187$

$$m_H := \frac{1.008 \cdot 10^{-3}}{1.602 \cdot 10^{23}} \qquad m_O := \frac{16 \cdot 10^{-3}}{1.602 \cdot 10^{23}} \qquad n := 10^{24} \qquad x2 := \left(\frac{2}{3} \cdot m_H + \frac{1}{3} \cdot m_O\right) \cdot n \qquad x2 = 0.037$$

$$dens(m, pp, T_o) := \frac{pp_1}{k \cdot T_o}$$

We test out this function: $dens(m_{trial}, pp_{trial}, temp(m_{trial}, pp_{trial})) = 3.078 \cdot 10^{26}$

We define the initial condition vector function:

$$init(m, pp, T_o) := \begin{bmatrix} m_1 \cdot m_4 \\ -\frac{m_4}{pp_2 + m_9} \\ temp(m, pp) \\ pp_3 \\ dens(m, pp, T_o) \end{bmatrix}$$

$PP_1 = p_o$

$PP_2 = R_o$

$pp_3 = a_o$

The parameter vector is given by

The inductance L:	$L=m_0$
The capacitance C:	$C=m_1$
The electrode gap l:	$l=m_2$
The integration constant c_1:	$c_1=m_3$
The Initial Voltage U_o:	$U_o=m_4$
Conduc. Prop. Constant c_2:	$c2=m_5$
The equilibrium constant γ:	$\gamma=m_6$
The induction constant κ:	$\kappa=m_7$

The function vector is given by

y_0=Charge q_o:

y_1=Current I_o:

y_2=Temperature T_o:

y_3=Channel radius a_o:

y_4=plasma density ρ_o:

Next, we create the initial condition vectors for the whole spectrum of parameters chosen:

$r := 1,2..10$

The inductance L: $c_{0,r} := L_i + \frac{L_f - L_i}{9} \cdot (r-1)$

The capacitance C: $c_{1,r} := C_i + \frac{C_f - C_i}{9} \cdot (r-1)$

The electrode gap l: $c_{2,r} := l_i + \frac{l_f - l_i}{9} \cdot (r-1)$

The integration constant c_1: $c_{3,r} := c1_i + \frac{c1_f - c1_i}{9} \cdot (r-1)$

The Initial Voltage U_o: $c_{4,r} := U_i + \frac{U_f - U_i}{9} \cdot (r-1)$

Conductiv. Prop. Constant: $c_{5,r} := c2_i + \frac{c2_f - c2_i}{9} \cdot (r-1)$

The equilibrium constant γ: $c_{6,r} := \gamma_i + \frac{\gamma_f - \gamma_i}{9} \cdot (r-1)$

The ionization constant κ: $c_{7,r} := \kappa_i + \frac{\kappa_f - \kappa_i}{9} \cdot (r-1)$

The induction fraction f: $c_{8,r} := f_i + \frac{f_f - f_i}{9} \cdot (r-1)$

The circuit resistance R_c: $c_{9,r} := Rc_i + \frac{Rc_f - Rc_i}{9} \cdot (r-1)$

The conduct. cut-off T_c: $c_{10,r} := Tc_i + \frac{Tc_f - Tc_i}{9} \cdot (r-1)$

$c_{2,1} := 1.27 \cdot 10^{-2}$ $c_{5,1} := 0.01411$

$c_{2,2} := 2.54 \cdot 10^{-2}$ $c_{5,2} := 0.01411$

$c_{2,3} := 3.81 \cdot 10^{-2}$ $c_{5,3} := 0.01411$

$c_{2,4} := 5.08 \cdot 10^{-2}$ $c_{5,4} := 0.01411$

$c_{2,5} := 1.27 \cdot 10^{-2}$ $c_{5,5} := 0.0032$

$c_{2,6} := 2.54 \cdot 10^{-2}$ $c_{5,6} := 0.0032$

$c_{2,7} := 3.81 \cdot 10^{-2}$ $c_{5,7} := 0.0032$

$c_{2,8} := 5.08 \cdot 10^{-2}$ $c_{5,8} := 0.0032$

$c_{2,9} := 1.27 \cdot 10^{-2}$ $c_{5,9} := 0.005$

$c_{2,10} := 1.27 \cdot 10^{-2}$ $c_{5,10} := 0.009$

Initial parameter 1 p_o: $pp_{1,r} := P1_i + \frac{P1_f - P1_i}{9} \cdot (r-1)$

Initial parameter 3 a_o: $pp_{3,r} := P3_i + \frac{P3_f - P3_i}{9} \cdot (r-1)$

Initial parameter 2 R_o: $pp_{2,r} := P2_i + \frac{P2_f - P2_i}{9} \cdot (r-1)$ $pp_{2,r} = R(1000, c_{5,r})$

$c =$

	0	1	2	3	4
0	0	$2.5 \cdot 10^{-7}$	$2.5 \cdot 10^{-7}$	$2.5 \cdot 10^{-7}$	$2.5 \cdot 10^{-7}$
1	0	$1.37 \cdot 10^{-5}$	$1.37 \cdot 10^{-5}$	$1.37 \cdot 10^{-5}$	$1.37 \cdot 10^{-5}$
2	0	0.013	0.025	0.038	0.051
3	0	$1.2 \cdot 10^{4}$	$1.2 \cdot 10^{4}$	$1.2 \cdot 10^{4}$	$1.2 \cdot 10^{4}$
4	0	$1.4 \cdot 10^{4}$	$1.4 \cdot 10^{4}$	$1.4 \cdot 10^{4}$	$1.4 \cdot 10^{4}$
5	0	0.014	0.014	0.014	0.014
6	0	1.22	1.22	1.22	1.22
7	0	$1.81 \cdot 10^{-4}$	$1.81 \cdot 10^{-4}$	$1.81 \cdot 10^{-4}$	$1.81 \cdot 10^{-4}$
8	0	0.2	0.2	0.2	0.2
9	0	0	0	0	0
10	0	$5 \cdot 10^{3}$	$5 \cdot 10^{3}$	$5 \cdot 10^{3}$	$5 \cdot 10^{3}$

L - Henries

C - Farads

l - Meters

c_1 -

U_o - Volts

c_2 -

γ - Dimensionless

κ -

$pp =$

	0	1	2	3	4	5	6
0	0	0	0	0	0	0	0
1	0	$1 \cdot 10^{7}$	$1 \cdot 10^{7}$	$1 \cdot 10^{7}$	$1 \cdot 10^{7}$	$1 \cdot 10^{7}$	$1 \cdot 10^{7}$
2	0	100	100	100	100	100	100
3	0	$5 \cdot 10^{-4}$	$5 \cdot 10^{-4}$	$5 \cdot 10^{-4}$	$5 \cdot 10^{-4}$	$5 \cdot 10^{-4}$	$5 \cdot 10^{-4}$

P1: pressure

P2: Resistance

P3: Radius

$$initial^{\langle\rangle} := init\left(c^{\langle\rangle}, pp^{\langle\rangle}, temp\left(c^{\langle\rangle}, pp^{\langle\rangle}\right)\right)$$

$initial =$

	0	1	2	3	4
0	0	0.192	0.192	0.192	0.192
1	0	-140	-140	-140	-140
2	0	$2.244 \cdot 10^{3}$	$2.733 \cdot 10^{3}$	$3.099 \cdot 10^{3}$	$3.407 \cdot 10^{3}$
3	0	$5 \cdot 10^{-4}$	$5 \cdot 10^{-4}$	$5 \cdot 10^{-4}$	$5 \cdot 10^{-4}$
4	0	$3.227 \cdot 10^{26}$	$2.651 \cdot 10^{26}$	$2.337 \cdot 10^{26}$	$2.126 \cdot 10^{26}$

Next, we test out all the functions for self-consistency:

$yy := initial^{\langle 1 \rangle}$ $\quad mm := c^{\langle 1 \rangle}$

The parameter vector is given by

The inductance L:	$L=m_0$
The capacitance C:	$C=m_1$
The electrode gap l:	$l=m_2$
The integration constant c_1:	$c_1=m_3$
The Initial Voltage U_o:	$U_o=m_4$
Conduc. Prop. Constant c_2:	$c_2=m_5$
The equilibrium constant γ:	$\gamma=m_6$
The induction constant κ:	$\kappa=m_7$

Pressure: $P1_i = 1 \cdot 10^7$ $\quad p(yy, mm) = -3.718 \cdot 10^6$

Resistance: $P2_i = 100$ $\quad \dfrac{mm_2}{\sigma(yy, mm) \cdot \pi \cdot (yy_3)^2} = 100$

Radius: $P3_i = 5 \cdot 10^{-4}$ $\quad yy_3 = 5 \cdot 10^{-4}$

Voltage: $mm_4 = 1.4 \cdot 10^4$ $\quad \dfrac{mm_2 \cdot yy_1}{\sigma(yy, mm) \cdot \pi \cdot (yy_3)^2} = -1.4 \cdot 10^4$

Charge: $mm_1 \cdot mm_4 = 0.192$ $\quad yy_0 = 0.192$

$$DD(0, yy, mm) = \begin{bmatrix} -140 \\ 122.931 \\ 9.704 \cdot 10^9 \\ 2.557 \\ -3.255 \cdot 10^{30} \end{bmatrix}$$

$$DD\left(0, initial^{\langle 1 \rangle}, c^{\langle 1 \rangle}\right) = \begin{bmatrix} -140 \\ 122.931 \\ 9.704 \cdot 10^9 \\ 2.557 \\ -3.255 \cdot 10^{30} \end{bmatrix}$$

Next, we initialize the time steps to take:

Specify beginning and ending times: $t_0 := 0 \cdot 10^{-6}$ Seconds

$t_1 := 50 \cdot 10^{-6}$ Seconds

$\Delta t := 2 \cdot 10^{-9}$ Seconds

so that we take $steps := floor\left(\dfrac{t_1 - t_0}{\Delta t}\right)$ $\quad steps = 2.5 \cdot 10^4$

Because Mathcad doesn't have loops in the macro language, we have to define 10 separate runs. We write to the same data file.

Run: number := 1 num := number − 1 next := 1111·number

We use a solver with an implicit approach: $D(t,y) := DD(t,y,c^{\langle number \rangle})$ $J(t,y) := JJ(t,y,c^{\langle number \rangle})$

$RS := Stiffb(initial^{\langle number \rangle}, t_0, t_1, steps, D, J)$

$param_0 := c_{0,number} \cdot 10^9$ $param_1 := c_{1,number} \cdot 10^6$

$param_2 := c_{2,number} \cdot 10^2$ $param_3 := c_{3,number}$

$param_4 := c_{4,number} \cdot 10^{-3}$ $param_5 := c_{5,number}$

$param_6 := c_{6,number}$ $param_7 := c_{7,number}$

$param_8 := pp_{1,number}$ $param_9 := pp_{2,number}$

$param_{10} := pp_{3,number}$ $param_{11} := t_1 \cdot 10^6$

$param_{12} := \Delta t \cdot 10^9$ $param_{13} := c_{8,number}$

$param_{14} := 2$ $param_{15} := 3$

$param_{16} := 4$ $param_{17} := 5$

$param_{18} := 6$ $param_{19} := 7$

$param_{20} := 8$ $param_{21} := 9$

$param_{22} := 10$ $param_{23} := next$

We write data to disk:

$kk := 0, 1 .. 100$ $d := floor\left(\frac{steps}{100}\right)$

$data_{kk,0} := RS_{d \cdot kk,0} \cdot 10^6$ Time in Microseconds

$data_{kk,1} := RS_{d \cdot kk,1}$ Charge in Coulombs

$data_{kk,2} := -1 \cdot RS_{d \cdot kk,2} \cdot 10$ Current in kA

$data_{kk,3} := RS_{d \cdot kk,3}$ Internal Energy in J/m

$data_{kk,4} := RS_{d \cdot kk,4} \cdot 10^3$ Channel Radius in mm

$data_{kk,5} := RS_{d \cdot kk,5}$ Plasma Density in N/m

$data_{101,0} := next$ $data_{101,1} := next$ $data_{101,2} := next$ $data_{101,3} := next$ $data_{101,4} := next$ $data_{101,5} := next$

WRITEPRN(datas) := data

WRITEPRN(parameters) := param

Run: number := 2 num := number − 1 next := 1111·number

We use a solver with an implicit approach: $D(t,y) := DD(t,y,c^{\langle number \rangle})$ $J(t,y) := JJ(t,y,c^{\langle number \rangle})$

$RS := Stiffb(initial^{\langle number \rangle}, t_0, t_1, steps, D, J)$

$param_0 := c_{0,number} \cdot 10^9$ $param_1 := c_{1,number} \cdot 10^6$

$param_2 := c_{2,number} \cdot 10^2$ $param_3 := c_{3,number}$

$param_4 := c_{4,number} \cdot 10^{-3}$ $param_5 := c_{5,number}$

$param_6 := c_{6,number}$ $param_7 := c_{7,number}$

$param_8 := pp_{1,number}$ $param_9 := pp_{2,number}$

$param_{10} := pp_{3,number}$ $param_{11} := t_1 \cdot 10^6$

$param_{12} := \Delta t \cdot 10^9$ $param_{13} := c_{8,number}$

$param_{14} := 2$ $param_{15} := 3$

$param_{16} := 4$ $param_{17} := 5$

$param_{18} := 6$ $param_{19} := 7$

$param_{20} := 8$ $param_{21} := 9$

$param_{22} := 10$ $param_{23} := next$

We write data to disk:

$kk := 0, 1 .. 100$ $d := floor\left(\frac{steps}{100}\right)$

$data_{kk,0} := RS_{d \cdot kk,0} \cdot 10^6$ Time in Microseconds

$data_{kk,1} := RS_{d \cdot kk,1}$ Charge in Coulombs

$data_{kk,2} := -1 \cdot RS_{d \cdot kk,2} \cdot 10$ Current in kA

$data_{kk,3} := RS_{d \cdot kk,3}$ Internal Energy in J/m

$data_{kk,4} := RS_{d \cdot kk,4} \cdot 10^3$ Channel Radius in mm

$data_{kk,5} := RS_{d \cdot kk,5}$ Plasma Density in N/m

$data_{101,0} := next$ $data_{101,1} := next$ $data_{101,2} := next$ $data_{101,3} := next$ $data_{101,4} := next$ $data_{101,5} := next$

WRITEPRN(datas) := data

WRITEPRN(parameters) := param

Run: number := 3 num := number − 1 next := 1111·number

We use a solver with an implicit approach: $D(t,y) := DD\left(t,y,c^{\langle number\rangle}\right)$ $J(t,y) := JJ\left(t,y,c^{\langle number\rangle}\right)$

$RS := Stiffb\left(initial^{\langle number\rangle}, t_0, t_1, steps, D, J\right)$

We write data to disk:

$kk := 0,1 .. 100$ $d := floor\left(\frac{steps}{100}\right)$

$data_{kk,0} := RS_{d\cdot kk,0}\cdot 10^{6}$ Time in Microseconds

$data_{kk,1} := RS_{d\cdot kk,1}$ Charge in Coulombs

$data_{kk,2} := -1\cdot RS_{d\cdot kk,2}\cdot 10$ Current in kA

$data_{kk,3} := RS_{d\cdot kk,3}$ Internal Energy in J/m

$data_{kk,4} := RS_{d\cdot kk,4}\cdot 10^{3}$ Channel Radius in mm

$data_{kk,5} := RS_{d\cdot kk,5}$ Plasma Density in N/m

$param_0 := c_{0,number}\cdot 10^{9}$ $param_1 := c_{1,number}\cdot 10^{6}$

$param_2 := c_{2,number}\cdot 10^{2}$ $param_3 := c_{3,number}$

$param_4 := c_{4,number}\cdot 10^{-3}$ $param_5 := c_{5,number}$

$param_6 := c_{6,number}$ $param_7 := c_{7,number}$

$param_8 := pp_{1,number}$ $param_9 := pp_{2,number}$

$param_{10} := pp_{3,number}$ $param_{11} := t_1\cdot 10^{6}$

$param_{12} := \Delta t\cdot 10^{9}$ $param_{13} := c_{8,number}$

$param_{14} := 2$ $param_{15} := 3$

$param_{16} := 4$ $param_{17} := 5$

$param_{18} := 6$ $param_{19} := 7$

$param_{20} := 8$ $param_{21} := 9$

$param_{22} := 10$ $param_{23} := next$

$data_{101,0} := next$ $data_{101,1} := next$ $data_{101,2} := next$ $data_{101,3} := next$ $data_{101,4} := next$ $data_{101,5} := next$

WRITEPRN(datas) := data

WRITEPRN(parameters) := param

Run: number := 4 num := number − 1 next := 1111·number

We use a solver with an implicit approach: $D(t,y) := DD\left(t,y,c^{\langle number\rangle}\right)$ $J(t,y) := JJ\left(t,y,c^{\langle number\rangle}\right)$

$RS := Stiffb\left(initial^{\langle number\rangle}, t_0, t_1, steps, D, J\right)$

We write data to disk:

$kk := 0,1 .. 100$ $d := floor\left(\frac{steps}{100}\right)$

$data_{kk,0} := RS_{d\cdot kk,0}\cdot 10^{6}$ Time in Microseconds

$data_{kk,1} := RS_{d\cdot kk,1}$ Charge in Coulombs

$data_{kk,2} := -1\cdot RS_{d\cdot kk,2}\cdot 10$ Current in kA

$data_{kk,3} := RS_{d\cdot kk,3}$ Internal Energy in J/m

$data_{kk,4} := RS_{d\cdot kk,4}\cdot 10^{3}$ Channel Radius in mm

$data_{kk,5} := RS_{d\cdot kk,5}$ Plasma Density in N/m

$param_0 := c_{0,number}\cdot 10^{9}$ $param_1 := c_{1,number}\cdot 10^{6}$

$param_2 := c_{2,number}\cdot 10^{2}$ $param_3 := c_{3,number}$

$param_4 := c_{4,number}\cdot 10^{-3}$ $param_5 := c_{5,number}$

$param_6 := c_{6,number}$ $param_7 := c_{7,number}$

$param_8 := pp_{1,number}$ $param_9 := pp_{2,number}$

$param_{10} := pp_{3,number}$ $param_{11} := t_1\cdot 10^{6}$

$param_{12} := \Delta t\cdot 10^{9}$ $param_{13} := c_{8,number}$

$param_{14} := 2$ $param_{15} := 3$

$param_{16} := 4$ $param_{17} := 5$

$param_{18} := 6$ $param_{19} := 7$

$param_{20} := 8$ $param_{21} := 9$

$param_{22} := 10$ $param_{23} := next$

$data_{101,0} := next$ $data_{101,1} := next$ $data_{101,2} := next$ $data_{101,3} := next$ $data_{101,4} := next$ $data_{101,5} := next$

WRITEPRN(datas) := data

WRITEPRN(parameters) := param

Run: number := 5 num := number – 1 next := 1111·number

We use a solver with an implicit approach: $D(t,y) := DD\left(t,y,c^{\langle number\rangle}\right)$ $J(t,y) := JJ\left(t,y,c^{\langle number\rangle}\right)$

$RS := Stiffb\left(initial^{\langle number\rangle}, t_0, t_1, steps, D, J\right)$

We write data to disk:

$kk := 0, 1 .. 100$ $d := floor\left(\frac{steps}{100}\right)$

$data_{kk,0} := RS_{d\cdot kk,0}\cdot 10^6$ Time in Microseconds

$data_{kk,1} := RS_{d\cdot kk,1}$ Charge in Coulombs

$data_{kk,2} := -1\cdot RS_{d\cdot kk,2}\cdot 10$ Current in kA

$data_{kk,3} := RS_{d\cdot kk,3}$ Internal Energy in J/m

$data_{kk,4} := RS_{d\cdot kk,4}\cdot 10^3$ Channel Radius in mm

$data_{kk,5} := RS_{d\cdot kk,5}$ Plasma Density in N/m

$param_0 := c_{0,number}\cdot 10^9$ $param_1 := c_{1,number}\cdot 10^6$

$param_2 := c_{2,number}\cdot 10^2$ $param_3 := c_{3,number}$

$param_4 := c_{4,number}\cdot 10^{-3}$ $param_5 := c_{5,number}$

$param_6 := c_{6,number}$ $param_7 := c_{7,number}$

$param_8 := pp_{1,number}$ $param_9 := pp_{2,number}$

$param_{10} := pp_{3,number}$ $param_{11} := t_1\cdot 10^6$

$param_{12} := \Delta t\cdot 10^9$ $param_{13} := c_{8,number}$

$param_{14} := 2$ $param_{15} := 3$

$param_{16} := 4$ $param_{17} := 5$

$param_{18} := 6$ $param_{19} := 7$

$param_{20} := 8$ $param_{21} := 9$

$param_{22} := 10$ $param_{23} := next$

$data_{101,0} := next$ $data_{101,1} := next$ $data_{101,2} := next$ $data_{101,3} := next$ $data_{101,4} := next$ $data_{101,5} := next$

WRITEPRN(datas) := data

WRITEPRN(parameters) := param

Run: number := 6 num := number – 1 next := 1111·number

We use a solver with an implicit approach: $D(t,y) := DD\left(t,y,c^{\langle number\rangle}\right)$ $J(t,y) := JJ\left(t,y,c^{\langle number\rangle}\right)$

$RS := Stiffb\left(initial^{\langle number\rangle}, t_0, t_1, steps, D, J\right)$

We write data to disk:

$kk := 0, 1 .. 100$ $d := floor\left(\frac{steps}{100}\right)$

$data_{kk,0} := RS_{d\cdot kk,0}\cdot 10^6$ Time in Microseconds

$data_{kk,1} := RS_{d\cdot kk,1}$ Charge in Coulombs

$data_{kk,2} := -1\cdot RS_{d\cdot kk,2}\cdot 10$ Current in kA

$data_{kk,3} := RS_{d\cdot kk,3}$ Internal Energy in J/m

$data_{kk,4} := RS_{d\cdot kk,4}\cdot 10^3$ Channel Radius in mm

$data_{kk,5} := RS_{d\cdot kk,5}$ Plasma Density in N/m

$param_0 := c_{0,number}\cdot 10^9$ $param_1 := c_{1,number}\cdot 10^6$

$param_2 := c_{2,number}\cdot 10^2$ $param_3 := c_{3,number}$

$param_4 := c_{4,number}\cdot 10^{-3}$ $param_5 := c_{5,number}$

$param_6 := c_{6,number}$ $param_7 := c_{7,number}$

$param_8 := pp_{1,number}$ $param_9 := pp_{2,number}$

$param_{10} := pp_{3,number}$ $param_{11} := t_1\cdot 10^6$

$param_{12} := \Delta t\cdot 10^9$ $param_{13} := c_{8,number}$

$param_{14} := 2$ $param_{15} := 3$

$param_{16} := 4$ $param_{17} := 5$

$param_{18} := 6$ $param_{19} := 7$

$param_{20} := 8$ $param_{21} := 9$

$param_{22} := 10$ $param_{23} := next$

$data_{101,0} := next$ $data_{101,1} := next$ $data_{101,2} := next$ $data_{101,3} := next$ $data_{101,4} := next$ $data_{101,5} := next$

WRITEPRN(datas) := data

WRITEPRN(parameters) := param

Run: number := 7 num := number − 1 next := 1111·number

We use a solver with an implicit approach: $D(t,y) := DD(t,y,c^{\langle number \rangle})$ $J(t,y) := JJ(t,y,c^{\langle number \rangle})$

$RS := Stiffb(initial^{\langle number \rangle}, t_0, t_1, steps, D, J)$

$param_0 := c_{0,number} \cdot 10^9$ $param_1 := c_{1,number} \cdot 10^6$

$param_2 := c_{2,number} \cdot 10^2$ $param_3 := c_{3,number}$

$param_4 := c_{4,number} \cdot 10^{-3}$ $param_5 := c_{5,number}$

$param_6 := c_{6,number}$ $param_7 := c_{7,number}$

$param_8 := pp_{1,number}$ $param_9 := pp_{2,number}$

$param_{10} := pp_{3,number}$ $param_{11} := t_1 \cdot 10^6$

$param_{12} := \Delta t \cdot 10^9$ $param_{13} := c_{8,number}$

$param_{14} := 2$ $param_{15} := 3$

$param_{16} := 4$ $param_{17} := 5$

$param_{18} := 6$ $param_{19} := 7$

$param_{20} := 8$ $param_{21} := 9$

$param_{22} := 10$ $param_{23} := next$

We write data to disk:

$kk := 0, 1 .. 100$ $d := floor\left(\frac{steps}{100}\right)$

$data_{kk,0} := RS_{d \cdot kk,0} \cdot 10^6$ Time in Microseconds

$data_{kk,1} := RS_{d \cdot kk,1}$ Charge in Coulombs

$data_{kk,2} := -1 \cdot RS_{d \cdot kk,2} \cdot 10^2$ Current in kA

$data_{kk,3} := RS_{d \cdot kk,3}$ Internal Energy in J/m

$data_{kk,4} := RS_{d \cdot kk,4} \cdot 10^3$ Channel Radius in mm

$data_{kk,5} := RS_{d \cdot kk,5}$ Plasma Density in N/m

$data_{101,0} := next$ $data_{101,1} := next$ $data_{101,2} := next$ $data_{101,3} := next$ $data_{101,4} := next$ $data_{101,5} := next$

WRITEPRN(datas) := data

WRITEPRN(parameters) := param

Run: number := 8 num := number − 1 next := 1111·number

We use a solver with an implicit approach: $D(t,y) := DD(t,y,c^{\langle number \rangle})$ $J(t,y) := JJ(t,y,c^{\langle number \rangle})$

$RS := Stiffb(initial^{\langle number \rangle}, t_0, t_1, steps, D, J)$

$param_0 := c_{0,number} \cdot 10^9$ $param_1 := c_{1,number} \cdot 10^6$

$param_2 := c_{2,number} \cdot 10^2$ $param_3 := c_{3,number}$

$param_4 := c_{4,number} \cdot 10^{-3}$ $param_5 := c_{5,number}$

$param_6 := c_{6,number}$ $param_7 := c_{7,number}$

$param_8 := pp_{1,number}$ $param_9 := pp_{2,number}$

$param_{10} := pp_{3,number}$ $param_{11} := t_1 \cdot 10^6$

$param_{12} := \Delta t \cdot 10^9$ $param_{13} := c_{8,number}$

$param_{14} := 2$ $param_{15} := 3$

$param_{16} := 4$ $param_{17} := 5$

$param_{18} := 6$ $param_{19} := 7$

$param_{20} := 8$ $param_{21} := 9$

$param_{22} := 10$ $param_{23} := next$

We write data to disk:

$kk := 0, 1 .. 100$ $d := floor\left(\frac{steps}{100}\right)$

$data_{kk,0} := RS_{d \cdot kk,0} \cdot 10^6$ Time in Microseconds

$data_{kk,1} := RS_{d \cdot kk,1}$ Charge in Coulombs

$data_{kk,2} := -1 \cdot RS_{d \cdot kk,2} \cdot 10^2$ Current in kA

$data_{kk,3} := RS_{d \cdot kk,3}$ Internal Energy in J/m

$data_{kk,4} := RS_{d \cdot kk,4} \cdot 10^3$ Channel Radius in mm

$data_{kk,5} := RS_{d \cdot kk,5}$ Plasma Density in N/m

$data_{101,0} := next$ $data_{101,1} := next$ $data_{101,2} := next$ $data_{101,3} := next$ $data_{101,4} := next$ $data_{101,5} := next$

WRITEPRN(datas) := data

WRITEPRN(parameters) := param

Run: number := 9 num := number − 1 next := 1111·number

We use a solver with an implicit approach: $D(t,y) := DD(t,y,c^{\langle number \rangle})$ $J(t,y) := JJ(t,y,c^{\langle number \rangle})$

$RS := Stiffb(initial^{\langle number \rangle}, t_0, t_1, steps, D, J)$

We write data to disk:

$kk := 0,1 .. 100$ $d := floor\left(\frac{steps}{100}\right)$

$data_{kk,0} := RS_{d \cdot kk,0} \cdot 10^6$ Time in Microseconds

$data_{kk,1} := RS_{d \cdot kk,1}$ Charge in Coulombs

$data_{kk,2} := -1 \cdot RS_{d \cdot kk,2} \cdot 10$ Current in kA

$data_{kk,3} := RS_{d \cdot kk,3}$ Internal Energy in J/m

$data_{kk,4} := RS_{d \cdot kk,4} \cdot 10^3$ Channel Radius in mm

$data_{kk,5} := RS_{d \cdot kk,5}$ Plasma Density in N/m

$param_0 := c_{0,number} \cdot 10^9$ $param_1 := c_{1,number} \cdot 10^6$

$param_2 := c_{2,number} \cdot 10^2$ $param_3 := c_{3,number}$

$param_4 := c_{4,number} \cdot 10^{-3}$ $param_5 := c_{5,number}$

$param_6 := c_{6,number}$ $param_7 := c_{7,number}$

$param_8 := pp_{1,number}$ $param_9 := pp_{2,number}$

$param_{10} := pp_{3,number}$ $param_{11} := t_1 \cdot 10^6$

$param_{12} := \Delta t \cdot 10^9$ $param_{13} := c_{8,number}$

$param_{14} := 2$ $param_{15} := 3$

$param_{16} := 4$ $param_{17} := 5$

$param_{18} := 6$ $param_{19} := 7$

$param_{20} := 8$ $param_{21} := 9$

$param_{22} := 10$ $param_{23} := next$

$data_{101,0} := next$ $data_{101,1} := next$ $data_{101,2} := next$ $data_{101,3} := next$ $data_{101,4} := next$ $data_{101,5} := next$

WRITEPRN(datas) := data

WRITEPRN(parameters) := param

Run: number := 10 num := number − 1 next := 1111·number

We use a solver with an implicit approach: $D(t,y) := DD(t,y,c^{\langle number \rangle})$ $J(t,y) := JJ(t,y,c^{\langle number \rangle})$

$RS := Stiffb(initial^{\langle number \rangle}, t_0, t_1, steps, D, J)$

We write data to disk:

$kk := 0,1 .. 100$ $d := floor\left(\frac{steps}{100}\right)$

$data_{kk,0} := RS_{d \cdot kk,0} \cdot 10^6$ Time in Microseconds

$data_{kk,1} := RS_{d \cdot kk,1}$ Charge in Coulombs

$data_{kk,2} := -1 \cdot RS_{d \cdot kk,2} \cdot 10$ Current in kA

$data_{kk,3} := RS_{d \cdot kk,3}$ Internal Energy in J/m

$data_{kk,4} := RS_{d \cdot kk,4} \cdot 10^3$ Channel Radius in mm

$data_{kk,5} := RS_{d \cdot kk,5}$ Plasma Density in N/m

$param_0 := c_{0,number} \cdot 10^9$ $param_1 := c_{1,number} \cdot 10^6$

$param_2 := c_{2,number} \cdot 10^2$ $param_3 := c_{3,number}$

$param_4 := c_{4,number} \cdot 10^{-3}$ $param_5 := c_{5,number}$

$param_6 := c_{6,number}$ $param_7 := c_{7,number}$

$param_8 := pp_{1,number}$ $param_9 := pp_{2,number}$

$param_{10} := pp_{3,number}$ $param_{11} := t_1 \cdot 10^6$

$param_{12} := \Delta t \cdot 10^9$ $param_{13} := c_{8,number}$

$param_{14} := 2$ $param_{15} := 3$

$param_{16} := 4$ $param_{17} := 5$

$param_{18} := 6$ $param_{19} := 7$

$param_{20} := 8$ $param_{21} := 9$

$param_{22} := 10$ $param_{23} := next$

$data_{101,0} := next$ $data_{101,1} := next$ $data_{101,2} := next$ $data_{101,3} := next$ $data_{101,4} := next$ $data_{101,5} := next$

WRITEPRN(datas) := data

WRITEPRN(parameters) := param